

Basalt Fiber Reinforced Polymer Composites

**Dr. Richard Parnas, PI
Dr. Montgomery Shaw, Co-PI
Qiang Liu, Student Assistant**

**Prepared for
The New England Transportation Consortium
August, 2007**

NETCR63

Project No. 03-7

This report, prepared in cooperation with the New England Transportation Consortium, does not constitute a standard, specification, or regulation. The contents of this report reflect the views of the authors who are responsible for the facts and the accuracy of the data presented herein. The contents do not necessarily reflect the views of the New England Transportation Consortium or the Federal Highway Administration.

ACKNOWLEDGEMENTS

The following are the members of the Technical Committee that developed the scope of work for the project and provided technical oversight throughout the course of the research:

Anne-Marie H. McDonnell, Connecticut Department of Transportation, Chairperson
William Ahearn, Vermont Department of Transportation
Tadeusz Alberski, New York State Department of Transportation
Clement Fung, Massachusetts Highway Department
Brian Marquis, Maine Department of Transportation
David L. Scott, New Hampshire Department of Transportation

**Technical Report Documentation
Page**

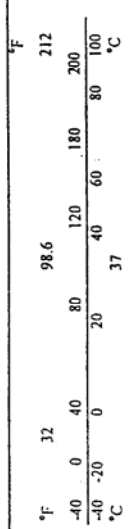
1. Report No. NETCR63		2. Government Accession No. N/A		3. Recipient's Catalog No. N/A	
4. Title and Subtitle Basalt Fiber Reinforced Polymer Composites				5. Report Date August 2007	
				6. Performing Organization Code N/A	
7. Author(s) Richard Parnas, Montgomery Shaw and Qiang Liu				8. Performing Organization Report No. NETCR63	
9. Performing Organization Name and Address <i>Institute of Materials Science, University of Connecticut</i>				10 Work Unit No. (TRAIS) N/A	
				11. Contract or Grant No. N/A	
				13. Type of Report and Period Covered FINAL REPORT	
12. Sponsoring Agency Name and Address New England Transportation Consortium C/O Advanced Technology & Manufacturing Center University of Massachusetts Dartmouth 151 Martine Street Fall River, MA 02723				14. Sponsoring Agency Code NETC 03-7 A Study Conducted in Cooperation with the US DOT	
				15 Supplementary Notes N/A	
16. Abstract <p>The objective of the research was to determine if basalt fiber reinforced polymer composites are feasible, practical, and a beneficial material alternative for transportation applications. No significant differences in stiffness and strength were found between basalt fabric reinforced polymer composites and glass composites reinforced by a fabric of similar weave pattern. Aging results indicate that the interfacial region in basalt composites may be more vulnerable to environmental damage than in glass composites. However, the basalt/epoxy interface may also be more durable than the glass/epoxy interface in tension-tension fatigue because the fatigue life of basalt composites is longer. A wide disagreement between the literature properties of basalt fibers and the properties measured in this study renders any further consideration of basalt reinforced composites highly problematical.</p> <p>Composites manufacturing issues with basalt fabric were also investigated. The measurement results of the in-plane permeability for basalt twill 3×1 fabric material showed that a high correlation exists between the two principal permeability values for this fabric. This is in contrast to the lack of correlation found in other weave patterns, and may point to an important material selection criteria for mass production of composites by liquid molding.</p>					
17. Key Words Basalt, aging, fatigue, environmental exposure, permeability, composites			18. Distribution Statement No restrictions. This document is available to the public through the National Technical Information Service, Springfield, Virginia 22161.		
19. Security Classif. (of this report) Unclassified		20. Security Classif. (of this page) Unclassified		21. No. of Pages 143	22. Price N/A

SI* (MODERN METRIC) CONVERSION FACTORS

APPROXIMATE CONVERSIONS TO SI UNITS

APPROXIMATE CONVERSIONS TO SI UNITS

Symbol	When You Know	Multiply By	To Find	Symbol	When You Know	Multiply By	To Find	Symbol
LENGTH								
in	inches	25.4	millimetres	mm	millimetres	0.039	inches	in
ft	feet	0.305	metres	m	metres	3.28	feet	ft
yd	yards	0.914	metres	m	metres	1.09	yards	yd
mi	miles	1.61	kilometres	km	kilometres	0.621	miles	mi
AREA								
in ²	square inches	645.2	millimetres squared	mm ²	millimetres squared	0.0016	square inches	in ²
ft ²	square feet	0.093	metres squared	m ²	metres squared	10.764	square feet	ft ²
yd ²	square yards	0.836	metres squared	m ²	hectares	2.47	acres	ac
ac	acres	0.405	hectares	ha	kilometres squared	0.386	square miles	mi ²
mi ²	square miles	2.59	kilometres squared	km ²				
VOLUME								
fl oz	fluid ounces	29.57	millilitres	mL	millilitres	0.034	fluid ounces	fl oz
gal	gallons	3.785	Litres	L	litres	0.264	gallons	gal
ft ³	cubic feet	0.028	metres cubed	m ³	metres cubed	35.315	cubic feet	ft ³
yd ³	cubic yards	0.765	metres cubed	m ³				
NOTE: Volumes greater than 1000 L shall be shown in m³								
MASS								
oz	ounces	28.35	grams	g	grams	0.035	ounces	oz
lb	pounds	0.454	kilograms	kg	kilograms	2.205	pounds	lb
T	short tons (2000 lb)	0.907	megagrams	Mg	megagrams	1.102	short tons (2000 lb)	T
TEMPERATURE (exact)								
°F	Fahrenheit temperature	5(F-32)/9	Celcius temperature	°C	Celcius temperature	1.8C+32	Fahrenheit temperature	°F



* SI is the symbol for the International System of Measurement

TABLE OF CONTENTS

Title Page.....	i
Acknowledgements Page.....	ii
Technical Report Documentation Page.....	iii
Metric Conversion Factors.....	iv
Table of Contents.....	v
List of Tables.....	vi
List of Figures.....	viii
Chapter 1. Introduction	1
Part I. Research Objectives and Methodology	1
Part II. Overview of Work on Basalt Fibers	3
Chapter 2. Investigation of Mechanical Properties and Durability of Basalt Fiber Reinforced Polymer Composites	6
Part I. Composite Material Preparation	8
I. Materials Used and Composite Preparations	8
II. Density and Void Content Measurement According to ASTM 1505-96	13
III. Preparation of Mechanical Property Test Specimens and Aging Conditions	16
Part II. Basalt Fiber Composite Mechanical Properties	18
I. Tensile tests, ASTM 3039.....	18
II. Flexure Test Results according to ASTM 790-71	22
III. Short Beam Strength Tests, according to ASTM D 2344	23
IV. Compression test results according to ASTM D 3410-75	25
V. Single Fiber Tensile Tests	26
Part III. Investigation of Durability of Basalt Fiber Reinforced Composites	29

I. Environmental Aging Properties	30
1. Tensile Tests According to ASTM D3039-76	30
2. Short Beam Strength Tests, According to ASTM D 2344	34
3. Discussion	42
II. Fatigue Results	44
Chapter 3. Permeability Measurement of Basalt Fabric	49
Part I. Hardware Design	49
Part II. Algebra of the Data Derivation	56
I. Derivation of Sensor Trigger Time	56
II. Permeability Calculation Procedure	59
Part III. Experimental Results and Analysis	61
I. Permeability Measurement Results	61
II. Characterization of Micro Flow Behavior	68
Part IV. Comparison of Permeability Measurement Results between UD Wetting Measurements and Radial Measurements	72
Chapter IV. Recommendation & Suggestions for Future Work	78
Part I. Summary.....	78
Part II. Future Work on Basalt for the Civil Engineering Community.....	79
Appendix. Composite Material Overview.....	81
References	122

List of Tables

Table 1.1 Comparison of Chemical Components between Different Fibers	4
Table 1.2 Advertised Comparison of Properties between Different Fibers.....	5

Table 2.1 Comparison between Three Different Fabrics	8
Table 2.2 List of Abbreviations and Their Corresponding Materials	13
Table 2.3 List of Density Values	14
Table 2.4 Density, Fiber Volume Fraction and Void Volume Content Measurements	15
Table 2.5 The Environmental Conditions Used in the Aging Tests	17
Table 2.6 Comparison of Young’s Modulus	19
Table 2.7 Statistical Analysis of the Tensile Strength Data	21
Table 2.8 Statistical Analysis of the Short Beam Shear Strength Data	24
Table 2.9 Single Fiber Tensile Test Results and Weibull Parameters for the Tensile Strength.....	28
Table 2.10 Statistical Analysis Results for the Tensile Properties Under Aging Conditions.....	32
Table 2.11 Statistical Analysis Results for the Short Beam Strength Under Aging Conditions.....	37
Table 2.12 Statistical Analysis Results for the Short Beam Strength of BE Under Aging in 40 °C Salt Water	41
Table 2.13 Raw Data in Fatigue Tests for the Composites	46
Table 2.14 Fatigue Test Results for the Composites, Parameter Fit	47
Table 3.1 Information of Basalt Fabric Used & Some Other Fabrics	62
Table 3.2 In-Plane Permeability Results for Basalt Fabric	62
Table 3.3 Experimental Results from Both Plates	64
Table 3.4 Contact Angles between Fiber and DCS	70
Table 3.5 UD Permeability Measurement Results	75
Table 3.6 Comparison of Permeability Results from UD and Radial Tests	76
Table A.1 Current Large Scale Applications of Polymer Composites.....	82

List of Figures

Figure 2.1 (a) Basalt Fabric, (b) BGF 443, (c) BGF 1527	9
Figure 2.2 Hand Lay-Up Procedures	12
Figure 2.3 RTM Mold	12
Figure 2.4 SEM Images for Basalt Epoxy and Basalt Vinylester Composites	16
Figure 2.5 Comparison of Tensile Properties	18
Figure 2.6 Flexure Test (3-point bending)	22
Figure 2.7 Comparison of the Results from Flexure Test	23
Figure 2.8 Short Beam Strength Tests	24
Figure 2.9 Comparison of Short Beam Strength between Different Composites	24
Figure 2.10 (a). Comparison of Compression Strength, (b). Failed Specimens in Compression, Basalt Epoxy (left) and Glass Epoxy (GE 1527-350)	26
Figure 2.11 Single Fiber Tensile Tests.....	27
Figure 2.12 Stress-Strain Behavior of a Single Fiber	28
Figure 2.13 Tensile Property Changes in Saturated Sodium Chloride Solution (a) & (b)	33
Figure 2.13 Tensile Property Changes in Saturated Sodium Chloride Solution (c) & (d)	34
Figure 2.14 Aging Data for Short Beam Strength in Warp Direction (a) & (b)	38
Figure 2.14 Aging Data for Short Beam Strength in Warp Direction (c) & (d)	39
Figure 2.14 Aging Data for Short Beam Strength in Warp Direction (e) & (f)	40
Figure 2.15 Aging Data in 40 °C Salt Water for Short Beam Strength of BE in Warp Direction	42
Figure 2.16 Fatigue Tests	44
Figure 2.17 Comparison of Fatigue Life when Maximum Stress is 65% of Tensile Strength	48

Figure 2.18 Comparison of Fatigue Life when Maximum Stress is 50% of Tensile Strength	48
Figure 3.1 Top Sensor Plate	50
Figure 3.2 Electrical Diagram	51
Figure 3.3 Recessed Sensor	51
Figure 3.4 Prototype Design	53
Figure 3.5 View of the Front Panel	53
Figure 3.6 Scheme of Calibrating the Pressure Transducer	54
Figure 3.7 Calibration Results of the Pressure Transducer	54
Figure 3.8 The Whole Equipment	55
Figure 3.9 Measurement Result of the DCS Viscosity	56
Figure 3.10 Fluid Flow Front	56
Figure 3.11 Distribution of Permeability	63
Figure 3.12 Correlations between Permeability in Warp and Weft Direction for Different Fabrics	67
Figure 3.13 Measurement of Surface Tension	69
Figure 3.14 The Diagram of the UD Experimental Set Up	73
Figure 3.15 Scheme of Getting the Extrapolated Permeability	74
Figure 3.16 Data from UD Experiments	76
Figure 3.17 Comparison of K_{xx} Distribution between UD and Radial Flow Tests	77
Figure A.1 Classification of Composite Materials	83
Figure A.2 Commonly Used 2D Weave Patterns	84
Figure A.3 Crack Growth Modes in Tension Stress	93
Figure A.4 Resin Transfer Molding Scheme	107
Figure A.5 Diagram of UD Permeability Measurement	110

Figure A.6 Air-Entrapment Mechanism I	115
Figure A.7 Air-Entrapment Mechanism II	115
Figure A.8 Dual Scale Flow in Fibrous Reinforcement Material	116

Chapter 1. Introduction and Literature Review

Part I. Research Objectives and Methodology

The use of basalt fibers was investigated in low cost composites for civil infrastructure applications requiring excellent mechanical properties and long lifetimes. Basalt fibers were thought to have great potential as reinforcement in both polymer materials and in concrete. However, this research focused on the use of basalt fiber reinforced polymer composites.

A range of basic mechanical tests evaluated polymer composites reinforced with basalt fibers. Tests were also done with glass-reinforced composites using the same polymer as the basalt specimens to permit direct comparison between the two reinforcing materials. Subsequent tests examined the effects of environmental exposure on the composite material behavior. An appendix provides background on composite materials, their mechanical properties, and the methods used to produce them. Reference numbers begin in the appendix.

Woven broadgoods of glass and Basalt, as nearly as identical as possible, were obtained. Woven basalt fabric was obtained from AlBarrie Ltd (Canada), and woven glass fabric was obtained from BGF Inc. The fabrics supplied had commercial sizings on the fibers to promote adhesion with the resin systems, and these were removed to directly compare the fiber performance. Although carbon reinforced composites would also be interesting to test, the expense of carbon fiber places such composites outside the usable window in realistic large scale applications. Carbon reinforced composites have been used in a number of notable demonstration projects, and extensive literature exists on their properties that permit comparisons with the measurements reported in this report on basalt and glass materials. However, the test matrix was so large that we refrained from testing carbon in order to more fully test the basalt.

Two polymers, most appropriate for outdoor usage in transportation applications were chosen, vinyl ester and epoxy. Flat plates of basalt reinforced and glass reinforced polymers were prepared by molding, of sufficient size to provide approved test specimens for a variety of standardized tests. Although manufactured composites with either glass or basalt (very recent development) fibers are available, samples were prepared in the lab to ensure the

fairest possible comparison. In this manner, comparisons were made between materials with identical fiber volume fraction and identical processing conditions, and as nearly as possible identical fiber architectures. Moreover, for the durability testing, an accurate timeline was established since the time of origin of the material was established by preparing the samples in the lab. Destructive evaluation with standardized tests such as ASTM D 3171-99 (fiber content) and D 2734-94 (void content) verified the quality of fabricated samples.

Tension and compression stress – strain curves were measured via standardized tests such as ASTM D 3039 and D 5766, and their variants, to provide elastic moduli, yield stress, ultimate strength, strain to failure, as well as a preliminary assessment of toughness.

Flexural and shear tests were measured with standardized tests such as ASTM D 2344, D 3518, D 5379, and their variants, to provide bending stiffness and strength, as well as shear stiffness and strength.

Low cycle and high cycle fatigue tests were done via standardized tests such as ASTM D 3479 to begin the assessment of durability.

The major focus of this work is the durability of the composite to environmental exposure. The factors considered for environmental exposure were time, temperature, moisture, and salinity. Elevated temperature and temperature cycling were used to accelerate the testing. Moisture exposure was accomplished by immersing samples in liquid water of various salinities. Elevated temperature testing was carried out at temperatures well below the glass transition temperature of the polymers to avoid changing the degradation mechanisms.

An important test was conducted that was not part of the original plan. Single basalt and glass fibers were tested in tension to compare the single fiber properties of the materials used in this study to the material properties claimed by the manufacturers. These tests were carried out after the planned experiments yielded results that were much less positive for the basalt material than expected based on previous literature.

Last, an investigation of processing was carried out that provides general information about producing composites using a manufacturing method called liquid molding. Although this part of the work was not in the original objectives, it was carried out with the basalt fabric and provides important information concerning the mass production of composites for large volume applications such as civil infrastructure.

Part II. Overview of Work on Basalt Fibers

Basalt is the most common rock found in the earth crust. Russia has unlimited basalt reserves [88], and only the 30 active quarries have roughly 197 million m³. In the United States [82], Washington, Oregon and Idaho have thousands of square miles covered with basalt lava. The Columbia Basalt Plateau, located in this region, has about 100,000 square miles covered with basalt. Basalt color is from brown to dull green depending on the ferrous content. Basalt fibers are made from basalt rock by melting the rock at 1300-1700 °C and spinning it [183, 184]. Due to fiber production problems of gradual crystallization of some parts and non-homogeneous melting, continuous basalt fiber was rarely used until the technology of continuous spinning recently overcame these problems [185]. The first basalt plants were built in USSR in late 1980's in Sudogda, Ukraine and Georgia. A patent about the basalt fiber production was registered in 1991[186].

The chemical composition of basalts differs to some degree, as shown in Table 1.1. Besides the chemical compositions, the mechanical properties of basalt fibers from different sources are also different [83, 88, 187], probably due to different chemical components and processing conditions like drawing temperature. Tensile strength of basalt fiber tends to increase with increasing drawing temperatures, between 1.5 and 2.9 GPa, between 1200~1375 °C. This is due to increasing proportions of crystal nuclei of basalt at lower temperatures, proved by SEM [83]. Young's modulus of Basalt fiber Varies between 78 and 90 GPa for basalt fiber from different sources, and USSR report the highest modulus of 90 Gpa [83]. Compared to glass, most references claimed that basalt fiber has higher or comparable modulus and strength [82, 88], while a few reported much lower basalt fiber strength than claimed [187].

Besides good mechanical properties, basalt has high chemo- and thermal stability [88], good thermal, electrical and sound insulating properties [188]. The thermal insulating ability of basalt is three times that of asbestos [189, 190], and due to such good insulating property basalt is used in fire protection [188-190]. Basalt has electrical insulating properties 10 times better than glass [189, 190]. Secondly, basalt has much better chemical resistance than glass fiber, especially in strong alkalis. Basalt composite pipes can transport corrosive liquids and gases [183, 184, 188-190]. Polymer concretes based on polybutadiene matrix, with quartz sand and fly ash as filler, and basalt chipping as coarse aggregate, have very high resistance to acids and alkali, excellent toughness and adhesion to metal reinforcements, low water absorption and remarkable compressive strength (80~90 MPa) [191]. In addition, basalt can be used in a wider temperature range, -260/-200 °C to about 650/800 °C compared to E-glass, -60 to 450/460 °C [183, 188-190, 192]. And replacement of glass fiber with basalt fiber can reduce the risk of environment pollution like high-toxic metals and oxides, which are produced in glass fiber production [9]. Furthermore, basalt fiber has higher stiffness and strength than glass fiber, as claimed by some people and shown in Table 1.2 below [193, 194]. Therefore, basalt fibers are more and more widely used and studied in both polymer [9, 184, 185, 188, 192, 195] and ceramic matrix based concrete. In some cases, basalt fiber is mixed with another fiber in the matrix to form a hybrid composite [196]. Some research indicates the interface between basalt fiber and polymer matrix is poor [197], while other work indicates that it is good, and that basalt fiber even has an activation effect for polymerization [9]. More practically, one report indicates that the mechanical properties of basalt reinforced polymer differ significantly from matrix to matrix [88].

Table 1.1 Comparison of Chemical Components between Different Fibers

Chemical composition, %	Basalt [88]	E-Glass	S-Glass
Silicone Dioxide, SiO ₂	48.8~51	52-56	64-66
Aluminum Oxide, Al ₂ O ₃	14~15.6	12-16	24-26
Iron Oxide, FeO+Fe ₂ O ₃	7.3~13.3	0.05-0.4	0-0.3
Calcium Oxide, CaO	10	16-25	0-0.3
Magnesium Oxide, MgO	6.2~16	0-5	9-11
Sodium Oxide & Potassium Oxide, Na ₂ O + K ₂ O	1.9~2.2	0-2	0-0.3
Titanium Oxide, TiO ₂	0.9~1.6	0-0.8	
P ₂ O ₅			
MnO	0.1~0.16		
Cr ₂ O ₃			

Fluorides		0-1	
Boron Oxide		5-10	

Due to the properties basalt has, its typical applications include [198]: production of textile fibers, floor tiles, acid-resistant equipment for heavy industrial use, rockwool, friction materials such as brake pads and linings, high-temperature insulation, and fire protection.

Table 1.2 Advertised Comparison of Properties between Different Fibers

Properties	Unit	Basalt	E-Glass	S-Glass	Silica
Density	g/cm ³	2.7	2.57	2.48	2.15
Thermal Linear Expansion Coefficient	ppm/°C	8.0	5.4	2.9	0.05
Tensile Strength	MPa	4840	3450	4710	4750
Elastic Modulus	GPa	89	77	89	66
Elongation at break	%	3.15	4.7	5.6	1.2
Compression Strength	MPa	3792	3033		3516
Maximum application temperature	(°C)	982°	650°		1100°
Sustained operating temperature	(°C)	820°	480°		1000°
Minimum operating temperature	(°C)	-260°	-60		-170°
Thermal conductivity	(W/m K)	0.031-0.038	0.034-0.04		0.035-0.04
Melting temperature	(°C)	1450°	1120°		1550°
Vitrification conductivity	(°C)	1050°	600°		1300°-1670°
Glow loss	(%)	1.91	0.32		1.75
Filament diameter	(microns)	9-23	9-13		9-15
Absorption of humidity (65%RAH)	(%)	<0.1	<0.1		<0.1
Stability at tension (20 C°)	(%)	100	100		100
Stability at tension (200 C°)	(%)	95	92		94
Stability at tension (400 C°)	(%)	82	52		80
% weight loss after 3 hrs boiling in:					
H ₂ O	(%)	0.2	0.7		0.05
2n NaOH (Sodium Hydroxide)	(%)	5.0	6.0		5.0
2n HCl (Hydrochloric acid)	(%)	2.2	38.9		15.7

Chapter 2. Investigation of Mechanical Properties and Durability of Basalt Fiber Reinforced Polymer Composites

In Table 1.2, Chapter I, the claimed tensile strength of basalt fiber is much higher than that of E-glass, and Young's modulus is also higher, basalt fiber is able to sustain higher operating temperature, and basalt fiber is more durable in boiling distilled water. These characteristics stimulated people's interest in using basalt fiber reinforced polymer composites in civil engineering infrastructures.

Transportation infrastructure is exposed to harsh conditions, including heavy loads and severe environmental effects. As a result, significant and costly maintenance and periodic replacement of infrastructure is required. Fiber-reinforced polymer (FRP) composites continue to win widespread application in aerospace, automotive, and sports. They offer many promising characteristics for civil engineering including high performance, light weight, and reduced lifecycle costs.

Currently, FRPs (usually reinforced by glass fibers) are applied to retrofitting concrete, retrofitting steel, seismic retrofit of bridge piers, bridge decks for special applications, and internal reinforcement for concrete [206]. Some bridges have been built entirely or partially of FRP [207]. The benefits of FRP are great since FRP offers the advantages of faster construction time, higher strength, lower weight, and greater environmental durability. Problems associated with FRP applications are mainly those of maintenance and initial cost [206].

Among currently used fibers for FRP, glass fiber has susceptibility to surface damage and high sensitivity to alkaline conditions [1, 208]. The chemically inert and stiffer carbon fiber has a disadvantage of high cost and anisotropy [8]. Synthetic fibers, mainly polymeric fibers, usually have low elastic modulus, low melting point and poor interfacial bonding with inorganic matrices [209].

According to reference, basalt fiber extruded from melted basalt rock possesses at least 16% higher modulus, equivalent tensile strength and better alkaline resistance [210] relative to E-glass fiber [194], excellent interfacial shear strength [210] and is currently available commercially [83]. Basalt-reinforced polymers were thought to have great potential as transportation and construction materials, and have gained some application in concrete structural members [209, 211]. Basalt fiber composite rebars [209], which typically consist of 80% fiber and 20% resin binder, may potentially replace steel wherever corrosion problems exist, such as exposure to salt water, alkaline attack, and ocean climate. In addition, basalt rebars have a density only one-third that of steel, a claimed tensile strength three times that of steel and thermal expansion coefficient very close to that of concrete. In applications and studies [209, 211], researchers have found that basalt fibers strongly affect the toughness of concrete in that basalt fiber changed the sudden and brittle failure of plain concrete to ductile failure because the gradual pullout behavior of the fiber increased energy absorption. However, before widespread application of basalt composites, the potential problems associated with durability have to be identified more quantitatively.

This chapter mainly discusses mechanical properties and environmental durability of basalt fiber reinforced polymer composites. Polymer composites reinforced by basalt fabric and glass fabrics were produced for these tests. Void content below 3% were measured for all the composites produced for the testing program. No significant differences in Young's modulus, tensile strength, flexure strength, shear strength and compression strength were found between Basalt composites and glass composites. Also reported in this paper is a study of the tolerance of the basalt fiber reinforced polymer composites to salt water immersion, moisture absorption, temperature and moisture cycling. Identical and parallel tests were conducted for the corresponding glass reinforced polymer composites. Aging in salt water or water decreased the Young's modulus and tensile strength of basalt composites a little ($p < 0.05$) after 240 days' aging. Freeze-thaw cycling up to 199 cycles did not change the shear strength significantly, but aging in 40 °C salt water and water did decrease the shear strength of basalt composites ($p < 0.05$). The aging results indicate that the interfacial region in basalt composites may be more vulnerable to damage (e.g. hydrolysis) than that in glass composites.

Part I. Composite Material Preparation

I. Materials Used and Composite Preparations

Basalt fabric was the same as used in the permeability tests: basalt twill 3/1 fabric from Albarrie Company in Canada. Two glass fabrics were chosen for comparison to the basalt fabric. The first glass fabric chosen, BGF 443, was a 1×3 RH woven twill produced by BGF Company in United States [193]. The basalt and BGF 443 glass fabrics had the same weave pattern and yarn balance between warp and weft. However, the thickness and twist of the basalt and glass yarns were different, leading to significant differences in micro-structural details such as yarn waviness. Another glass fabric, BGF 1527, was also chosen, which has the same filament diameter and yarn thickness as basalt fabric. The BGF 1527 is a plain-woven fabric, providing information on the effects of reinforcement weave pattern on composite properties. Table 2.1 summarizes the three kinds of fabric, and Figure 2.1 shows the images of them.

Table 2.1 Comparison between Three Different Fabrics [193, 200]

Properties	Basalt Fabric	E-Glass BGF 443	E-Glass BGF 1527
Areal Density, g/m ²	750	425.5	431.62
Filament Diameter, Micron	9	6	9
Yarn Linear Density, warp/weft, tex (g/km)	330	134.07	297.63
Weave pattern	Twill 3/1*	Twill 1×3 RH*	Plain weave
Yarn Balance (warp/weft), count/dm	1.53 = (119/78)	1.47 = (173/118)	1 = (67/67)

Both 3/1 and 1*3 RH means that the warp and weft yarns are interlaced with over 3 under 1, or over 1 under 3 weave pattern

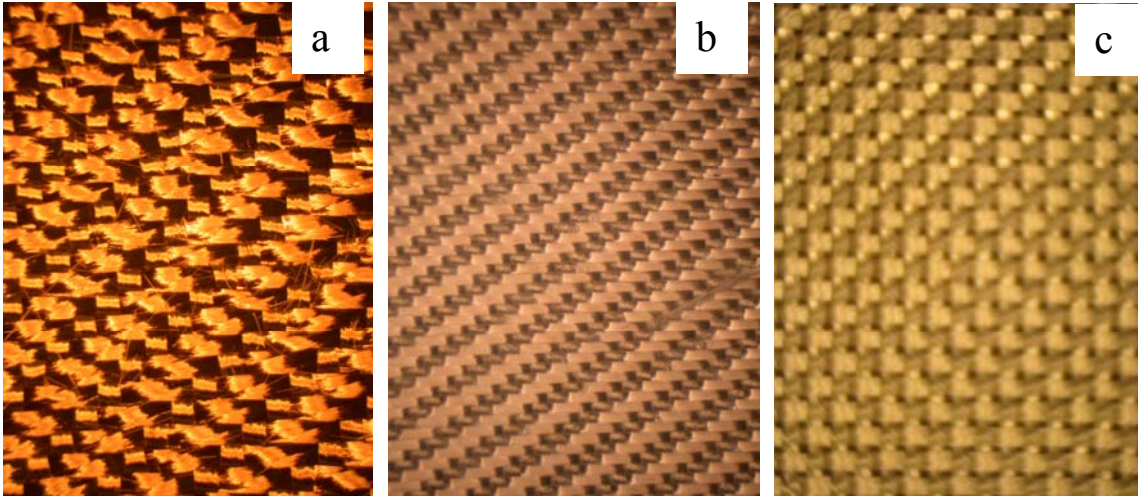


Figure 2.1 (a) Basalt Fabric, (b) BGF 443, (c) BGF 1527

Different fabrics came with different finishes on the fiber surface. Due to differences in basalt and glass fiber surface chemistry, obtaining the same interfacial interaction with the epoxy matrix is not certain, even if the same silane coupling agent is used. The structure and thickness of silane layers is sensitive to the underlying surface chemistry, therefore, the differences in basalt and glass surface chemistry are expected to cause differences in silane layer structure. Removal of fiber surface coatings was therefore planned to provide the most direct comparison of basalt and glass reinforcement. The basalt fabric came with a finish compatible with epoxy resin, and the finish was removed by heating in vacuum at 280~300 °C overnight. The BGF 443 glass fabric was heat treated at 500 °C overnight or 450 °C for 36 h to remove the acid resistant finish, consisting of acid resistant polymers/PTFE/silicone oils and graphite. BGF 1527 was treated at 500 °C or 350 °C overnight to remove the silane finish compatible with vinyl ester. The high temperature required for BGF 443 required careful attention to data interpretation.

Flat plates of basalt reinforced and glass reinforced composites were prepared by hand lay-up or RTM and curing in a mold using a Carver 4817 press. The hand lay-up mold cavity was approximately 140 mm wide, 216 mm long and 2.2 mm deep. The RTM mold cavity is approximately 400 mm × 375 mm × 2.2 mm. Although manufactured composites with both glass and basalt (very recent development) fibers are available, it was necessary to prepare samples in the laboratory to insure the fairest possible comparison. In this manner,

comparisons are made between materials with identical fiber volume fraction and identical processing conditions, and as nearly as possible identical fiber architectures.

Shell Epon 828 cured with Huntsman Jeffamine D230, at the prescribed weight ratio of 100:35, was used for the matrix in all experiments reported below. This epoxy resin system was selected because it is very common, low cost, and has a relatively high heat distortion temperature of 74 °C [212]. The resin system was mixed for 15 min by hand and then degassed under about 98 KPa vacuum for 25-30 min. In hand lay-up, the resin was injected into the mold by a syringe. The whole mold was put under 98 KPa vacuum for another 25-30 min to help the impregnation of the fabric by resin. Then the resin was cured for 1 h at 100 °C and another hour of postcure, at 140 °C, under approximately 1500 kPa pressure. The whole procedure is shown in Figure 2.2. Figure 2.3 shows the RTM mold. The bottom mold has an injection hole in the middle and an open channel across the injection hole helped to do a line injection. The top mold had four air outlets on the four corners and they were also used as vacuum lines. In RTM, the fabric materials were heat cleaned and laid them into the mold. The resin was mixed and vacuum degassed under approximately 98 KPa for 30 minutes. Before injecting the resin into the mold, approximately 98 KPa of vacuum pressure was applied from the four corners of the top mold. Then the resin mixture was injected into the mold with a flow rate about 60 ml/min. About 2 minutes later, when the mold cavity was almost full of resin, the vacuum was shut down and the vacuum lines closed, while injection was continued until the pump reached its own limit. During the injection, the mold is already heated to 100 °C. After injection, the mold was kept at 100 °C for 1 hour the materials to cure and 140 °C for another hour for post cure. The hand lay-up molded parts were mainly used in this study, so the hand lay-up molded parts are referenced by default, except for special notification.

In accordance with the data shown in Table 2.1, three layers of basalt fabric or five layers of BGF 443 glass fabric were used for each part. This lay-up resulted in approximately the same overall fiber volume fraction of 37.7%, with 15% fiber volume fraction in the weft direction and 22.7% in the warp direction for both basalt and glass composites. Four layers of BGF 1527 glass fabric were used for each part to keep the fiber volume fraction in weft direction the same, which is the direction for the tension test. Both the overall fiber volume fraction

and the weft direction fiber volume fraction of BGF 1527 composites could not be set equal to those of basalt and BGF 443 composites simultaneously because the BGF 1527 had a different warp/weft ratio. The produced pieces were cut into different test specimens with a DoAll water-cooled diamond saw. The cut edges of the specimens were polished using 600-grit sand paper to minimize any stress concentrations during the measurements.



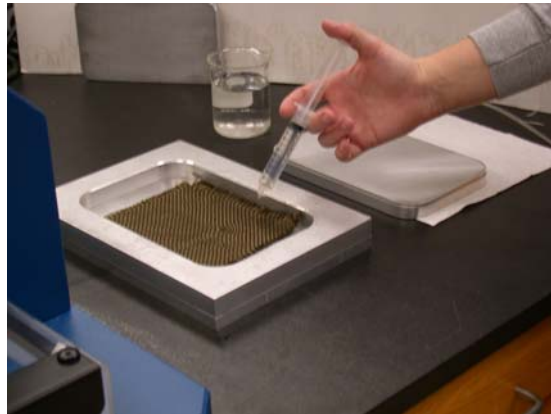
(a). Heat Clean the Fabric in the Oven



(b). Stir the Resin Mixture



(c). Vacuum the Resin in the Vacuum Oven



(d). Inject the Resin to the Mold



(e). Mold Curing in the Heat Press



(f) Finished Part

Figure 2.2 Hand Lay-Up Procedures



(a) Bottom Mold



(b) Top Mold

Figure 2.3 RTM Mold

For convenience, abbreviations are used to represent different materials in this paper. The list of the abbreviations and their corresponding materials are listed in Table 2.2.

Table 2.2 List of Abbreviations and Their Corresponding Materials

Abbreviations	Materials
BE	Epoxy reinforced by basalt fabric which was heat treated at 300 °C before application
BV	Vinyl ester reinforced by basalt fabric which was heat treated at 300 °C before application
GE 443-500	Epoxy reinforced by glass fabric (BGF 443) which was heat treated at 500 °C before application
GE 443-450	Epoxy reinforced by glass fabric (BGF 443) which was heat treated at 450 °C before application
GV	Vinyl ester reinforced by glass fabric (BGF 443) which was heat treated at 500 °C before application
GE 1527-500	Epoxy reinforced by glass fabric (BGF 1527) which was heat treated at 500 °C before application
GE 1527-350	Epoxy reinforced by glass fabric (BGF 1527) which was heat treated at 350 °C before application

II. Density and Void Content Measurement According to ASTM 1505-96

To determine the quality of the basalt composites and glass composites (with glass fabric 443), fiber volume fraction and void content were determined through the density measurements of polymer matrix and composites. The density of fiber is listed in Table 1.2 in Chapter I. Different references reported different fiber densities [88, 90, 193, 198, 200, 213, 214], and the data reported by Albarrie and BGF companies are used here [193, 200]. Measured data in this study give an estimate of the standard deviation for the fiber density to be 0.50 g/cm³. Composite materials were cut to a rectangular shape about 180 mm × 120 mm, and the density was determined by dividing the mass by its volume. Such measurement was replicated for 10 times. Polymer densities were measured using a density-gradient column containing a fluid mixture with density variation from 1.0 to 1.5 g/cm³ over a

distance of 1 meter. About 20 tiny polymer pieces were acquired from different polymer parts made under the same conditions. The 20 tiny polymer pieces were dropped into the density-gradient column, and their densities were determined according to their heights in the column. Their densities exhibited a normal distribution and the mean and standard deviation were calculated. These data are listed in Table 2.3 below, in which each cell contains (average \pm standard deviation).

Table 2.3 List of Density Values

Materials	Density, g/cm ³
Epoxy	1.164 \pm 0.001
Vinyl ester	1.130 \pm 0.031
BE	1.736 \pm 0.029
BV	1.759 \pm 0.028
GE 443	1.650 \pm 0.017
GV	1.640 \pm 0.013

The burn-off experiments were done for the composites to determine the mass content of resin and fiber. About 10 pieces of composite samples taken from different molded parts put into a glass vial, which was then weighted and heated to 500 °C for overnight. The next morning the vials were weighed again when they only contained fibers. This way, the weight content of polymer and fiber in the composites was determined.

The fiber volume fraction is,
$$v_f = \frac{m_f / \rho_f}{m_c / \rho_c} \quad (2-1)$$

where m_f and m_c represents the fiber mass and the composite mass, respectively, and ρ_f and ρ_c are the corresponding densities.

The void content is defined as,
$$v_c = 1 - v_f - \frac{\rho_c}{\rho_r} \left[1 - \frac{m_f}{m_c} \right] \quad (2-2)$$

where ρ_r is the density of resin.

The result is shown in Table 2.4 below. Burn-off tests may be as accurate as 1% for void content, if the resin and composite densities are precisely known. The accuracy of the data contained here is estimated at roughly 2%, mainly due to uncertainty in the density of the fiber and composite, assuming the composite and fiber mass measurements are accurate to 0.001%. These results indicate that all the composites had low void contents except BV.

Void content measurement results correspond well with SEM images. Those of basalt epoxy and basalt vinyl ester are shown in Figure 2.4 below. From low magnification SEM images, no significant differences between basalt epoxy, glass vinyl ester and glass epoxy were observed, and their images show that the resin impregnation of the both basalt fiber and glass fiber was good in that no voids were visually observed. The white areas in the interfacial zones of basalt vinyl ester are different than the more uniform appearance in the other composites, as exemplified by the basalt epoxy image. This difference in appearance may indicate that impregnation of vinyl ester in basalt fibers is less complete than in the other composites, and there is reduced compatibility between vinyl ester resin and basalt fiber, compared to epoxy resin.

Table 2.4 Density, Fiber Volume Fraction and Void Volume Content Measurements

	Density, g/cm ³	Fiber Volume Fraction, %	Void content, % Average ± estimated standard deviation
BE	1.736 ± 0.029	36.54	-0.28 ± 2.00
BV	1.759 ± 0.028	39.53	2.76 ± 2.00
GE 443	1.650 ± 0.017	34.01	0.16 ± 2.00
GV	1.640 ± 0.013	34.60	-0.63 ± 2.00

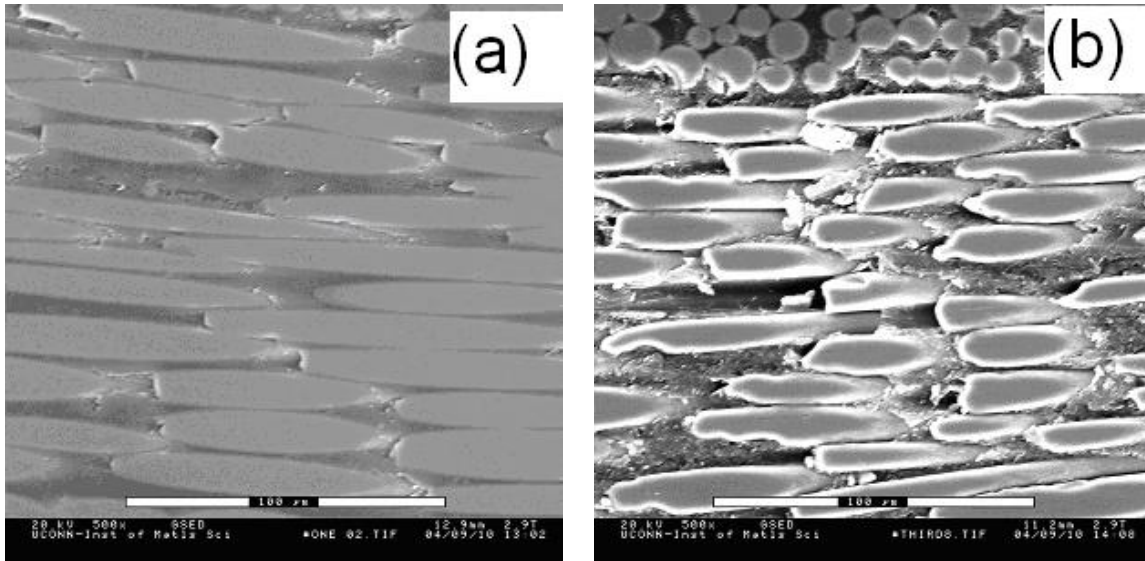


Figure 2.4 SEM Images for Basalt Epoxy and Basalt Vinylester Composites, the Length of the White Bar Represents 100 Micron. (a). BE (b). BV

III. Preparation of Mechanical Property Test Specimens and Aging Conditions

An Instron 5869 was used according to ASTM D3039-76 for the tensile tests. The rectangular tension specimens were approximately 125 mm long, 12.7 mm wide and 2.2 mm thick. They were cut along the weft direction. An Instron 1011 was used according to ASTM D 2344 to measure the short-beam strength (3-point bending), which is a screening test for shear strength [215], and long-beam flexure test according to ASTM 790-71. The shear specimens were 12 mm by 4 mm by 2.2 mm thickness, and were cut along the weft direction. The span length was approximately 4 times the specimen thickness. The flexure test specimen has the same dimension as the tension specimen, and the span-to-thickness ratio (16:1 and 32:1) was adjusted to minimize the effect of the through thickness shear deformation on the Young's modulus. These two ratios are typically used in ASTM standard 790-71. Last, compression specimens were cut to 141 mm in length, 6.4 mm in width, and 2.2 mm in thickness, with a test section of 12.7 mm for the compression test according to ASTM D 3410-75.

In the environmental aging tests, the factors considered were time, temperature, moisture, and salinity. Specimens were immersed into different environments as shown in Table 2.5 below. Table 2.5 also lists the abbreviations used to identify the material and its aging sequence.

Table 2.5 The Environmental Conditions Used in the Aging Tests

Abbreviations of aging condition for Tension test specimens		Abbreviations of aging condition for Shear test specimens	
SRT	Saturated sodium chloride solution immersion at room temperature	FTC	Freeze-thaw cycling in saturated sodium chloride solution between -8.5 °C and 20 °C, with 4.8 hours per cycle. The number after 'FTC' represent the number of cycles in such condition
SHT	Saturated sodium chloride solution immersion at 70 °C	SH	Saturated sodium chloride solution immersion at 40 °C
WRT	Distilled water immersion at room temperature	WH	Distilled water immersion at 40 °C
CWRT	Cycling between dry 2 days and wet (distilled water immersion) 2 days at room temperature		
FT	Cycling between freeze 2 days at -10 °C and thawing 2 days at 20 °C in saturated sodium chloride solution		
Note: the number after the abbreviation represents the number of days in such condition.		Note: the number after 'WH' and 'SH' represents the number of days in such condition	

Part II. Basalt Fiber Composite Mechanical Properties

I. Tensile Tests

The comparison for Young's modulus is shown in Figure 2.5 below. To remove the finishes on glass fabric, they were heat treated. While such heat treatment is known to decrease the tensile strength of glass fiber [216], it should not influence the modulus of the fiber. Indeed, the heat-treatment temperature for glass fabric had no observable effect on Young's modulus of the glass composites. The differences in the weave patterns between the glass fabrics were not large enough to cause observable differences in modulus. Basalt-epoxy composites exhibited a similar modulus to glass-epoxy composites. The height of the bars in Figure 2.5 (a) represent the average of 5 or 6 replicated measurements (entirely different pressings), and the error bars represent the 95% confidence interval of the mean. Each of the specimens for the replicated measurements was from a different molded part, so they were independent from each other. The same statistical considerations also hold for the other figures in this paper.

As discussed above, the tensile properties in the weft direction, in which fiber volume fraction is around 15%, were tested. If the linear mixing law [217] is used to calculate the modulus and consider yarn architecture effects such as twist and waviness [4], the measured values match the expected values closely. The analysis is shown in Table 2.6 and the fiber moduli are listed in Table 1.2 in Chapter I.

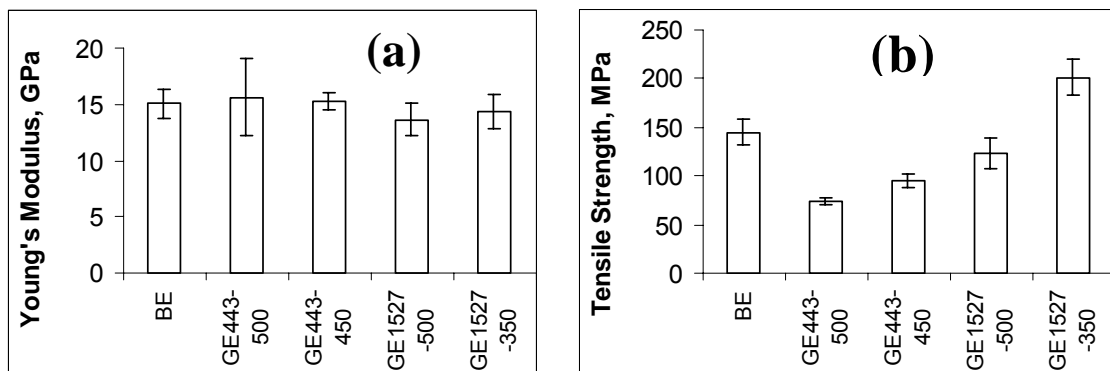


Figure 2.5 Comparison of Tensile Properties. (a) Young's Modulus, (b). Tensile Strength.

Table 2.6 Comparison of Young's Modulus

Material	Measured Young's modulus, (mean \pm 95% Confidence Interval)GPa	Calculated Young's modulus using linear mix law, GPa
BE	15.35 \pm 1.35	13.74
GE 443-450	15.26 \pm 0.83	13.46
GE 443-500	15.65 \pm 3.38	13.46
GE 1527-350	14.41 \pm 1.53	
GE 1527-500	13.66 \pm 1.40	

Note from Table 1.2 that the modulus of basalt is higher than that of glass. The similar glass and basalt composite moduli are due to several reasons. The most important is the difference in twist between the basalt fibers and the glass fibers. Glass fibers are not twisted, but basalt fibers have a twist of 100 /m, which leads to a roughly 18% stiffness loss compared to straight basalt fibers, considering the yarn thickness [3]. The modulus of both basalt and glass composites are further reduced relative to the unidirectional composites due to the yarn waviness in the fabric. A suggested knockdown factor for the modulus of fabric reinforced composites is 10% [4]. Third, the basalt fabric has a larger shear angle than the glass fabric after being cut, which also reduces the basalt composite modulus relative to the glass composite modulus. Thus, the combined effects of subtle differences in yarn architecture such as yarn twist, waviness, and shear may reduce the basalt composite modulus by 25%, negating the higher basalt fiber stiffness.

In addition, through two-sample t-test [218, 219], the BV had a lower modulus ($P = 0.002$, P -value will be explained later in this paper) than GV-443, in that (mean \pm 95% C. I.) = (10.67 \pm 1.35) GPa for BV, and (13.82 \pm 1.64) GPa for GV-443. This lower modulus may also be due to a reduced compatibility between basalt fiber and vinyl ester, indicated in Figure 2.4 SEM images.

The comparison of tensile strength between different composites is shown in Figure 2.5 (b). This comparison is more complicated, since both the weave types and fabric heat treatment temperatures appear to affect the composite tensile strength, as can be demonstrated by

statistical analysis [219]. A Generalized Linear Model (GLM) was formulated to evaluate the important effects on composite tensile strength, considering the three materials and four heat-treatment temperatures. A generalized linear model is a regression model, made up of a random component (ε), a linear function of the design factors (X_i), and the unknown regression parameters (β_j). In our case, a constant, μ , and 2 design factors, X_0 and X_1 , are required to differentiate the 3 materials, and a third design factor, X_2 , is required to describe the effects of heat treatment temperature.

$$\log S_T = \mu + \beta_0 X_0 + \beta_1 X_1 + \beta_2 X_2 + \beta_3 (X_1 X_2) + \varepsilon \quad (2-3)$$

where S_T is the tensile strength, μ is a constant (unbiased estimator of the strength of GE443 using a heat-treatment temperature of 400 °C), X_0 is the first design factor ($X_0 = 1$ for basalt and 0 otherwise), X_1 is the second design factor ($X_1 = 1$ for glass 1527 and 0 otherwise), and X_2 is the third design factor for the heat treatment temperature. The values of X_2 were coded into the model as (-2, -1, 1 and 2) corresponding to (300, 350, 450 and 500 °C). The fifth term, $X_1 X_2$, models the interaction, if any, between the weave pattern and the heat treatment temperature.

The regression results and statistical analysis in Table 2.7 were computed with commercially available software [220]. After the t statistic was calculated, the P-value associated with that t statistic was found from the t probability distribution [219]. The P-value provides the confidence level (“significance”) of the associated design factor. For example, in Table 2.7, the P-value of β_0 is 0.14. Therefore, design factor X_0 is significant only at an 86% confidence level (more precisely, there is a 14% chance of being wrong by rejecting the hypothesis that the design factor X_0 is insignificant.). As this P-value is fairly high, it would be necessary to perform additional tests to distinguish between the tensile strengths of BE and GE 443.

Table 2.7 Statistical Analysis of the Tensile Strength Data. Total Degrees of Freedom = 31.

Design Factor	Degree of freedom	Regression coefficient, β	Standard Error (s_{β_i}) for β	t statistic (β/s_{β_i})	P-value
X_0	1	-0.12745	0.08301	-1.54	0.136
X_1	1	0.14686	0.03800	3.86	0.001
X_2	1	-0.10776	0.02349	-4.59	<0.001
X_1*X_2	1	0.03617	0.02465	1.47	0.154

With similar reasoning, design factor X_1 is important with a greater than 99% confidence level because the P-value associated with β_1 is only 0.001. Thus, there is a significant difference in tensile strength between GE 443 and GE 1527 in our study, which is probably due to the different weave patterns. In fabric-reinforced composites, the axial tensile strength is usually lower than that for unidirectional composites due to the fiber crimp, which causes local stress perturbations [5]. Fabric reinforcing efficiency depends strongly on the percentage of the straight fiber length [42, 221]. Since the tensile strength is tested in the weft direction, and the density of warp yarns is larger in GE 443 than that in GE 1527, it is reasonable that GE 1527 would have higher tensile strength than GE 443. Since the warp yarn density in basalt-epoxy composites is also higher than that in GE 1527, it's highly possible that basalt-epoxy composites reinforced with the same weave pattern as GE 1527 will show even higher tensile strength.

Design factor X_2 is also important with a very high confidence level since the P-value associated with β_2 is even smaller than 0.001. Our study indicates that there is an extremely high probability that the fabric heat treatment temperature has a significant and detrimental effect on tensile strength. High temperatures used to remove finishes damaged the glass fiber and made it more brittle [216]. This statistical analysis has allowed the heat treatment effects to be deconvoluted from the effects of weave pattern and material differences. As the X_1X_2 term proved to be insignificant because of the relatively large P value of 0.154, one can tentatively assert that the heat-treatment temperature has substantially the same effect on

each weave pattern. Other interactions can also be investigated with this statistical approach, such as the interaction between material type and heat treatment (X_0X_2), but those interactions are not critical for this data analysis.

II. Flexure Test Results According to ASTM 790-71

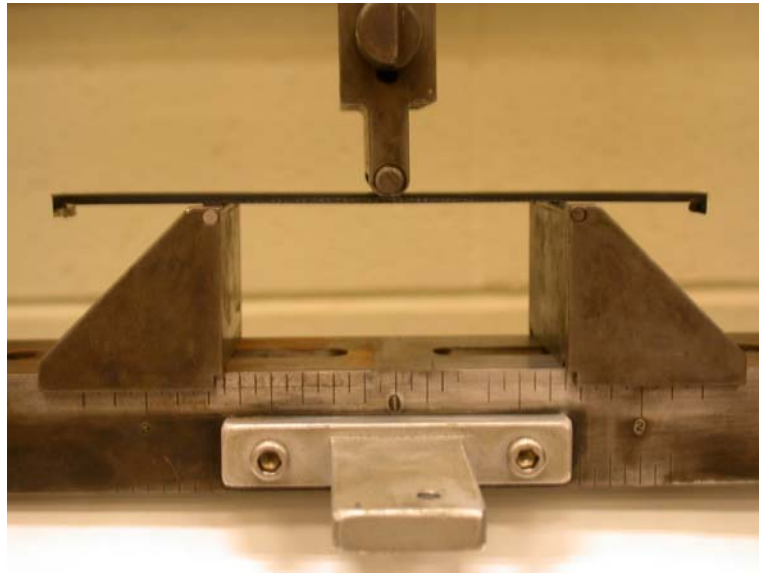


Figure 2.6 Flexure Test (3-point bending)

Figure 2.6 shows the flexure tests performed. The distance between the two supporting points is called ‘span’. In the flexure tests, the span can be adjusted to change the ratio between the span and specimen thickness, so as to minimize the effect of the through thickness shear deformation on the Young’s modulus [222].

Figure 2.7 compares the results for Young’s modulus and strength from the flexure test. The Young’s moduli from tension and flexure tests were almost the same. Through-thickness shear modulus effects may have caused some of the small differences observed by lowering the observed modulus. The strengths from the flexure test look much larger than from the tension test, although the material failed the same way, tension. This is due to the size effect, which is well documented [223]. The size effect is the decrease of mean strength with

increasing flaw-sensitive volume under stress. In the flexure test, the volume under maximum stress is only the outer surface in the central gauge length of the beam, while in the tension test the whole specimen is under maximum stress. Therefore, the strength measured in tensile tests is expected to be lower than in flexure tests because the volume under maximum stress is much larger in the tensile test. The relative flexure strengths of our various samples appeared the same as found in tension because the failure mechanism is the same in both tests, tensile fiber failure.

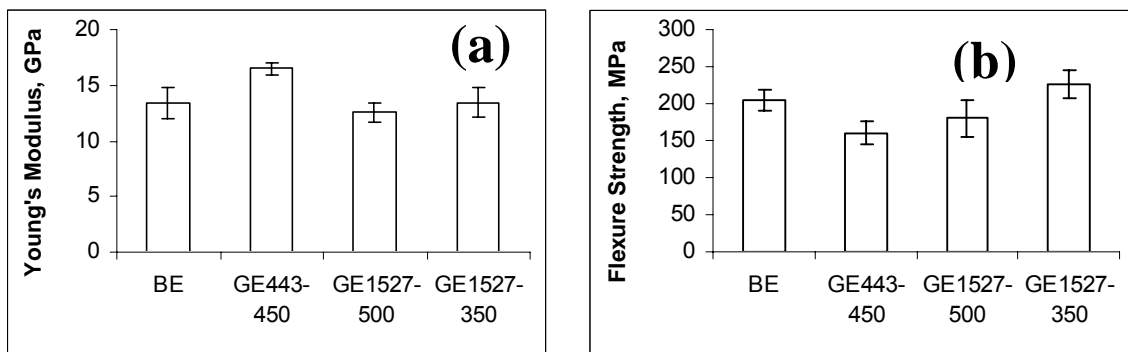


Figure 2.7 Comparison of the Results for Young's Modulus (a), and Strength (b) from Flexure Test

III. Short Beam Strength Tests, According to ASTM D 2344

The short beam strength test is shown in Figure 2.8 and it is still a 3-point bending configuration, but the span is much shorter than that in the flexure tests. The short beam strength in the weft direction of basalt epoxy appears to be much larger than that of glass epoxy (GE 443-450), as shown in Figure 2.9. However, the short beam strength of GE 1527-350 is much larger than that of GE1527-500, due to the heat treatment temperature effect. To deconvolute the material, weave pattern, and thermal effects, the GLM analysis was used again, with the same design variables.

$$\log S_S = \mu + \beta_0 X_0 + \beta_1 X_1 + \beta_2 X_2 + \varepsilon \quad (2-4)$$

In Equation (2-4), S_S is the short beam shear strength. The interaction term explored in the GLM for tensile strength, Equation (2-4), is not included here because data at different heat treatment temperatures is not available for the GE 443 material.

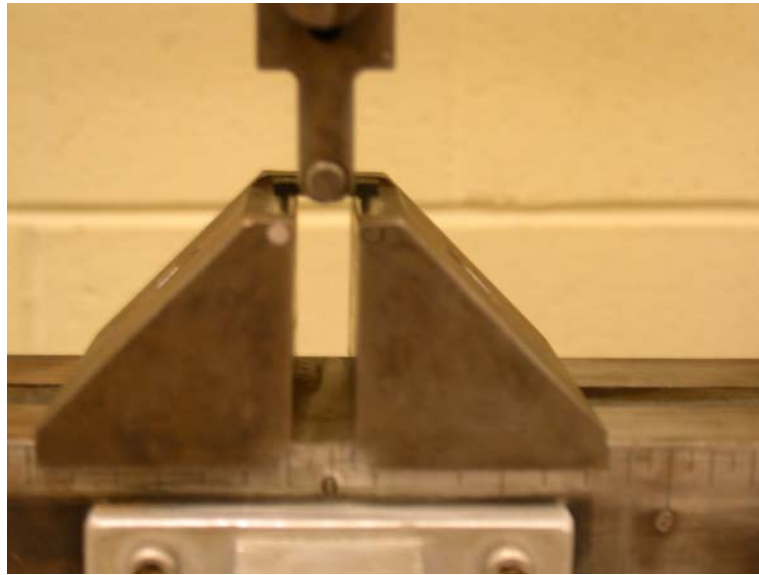


Figure 2.8 Short Beam Strength Tests

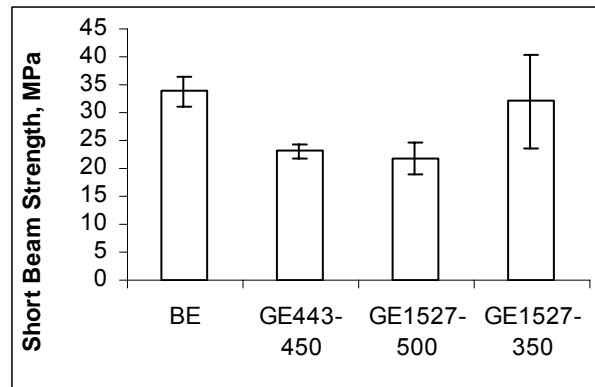


Figure 2.9 Comparison of Short Beam Strength between Different Composites

Table 2.8 Statistical Analysis of the Short Beam Shear Strength Data. Total d. f. = 22.

Design Factor	Degree of freedom, d.f.	Regression coefficient, β	Standard Error (s_{β}) for β	t statistic (β/s_{β})	P-value
X_0	1	0.00938	0.05571	0.17	0.868
X_1	1	0.02642	0.03486	0.76	0.458
X_2	1	-0.05231	0.01344	-3.89	0.001

The regression results are shown in Table 2.8 above. The P value for β_0 is 0.868 which is relatively large. This demonstrates that there are no significant differences in the short beam strengths of basalt epoxy and GE 443, when the effects of heat treatment are accounted for. Similarly, the P value for β_1 is 0.458, which demonstrates that weave pattern does not significantly affect glass composite short beam strength either. It is important to note that this result is different from the case in tension where weave pattern was significant ($p = 0.001$). Last, the P value for β_2 is 0.001, which demonstrates that fabric heat treatment temperature affects short beam strength significantly at a 99.9 % confidence level.

By observing the broken pieces, it was found that in the weft direction, all specimens broke suddenly once the crack started from the center-bottom edge. The shear failure across the fiber-matrix interface induced fiber break (tension failure) and then the material failure. This failure mechanism is discussed by others [215]. Due to the role of tensile fiber failure in the overall failure process, differences in the short beam strengths of GE 1527-500 and GE 1527-350 were observed. A 500 °C heat treatment temperature damaged the glass fiber and made it more brittle in tension.

IV. Compression test results according to ASTM D 3410-75

Compression results are shown in Figure 2.10 (a). Although high temperature heat treatment reduced the composite tensile strength due to fiber damage, such damage has negligible effect on composite compression strength [5]. So, no difference in compression strength is shown between GE 1527-350 and GE 1527-500. Also, no difference appeared between glass-epoxy and basalt-epoxy composites. Figure 2.10 (b) shows a failed basalt epoxy specimen in compression and all the other specimens (including basalt epoxy and glass epoxy) failed in the same way. This is a classic fracture pattern in compression, consisting of fiber micro buckling to form a “kink band” [44, 101]. Such fiber buckling and kink band formation are caused by local shear instability between fiber and matrix [4]. The similar compressive and short beam shear strengths observed for BE and GE443 suggest that many properties of the interfacial region around the basalt and glass fibers are similar in an epoxy matrix.

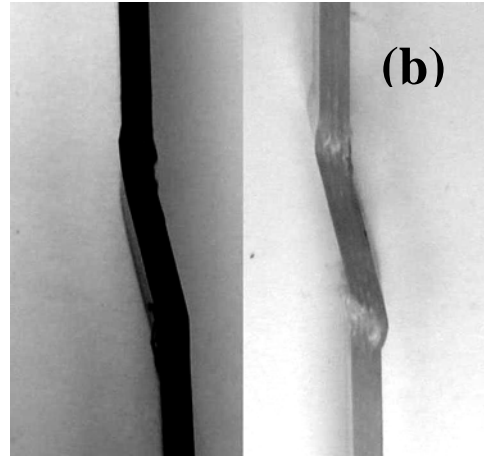
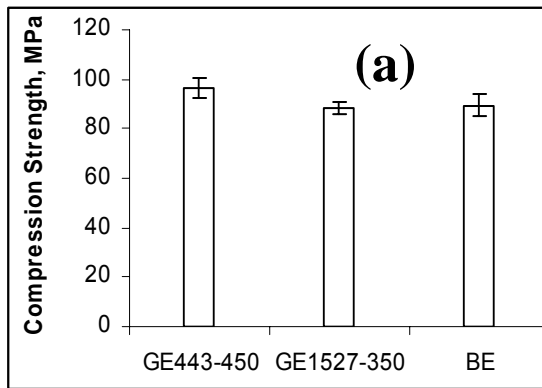


Figure 2.10 (a). Comparison of Compression Strength, (b). Failed Specimens in Compression, Basalt Epoxy (left) and Glass Epoxy (GE 1527-350).

V. Single Fiber Tensile Tests

No significant differences in tensile, shear and compressive strengths were found between basalt epoxy and the corresponding glass epoxy (GE 443). Basalt and glass composites also showed a similar Young's modulus, although some previous work indicates that a larger modulus is expected from basalt-reinforced composites [194]. Some possible reasons for the lower than expected BE modulus include yarn twist in the basalt yarn (absent in the glass), larger basalt yarn waviness and larger basalt fabric shear. The weave pattern and heat treatment temperatures have a significant effect on tensile strength for glass composites.

The comparison of the glass reinforced and basalt reinforced composites led to questions concerning the validity of the mechanical properties of basalt fiber, as claimed in Table 1.2 in chapter I. Therefore, single fiber tensile tests were performed for both basalt and glass fibers. A square hole was cut in a stiff paper board, and both ends of a single filament were glued along the hollow section on the center of the paper board, as shown in Figure 2.11 below. The length of the hollow section was the gauge length of the test.

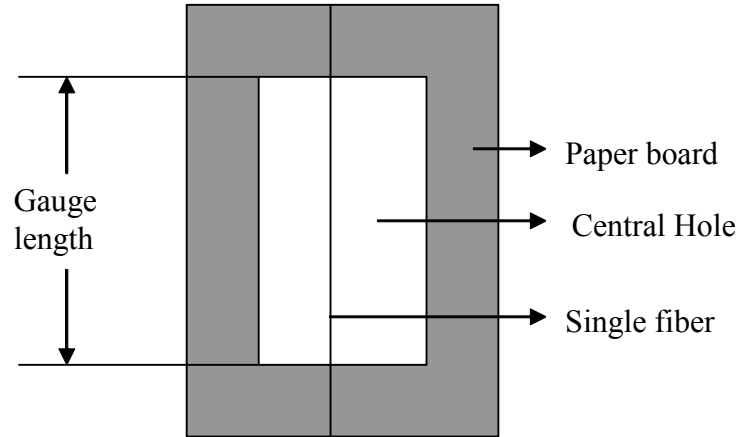


Figure 2.11 Single Fiber Tensile Tests

The diameter of the fiber was determined from optical microscope with a zoom of 40 times. Then the specimen was fixed on the Instron 1011. Using a 5N load cell, a tensile load was applied on the specimen under a displacement control of $(0.1 \times \text{gauge length})/\text{min}$. The tensile load and elongation were measured until the fiber was broken, then the tensile strength, Young's modulus and strain to failure were determined. The tensile curve is shown in Figure 2.12 below. The fiber (whether basalt or glass fiber) behaved very stiff, and the stress-strain is linear until broken. The results are listed in Table 2.9, in which the cell contains (mean \pm 95% confidence interval) from about 50 independent tests. Table 2.9 also supplies the fits for Weibull distributions for the tensile strength data with the Weibull parameters estimated by Maximum Likelihood method [102]. From Table 2.9, the Young's moduli measured for both basalt and glass fibers were close to the advertised values in Table 1.2. However, the tensile strength of basalt fiber is not significantly higher than that of the glass fiber, which is different than Table 1.2, if the fiber strength is compared for the same gauge length.

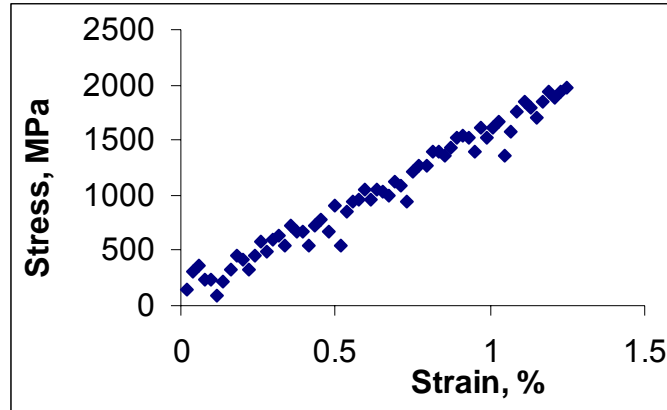


Figure 2.12 Stress-Strain Behavior of a Single Fiber

Table 2.9 Single Fiber Tensile Test Results and Weibull Parameters for the Tensile Strength

	Basalt Fiber	Basalt Fiber	Glass Fiber
Gauge Length, mm	100	25	100
Young's Modulus, GPa	87.1 ± 2.3	84.2 ± 1.7	76.2 ± 1.7
Tensile Strength, MPa	1371.49 ± 123.49	2245.3 ± 126.8	1547.7 ± 155.9
Weibull Distribution	$R(\sigma) = \exp\left[-\left(\frac{\sigma}{1500.17}\right)^{3.67}\right]$		$R(\sigma) = \exp\left[-\left(\frac{\sigma}{1654.24}\right)^{3.06}\right]$
Interpolated Length, mm	1.36 mm to achieve 4840 MPa tensile strength		10.55 mm to achieve 3450 MPa tensile strength

From Table 2.9, when the gauge length was decreased to 25 mm, much higher tensile strength was obtained for basalt fiber, due to the significant effect of gauge length on the measured tensile strength. Consider the Weibull distribution, equation (1-6),

$R(\sigma) = \exp\left[-\left(\frac{\sigma}{\sigma_0}\right)^\alpha\right]$, the location parameter σ_0 is also called the characteristic strength, and

is very close to the mean of the measured strength. If one assumes that in the tensile test of

the single fiber, the fracture origins are spatially distributed only on the fiber surface, σ_0 can be written as [222]

$$\sigma_0 = \frac{\sigma_{\theta,A}}{A^{\frac{1}{\alpha}}} \quad (2-5)$$

where A is the surface area of the fracture origin, $\sigma_{\theta,A}$ is a parameter irregardless of the surface area or stress level. Since for a single fiber, surface area is proportional to the length, one can write $A_{100} = \frac{100}{x} A_x$, where A_{100} is the surface area for fiber with gauge length of 100 mm, A_x is that for fiber with gauge length of x mm. So two equations can be constructed:

$$\sigma_{0,100} = \frac{\sigma_{\theta,A}}{A_{100}^{\frac{1}{\alpha}}} \quad (2-6)$$

and

$$\sigma_{0,x} = \frac{\sigma_{\theta,A}}{A_x^{\frac{1}{\alpha}}} \quad (2-7)$$

according to equation (2-5), assuming $\sigma_{\theta,A}$ or α doesn't change with gauge length. Let $\sigma_{0,x} = 4840$, and solve the unknown parameter x according to equation (2-6), (2-7) and $A_{100} = \frac{100}{x} A_x$, the gauge length required to have the fiber tensile strength reach the claimed value can be estimated as 1.36 mm. When the same procedure is used with the data for the basalt fiber with 25 mm gauge length, a different result is estimated, 0.61 mm. Both are so small that it's difficult and unreasonable to achieve in the real experiment. Therefore, the claimed value may have probably overestimated the tensile strength of basalt fibers. Apply the same procedure for the E-glass fiber, the estimated gauge length for its tensile strength to arrive at claimed value (3450 MPa) is 10.55 mm, which is small but still reasonable.

Part III. Investigation of Durability of Basalt Fiber Reinforced Composites

In Part II, the mechanical properties of basalt twill 3×1 fabric-reinforced polymer composites were comparable to composites reinforced with glass fabric with similar structures. Use in transportation, however, requires a better knowledge of many properties associated with

environmental durability. Reported in Part III is a study of the tolerance of the basalt-fiber-reinforced polymer composites to environmental aging conditions such as salt water immersion, moisture absorption, temperature, moisture cycling, and durability to mechanical aging, tension-tension fatigue tests. Parallel tests were conducted for the corresponding glass-reinforced polymer composites. Aging for 240 days in salt water or water decreased the Young's modulus and tensile strength of basalt composites slightly but significantly ($p < 0.05$). Freeze-thaw cycling up to 199 cycles did not change the shear strength significantly, but aging in hot (40 °C) salt water or water did decrease the shear strength of basalt composites ($p < 0.05$). The aging results indicate that the interfacial region in basalt composites may be more vulnerable to damage than that in glass composites.

I. Environmental Aging Properties

1. Tensile tests according to ASTM D3039-76

In Part II, no significant difference in Young's modulus existed between BE and GE-443. The Young's moduli were: (mean \pm 95% C. I.) = (15.05 \pm 1.35) and (15.65 \pm 3.37) GPa for the BE and the GE-443, respectively. However, BV has lower Young's modulus than GV.

The statistical analysis in Part II demonstrated that no significant difference in tensile strength exists between basalt epoxy (BE) and glass epoxy reinforced by BGF 443 glass fabric (GE-443). The seemingly higher tensile strength of basalt composites is due to the heat treatment effect, i.e. high temperature (500 °C) treatment on glass fabric BGF 443, which damaged the glass fiber and made it more brittle in tension.

In the environmental aging tests, SRT, WRT, SHT, CWRT and FT were used for BE, SRT and WRT were used for GE-443, SRT and FT were used for BV and only SRT was used for GV (see Table 2.5 in Part I). To demonstrate the property change in the environmental aging with time, a GLM model was designed. In the case of basalt epoxy (BE), a constant, β_0 , and three design factors, X_1 , X_2 and X_3 are required to differentiate the 4 aging conditions, and a fourth design factor, X_4 , is required to describe the effects of aging time. For the Young's modulus of BE, the GLM is described as:

$$G = \beta_0 + \beta_1 X_1 + \beta_2 X_2 + \beta_3 X_3 + \beta_4 X_4 + \varepsilon \quad (2-8)$$

where G represents Young's modulus with unit of GPa, design factors X_1, X_2, X_3 , represent the effect of environmental aging condition, $X_1 = 1$ for SRT, and 0 otherwise, $X_2 = 1$ for WRT and 0 otherwise, $X_3 = 1$ for FT and 0 otherwise. Therefore, the base case is CWRT where $X_1 = X_2 = X_3 = 0$. X_4 represents the time effect, and is coded to 0, 2, 3, 6, 9, 12 corresponding to 0, 40, 60, 120, 180 and 240 days' aging. ε is the Gaussian error term. The regression results and statistical analysis in Table 2.10 were computed. For the analysis of tensile strength of BE, change equation (2-8) to

$$\sigma_T = \beta_0 + \beta_1 X_1 + \beta_2 X_2 + \beta_3 X_3 + \beta_4 X_4 + \varepsilon \quad (2-9)$$

where σ_T represents the tensile strength with the unit of MPa, and all other terms are the same as in equation (2-8). For GE, property changes were investigated only in SRT and WRT, and for BV and GV only SRT and FT, the GLM is changed to $G = \beta_0 + \beta_1 X_1 + \beta_4 X_4 + \varepsilon$ and $\sigma_T = \beta_0 + \beta_1 X_1 + \beta_4 X_4 + \varepsilon$. In these equations, all terms have the same meaning as those in equation (2-8) and (2-9).

The P-value in the first row of Table 2.10, for β_1 under BE Young's modulus, is 0.056. Therefore, SRT affects the Young's modulus of BE significantly differently than the base condition which is CWRT 94.4% confidence (more precisely, there is only a 5.6% chance of being wrong by rejecting the hypothesis that different aging conditions SRT and CWRT affect the Young's modulus of BE to the same extent). However, a 95% confidence level is typically required for a strong conclusion. Therefore, at a confidence level of 95%, there is no significant difference between the effect from SRT and that from CWRT. However, since this P-value for β_1 is very close to 5%, additional experiments would permit a more certain conclusion concerning the differences between SRT and CWRT aging protocols. Clear cut cases are the P-values for β_2 and β_3 , which are both much larger than 0.05. These cases demonstrate that there appears to be no difference between the WRT, FT, and CWRT aging conditions on the BE Young's modulus. However, the P-value for β_4 , associated with aging time effects on BE Young's modulus, is less than 0.001. Thus, aging time has a significant effect on the BE Young's modulus.

Table 2.10 Statistical Analysis Results for the Tensile Properties under Aging Conditions

BE Young's modulus (total d. f. = 131)	Estimate	Standard Error (s_{β_i}) for β	t statistic (β/s_{β_i})	P-value
β_1 , SRT	-0.990	0.513	-1.93	0.056
β_2 , WRT	-0.729	0.509	-1.43	0.154
β_3 , FT	-0.307	0.509	-0.60	0.547
β_4 , time	-0.308	0.043	-7.22	<0.001
BE Tensile Strength (total d. f. = 134)				
β_1 , SRT	-5.712	4.619	-1.24	0.218
β_2 , WRT	-3.217	4.584	-0.70	0.484
β_3 , FT	-3.889	4.584	-0.85	0.398
β_4 , time	-1.242	0.381	-3.26	0.001
GE-443 Young's modulus (total d. f. = 66)				
β_1 , SRT	-0.090	0.393	-0.23	0.819
β_4 , time	-0.056	0.047	-1.18	0.241
GE-443 Tensile Strength (total d. f. = 70)				
β_1 , SRT	-0.172	2.167	-0.08	0.937
β_4 , time	-0.508	0.256	-1.98	0.051
BV Young's modulus (total d. f. = 67)				
β_1 , SRT	-0.118	0.271	-0.44	0.664
β_4 , time	-0.250	0.032	-7.86	<0.001
BV Tensile Strength (total d. f. = 65)				
β_1 , SRT	-3.440	4.295	-0.80	0.426
β_4 , time	-0.943	0.506	-1.86	0.067
GV-443 Young's modulus (total d. f. = 66)				
β_1 , SRT	0.154	0.421	0.37	0.716
β_4 , time	-0.176	0.055	-3.19	0.002
GV-443 Tensile Strength (total d. f. = 55)				
β_1 , SRT	1.487	2.136	0.70	0.489
β_4 , time	-0.465	0.280	-1.66	0.103

By similar procedures, BE tensile strength dropped significantly with aging time. In sum, all aging conditions used here degraded the BE Young's modulus to a similar extent. All aging conditions used here also degraded the BE tensile strength.

The results of the statistical analysis on the Young's modulus and tensile strength for the other three composites are also shown in Table 2.10 above. The Young's modulus of GE-443 stayed much the same in the environmental aging conditions, SRT and WRT, at a high confidence level. However, the P-value for the time effect on tensile strength of GE-443 is 0.051. This is quite close to 0.05, which is our arbitrary confidence level threshold, it is not certain whether the tensile strength of GE-443 decreased over time after 240 days' aging. Referring to Figure 2.11 (b) below, even if there was some degradation to the tensile strength of GE-443, it was very small. The results for BV and GV-443 both indicate that Young's modulus dropped in SRT and FT at a confidence level of more than 99%. For GV-443, the tensile strength probably did not decrease significantly due to the large P-value. However, the P-value for BV tensile strength changes over time is 0.067, also very close to our arbitrary confidence level (95%). Thus, there is some uncertainty about the significance of any decrease in the tensile strength of BV. Figure 2.11(d) indicates that any decrease in BV tensile strength was very small.

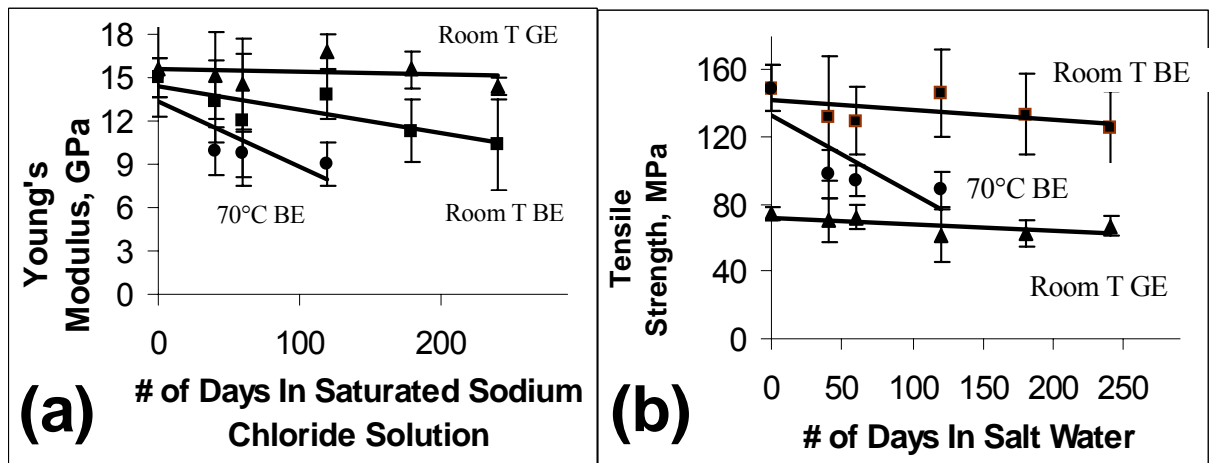


Figure 2.13 Tensile property changes in saturated sodium chloride solution. (a) Young modulus for for GE-443 at room temperature and for BE at room temperature and at 70 C, (b) Tensile strength for for GE-443 at room temperature and for BE at room temperature and at 70 C

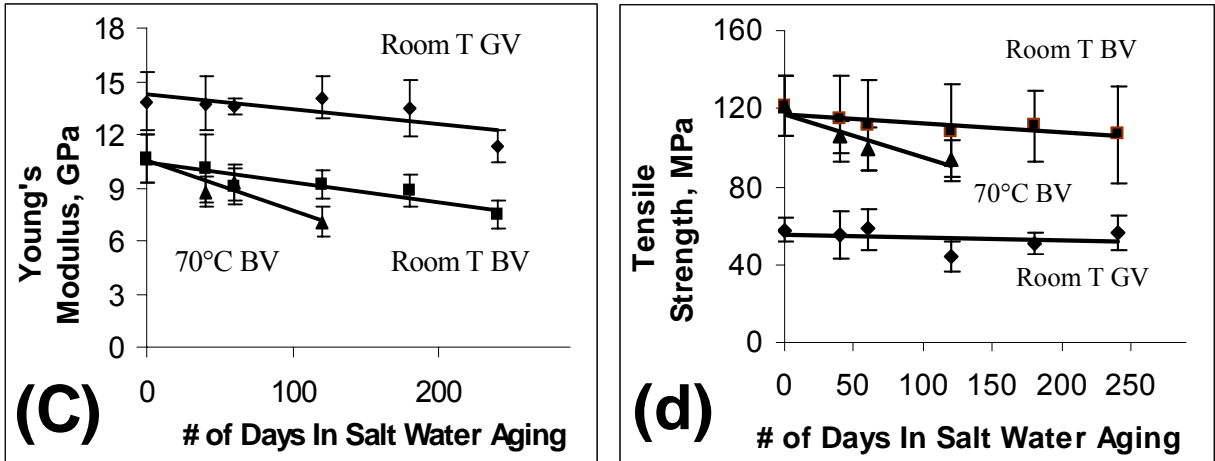


Figure 2.13 Tensile property changes in saturated sodium chloride solution. (c) Young's modulus for GV-443 at room temperature and for BV at room temperature and at 70 C, (d) Tensile strength for GV-443 at room temperature and for BV at room temperature and at 70 C.

2. Short Beam Strength Tests, according to ASTM D 2344

In Part II the Interlaminar Shear Strength (Short Beam Strength) for BE and GE-443 was discussed, and no significant difference in the short beam strength was found. The seemingly much larger shear strength of BE than GE-443 is due to the heat-treatment effect. In the tests, BE and BV specimens failed usually with large deformations, and small cracks in the middle of the thickness on the specimen surface could be observed. The failure mechanism is believed to be interfacial shear failure. On the contrary, GE-443 and GV-443 specimens failed in a brittle way, with cracks across the width in the middle of the bottom surface, and some specimens even broke cleanly into two pieces. Such failure was caused by fiber tension failure before any interface or matrix shear failure, leading to the conclusion that the high-temperature heat treatment (500 °C) damaged the fiber and made it more brittle in tension. This effect decreased the tensile strength of glass composite specimens and changed the failure mechanism in the interlaminar shear test from the expected interlaminar shear failure to fiber tensile failure.

In the aging test for the short-beam strength, FTC, SH and WH were used for BE and GE-443, FTC and SH were used for BV, SH and WH were used for GV-443 (See Table 2.5). To investigate the short beam strength change with aging in freeze-thaw, a GLM model was built as follows:

$$\sigma_s = \beta_0 + \beta_1 X_1 + \varepsilon \quad (2-10)$$

Here σ_s represents the short-beam strength with the unit of MPa. Design factor X_1 represents the number of freeze thaw cycles. ε represents the Gaussian error. To investigate the short-beam strength change in SH and WH, another GLM was designated as

$$\sigma_s = \beta_0 + \beta_1 X_1 + \beta_2 X_2 + \varepsilon \quad (2-11)$$

where σ_s represents the short beam strength with the unit of MPa. Design factor $X_1=0$ for SH and 1 for WH. Design factor X_2 represents the aging time, and is coded to 0, 2, 3, 6, 9, 12 corresponding to 0, 40, 60, 120, 180 and 240 days' aging. ε is the Gaussian error term. For BV, because only SH aging was performed, the simple GLM model is used

$$\sigma_s = \beta_0 + \beta_1 X_1 + \varepsilon \quad (2-12)$$

where σ_s represents the short beam strength with the unit of MPa. Design factor X_1 represents the aging time, and is coded to 0, 2, 3, 6, 9, 12 corresponding to 0, 40, 60, 120, 180 and 240 days' aging. ε is the Gaussian error term. The analysis is similar to that in the previous section and the regression results are shown in Table 2.11 below.

The changes of short beam strength in warp direction in freeze-thaw cycling are shown in Figure 2.12 (a) and (c). The data at freeze-thaw cycle -5 is the unexposed data, while the data at freeze-thaw cycle 0 is the short beam strength for the specimens which stayed in saturated sodium chloride solution for 10 days at room temperature before experiencing any freeze-thaw cycle. Obviously from this Figure, immersion in salt water decreased the short beam strength of BE. If a two-sample t-test with combined variance is used [219] with a null hypothesis (unexposed BE specimen short beam strength = that of the BE specimens aged in salt water for 10 days), and the alternative hypothesis (the former > the latter), the P-value for such test is 0.001, which demonstrates that salt water immersion at room temperature for only 10 days degraded the short beam strength of BE significantly. If the same analysis is performed on GE-443 and BV, P-values of 0.677 and 0.274 are obtained, respectively, which indicates that immersion in salt water at room temperature for 10 days had but a negligible

effect on the short beam strength of GE-443 and BV. Once freeze-thaw began, freeze-thaw cycling up to 199 cycles, completed in 30 days, did not significantly degrade the short beam strength of the composites BE, GE-443 and BV, as demonstrated by the corresponding P-value = 0.836, 0.607 and 0.983 in Table 2.11. The fact that BE short beam strength didn't drop in freeze-thaw cycling doesn't mean that freeze-thaw cycling doesn't degrade the material, but BE was already degraded in salt water to some extent and the effect of 199 freeze-thaw cycles may have been small in comparison.

The changes in short-beam strength after SH and WH aging are shown in Figure 2.12 (b) and (d)~(f). Obviously the shear strength of BE degraded with aging time in both conditions, as demonstrated by the corresponding P-value smaller than 0.001, shown in Table 2.11. Besides, the shear strength of BE degraded differently in the two conditions, as indicated by the corresponding P-value of 0.011 in Table 2.11. Comparing the degradation of short beam strength of BE in WH and SH from Figures 2.12 (b) and (e), one is able to see that generally BE had lower short beam strength in WH than in SH. In these cases, the linear regression model is not adequate to describe the rapid degradation and subsequent stable values of short beam strength. Nevertheless, the data in Figures 2.12 (b) and (e) may indicate the degradation depends on water activity. The greater degradation in pure water, Figure 2.12 (e), may occur because water activity is higher in pure water than in NaCl solutions. The difference in activity (fugacity) may change both the strength of the chemical interactions as well as the diffusion rate of water in the materials.

Table 2.11 Statistical Analysis for the Short Beam Strength under Aging

Short Beam Strength of BE in FTC (total d. f. * = 48)	Estimate	Standard Error (s_{β_i}) for β	t statistic (β/s_{β_i})	P-value
β_1 , time	-0.00274	0.0132	-0.21	0.836
Short Beam Strength of GE-443 in FTC (total d. f. * = 51)				
β_1 , time	0.00199	0.00385	0.52	0.607
Short Beam Strength of BV in FTC (total d. f. * = 43)				
β_1 , time	0.00032	0.0148	0.02	0.983
BE in SH and WH aging (total d. f. =76)				
β_1 , WH	-5.474	2.107	-2.60	0.011
β_2 , time	-1.741	0.252	-6.90	<0.001
GE-443 in SH and WH aging (total d. f. =60)				
β_1 , WH	-1.105	0.547	-2.02	0.048
β_2 , time	-0.127	0.0651	-1.94	0.057
BV in SH aging (total d. f. =28)				
β_1 , time	-1.236	0.486	-2.54	0.017
GV-443 in SH and WH aging (total d. f. =71)				
β_1 , WH	0.646	0.828	0.78	0.438
β_2 , time	0.0216	0.0947	0.23	0.820

For GE-443, similar results are obtained. The P-value for the regression coefficient β_1 is 0.048, which indicates that the material aged in WH and SH differently, while the P-value of 0.057 for β_2 indicates that the short beam strength didn't degrade significantly with aging at a

confidence level of 95%. Any decrease in GE-443 short beam strength was very small, as illustrated in Figures 2.12 (b) and (e). By similar statistical analysis, the shear strength of BV dropped significantly in SH aging, but that of GV-443 didn't change in SH or WH.

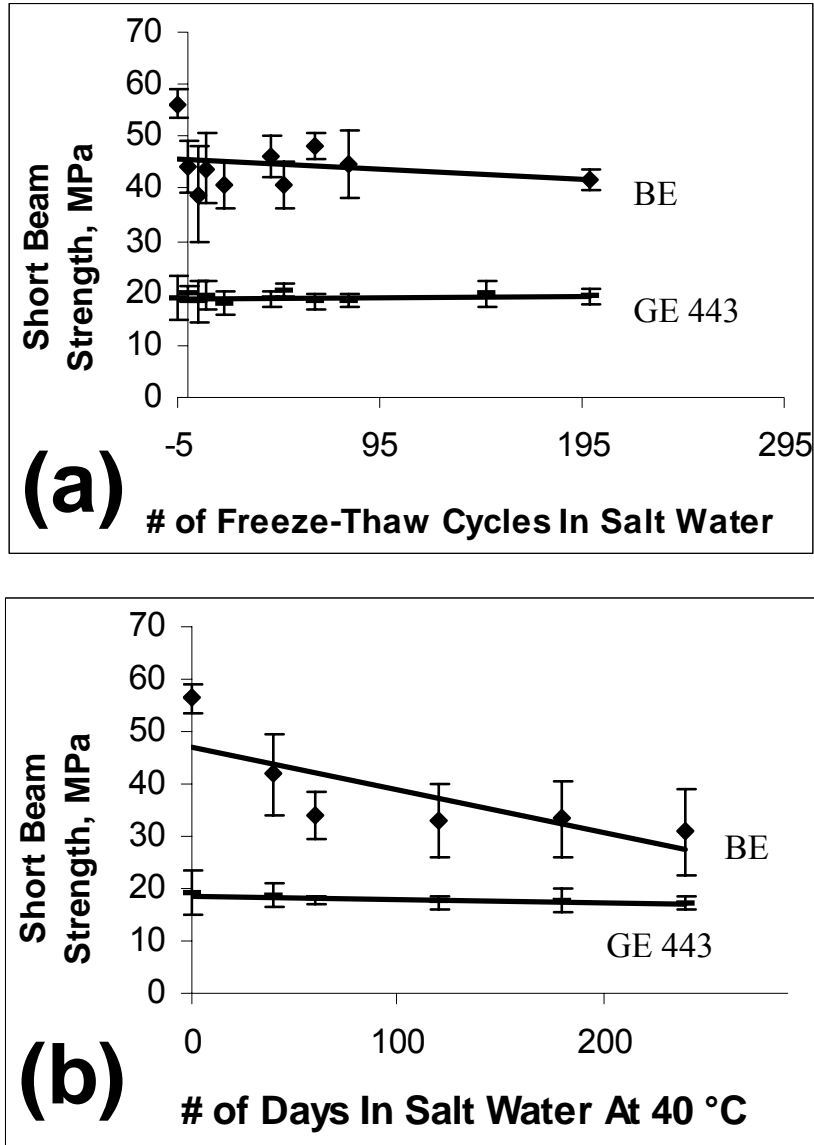


Figure 2.14 Aging data for Short Beam Strength in warp direction, for BE and GE-443. (a) In salt water experiencing freeze-thaw cycling. (b). In salt water at 40 °C.

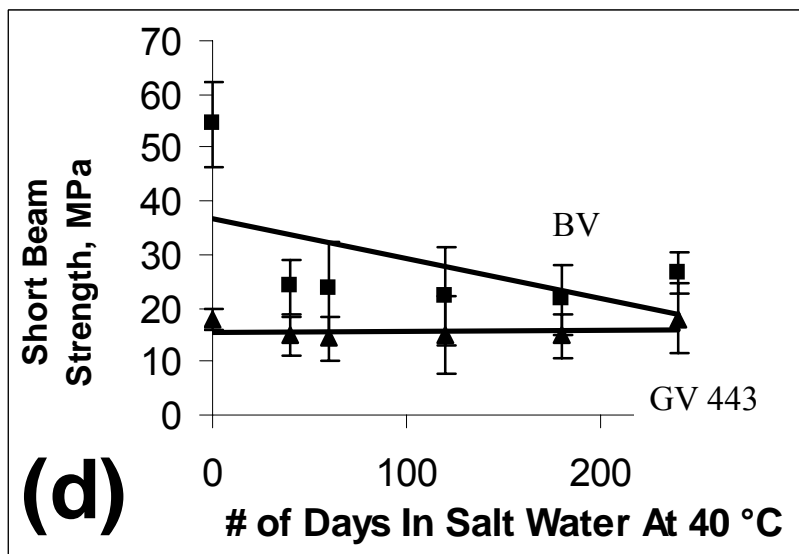
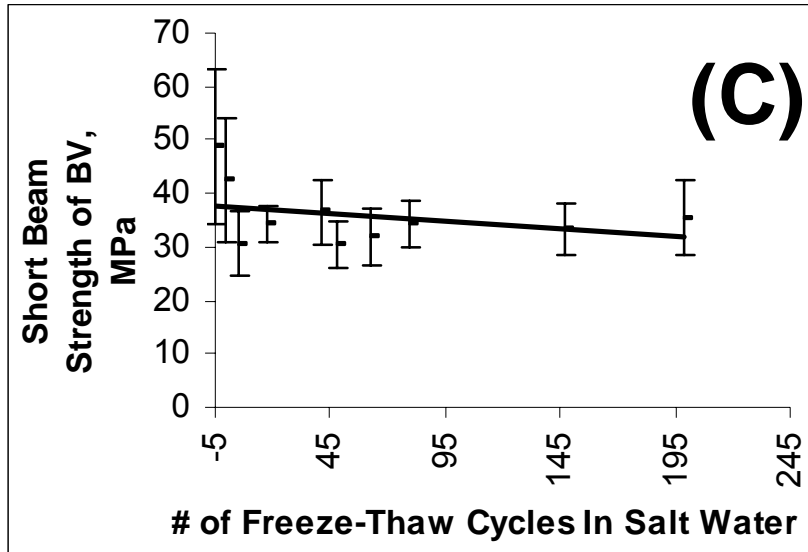


Figure 2.14 Aging Data for Short Beam Strength in Warp Direction, for BV and GV-443. (c) In Salt Water Experiencing Freeze-Thaw Cycling. (d). In Salt Water at 40 °C.

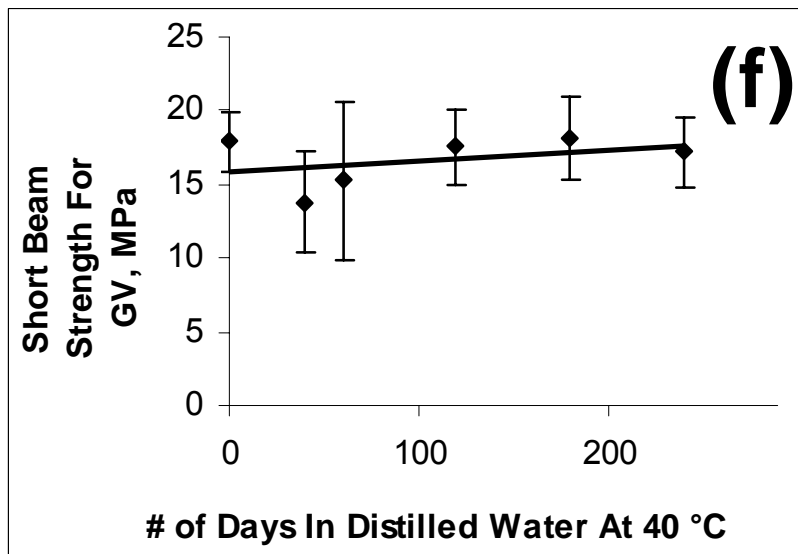
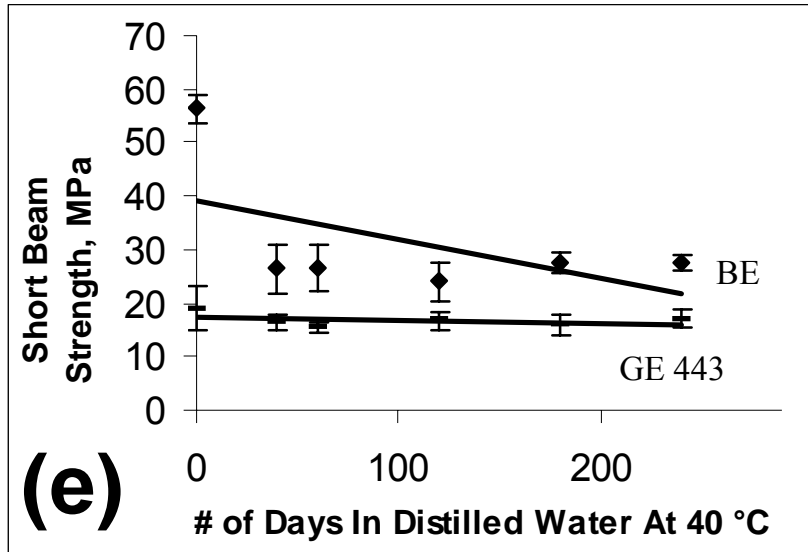


Figure 2.14 Aging Data for Short Beam Strength in Warp Direction in 40 °C Distilled Water, (e) for BE and GE-443 (f) for GV-443.

The changes of short beam strength for basalt composites with time were simplified by a generalized linear regression model shown in equation (2-12), $\sigma_s = \beta_0 + \beta_1 X_1 + \varepsilon$. The GLM was good enough to demonstrate the decrease of the short beam strength with time. However, it may be more appropriate to describe the relationship between short beam

strength of basalt composites and time by a nonlinear model, as indicated in Figure 2.13 (b), for example. A nonlinear model can be constructed as

$$\text{Ln}(\sigma_s) = \beta_0 + \beta_1 X_1 + \varepsilon \quad (2-13)$$

where the signals still represent the same variables as those in equation (2-12). Consider the short beam strength change for BE in salt water at 40 °C, perform the regression for GLM (2-13) and the results are shown in Table 2.12 below. The regression results for this model (2-13) demonstrated the same results as before: the short beam strength of BE decreased with aging time in 40 °C salt water. The relationship between short beam strength (in log scale) and time is shown in Figure 2.15, from which one can see clearly that this relationship looks more linear. Since the regression results for GLM (2-13) are basically the same as those for GLM (2-12), only the case of BE aging in 40 °C salt water is shown here.

Table 2.12 Statistical Analysis Results for the Short Beam Strength
Of BE under Aging in 40 °C Salt Water

Short Beam Strength of BE in 40 °C salt water (total d. f.* = 39)	Estimate	Standard Error (s_{β}) for β	t statistic (β/s_{β})	P- value
β_1 , time effect, (d. f.=5)	-3.30793	0.03122	-105.96	0.000

* d. f. represents degree of freedom

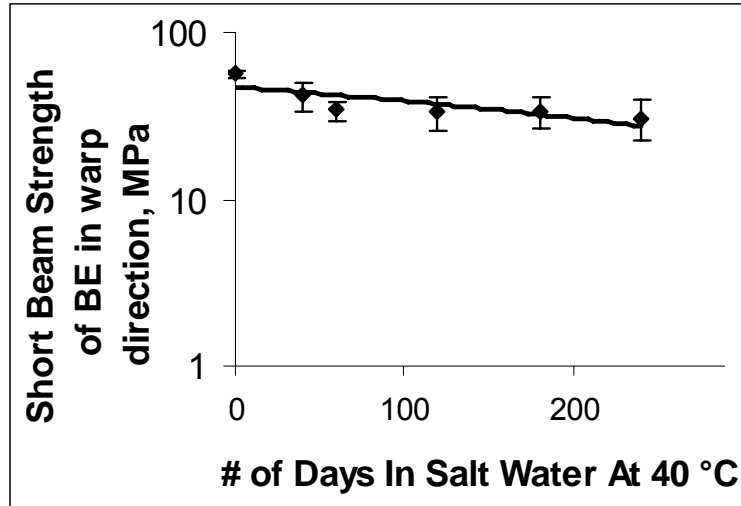


Figure 2.15 Aging Data in 40 °C Salt Water for Short Beam Strength (in log scale) of BE in Warp Direction

3. Discussion

The results from the tensile tests can be summarized very simply. Significant decreases were found in the moduli of BE, BV, and GV-443, but not GE-443, and also a significant decrease was found in the tensile strength of BE. Only small or insignificant decreases in tensile strength of the other composites were obtained. In short-beam shear, significant decreases in short-beam strength for BE and BV were found, but not for GE-443 or GV-443, and these differences were most likely due to changes in the failure mechanism.

Changes in the composite properties due to environmental aging may be due to degradation of the fiber, polymer, or interfacial properties. Under environmental aging, the polymer matrix may plasticize [114], as indicated by our high pressure (2.1 MPa) DSC results. For example, unexposed epoxy has an onset glass transition temperature of 74°C, and epoxy in saturated sodium chloride solution for 60 days has a T_g of 66°C. In the cases reported here, the modulus of the polymer matrix is relatively unimportant, since the fiber in the load direction dominates the modulus [5]. If the fiber was damaged, the interface was probably also damaged. Therefore, in the aging tests of the composites, either the interface alone or both the interface and fiber are damaged and cause degradation of composite properties.

If the interface is degraded but the fiber is not, expect decreases in the Young's modulus for textile reinforced composites [110-112, 114-116, 119, 120]. Changes in interfacial interactions have a complex effect on tensile strength [5]. In most cases, aging decreased the tensile strength of composites, but previous work did not clearly differentiate cases with only interfacial damage from cases with both interfacial and fiber damage [110-116, 119, 120, 122]. The current aging data also does not allow us to differentiate the case of interfacial damage alone from the case of interfacial and fiber damage.

Part II demonstrated that fiber damage due to heat treatment has a significant impact on composite tensile strength. The current tensile results show insignificant changes in strength. Therefore, the fibers were probably undamaged by the aging conditions used in this study. Also, fiber damage due to heat treatment did not significantly decrease Young's modulus. The current data show decreases in modulus for BE, BV, and GV-443. Since the fibers were probably undamaged, the decrease of the Young's modulus is attributable to interface damage alone. Note, that the GE-443 did not suffer a significant decline in Young's modulus or tensile strength, indicating that the GE-443 interface may be more stable than the other composite systems.

The result that the basalt-composite interfacial area is vulnerable to environmental aging was described previously [224, 225]. Palmese and Chawalwala [225] made polyester composites filled with basalt powder, and aged them in freeze-thaw cycling. They found that the flexure strength of the composites dropped to about 60% of that of the unaged ones after 500 cycles, and examination of the fractured surface indicated basalt-matrix debonding. Park and Subramanian [224] showed that exposure of basalt single-fiber fragmentation specimens to boiling water for one hour decreased the interfacial shear strength by 40%.

In short-beam shear tests, expect to observe significant decreases in short-beam strength if the interface is degraded and the sample fails in shear. This was observed for the BE and BV materials, shown in Figure 2.12 and Table 2.11. However, the GE-443 and GV-443 composites did not show decreases in short-beam shear strength. This would appear to be inconsistent in the case of GV-443 since a significant decline in Young's modulus was observed for GV-443 in tensile testing. A clear difference in failure mechanism was noted in

the glass reinforced composites during short-beam tests. The GE-443 and GV-443 both failed in tension during short-beam shear tests, and therefore, these tests did not properly assess the interfacial shear strength of the GE-443 and GV-443.

II. Fatigue Results

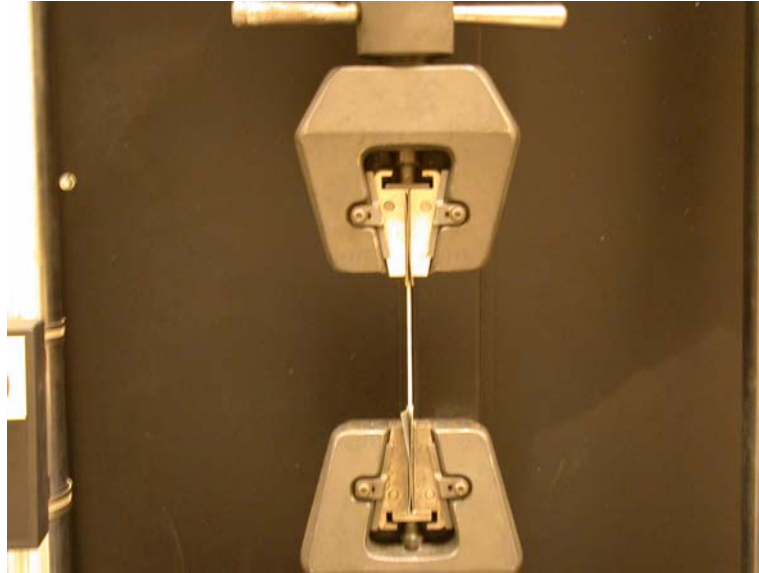


Figure 2.16 Fatigue Test

Tension-tension fatigue test is shown in Figure 2.16. The static tension and compression tests also look like Figure 2.16, except that in tension tests a strain gauge extensometer was hooked on the tensile specimen, and in compression tests the gauge length is very short (10~15 mm) to avoid the Euler buckling phenomena [222]. These fatigue tests were performed on BE and GE 1527-350 which were produced by compression molding method, and basalt epoxy composites produced by RTM methods (denoted as BE-RTM). The tensile strength and void content for BE-RTM were (150.5 ± 7.6) MPa and 1%, respectively. The error for the void content results was estimated as 2% roughly, as discussed before in part I, chapter III. The fatigue test frequency was 0.5 Hz due to the limit of the machine. The control mode was load control, with a minimum load of 500 N. The maximum tensile stress used equals 65%, 50% and 40% of the ultimate tensile strength of the specimens. It is noteworthy that when the maximum stress was 65% of the tensile strength, a Tinius-Olsen servo-mechanical tensile tester, with a 12,000 pound load cell was used. The computer software for the tester was the MTestW Materials Testing System from Admet, Inc. in

Norwood, MA. However, for easy operation, another machine was used, Instron MP5832 (S/N), with a load cell of 10,000 pound, for the tests at 50% and 40% of ultimate tensile strength, with the assumption that there was no effect from the machines on the fatigue life measured. The Instron MP5832 is operated through a control panel of Fast Track 8800 system, which can be accessed through Fast Track software in the computer. The sine wave was used as the format of the undulating movement of force versus time. In the fatigue tests, the number of cycles was recorded for the specimen to fail under the specified condition, and that number is defined as fatigue life, realizing that one cycle takes 2 second under the frequency of 0.5 Hz. After that, the distribution was found which best fitted the data of fatigue life for the same material according to Anderson-Darling tests [203].

Table 2.13 lists the raw data and Table 2.14 lists the best distribution fits for the fatigue life and the corresponding 95% confidence intervals calculated with the given distributions. When the maximum tensile stress is 40% of the tensile strength, only a few results were obtained because the test typically takes a long time (a few weeks). Such a small number of test results cannot supply a valid estimation for distribution. Distribution curves are graphed for the fatigue life of different materials when the maximum tensile stress is 65% and 50% of the tensile strength in Figure 2.17 and 2.18 respectively. In these figures, for easy observation, the probability density curves are scaled.

When the maximum stress is 65% of the tensile strength, there is no obvious difference in the fatigue life between the three composite materials, considering the large overlap of the distribution curves near the peak positions. However, when the maximum stress is decreased to 50% of the tensile strength, BE appears more durable in the fatigue test than GE 1527-350 and BE-RTM, because the peak position of the distribution curve for BE fatigue life is located in a much higher position. When the maximum stress is 40% of the tensile strength, the differences are very clear although there are only a few data points. The reason for the difference in the fatigue life between BE and BE-RTM could be that BE-RTM has higher void content than BE, in that the former has a void content of 0% and the latter has 1% according to our measurement shown before in Table 2.4. However, the fatigue life is not very sensitive to the void content at low level of maximum stress [5], i.e., the fatigue life is not very sensitive to the void content when the maximum stress is less than 50% of the

ultimate strength. Besides, in the void content measurement, the accuracy is about 2%. Therefore, the reason of void content difference deserves much debate. Another reason could be that the materials were made from different procedures: hand lay-up and RTM. In RTM, the epoxide liquid (Epon shell 828) might wet the fiber surface not as well as it did in the hand lay-up procedure. So the interfacial bonding strength in the BE composites is better than that in BE-RTM composites. Under low stress levels (high fatigue life), the fatigue sensitivity of the matrix and interface may be as important as the fibers themselves [5].

For the difference in fatigue life between BE and GE 1527-350, it may be due to the difference in fiber fatigue sensitivity, i.e., the basalt fiber is more mechanically durable than glass fiber, or due to the fact that the interfacial region in BE is more mechanically durable (less fatigue sensitive).

Table 2.13 Raw Data in Fatigue Tests for the Composites

Materials	Tensile Strength, MPa	Maximum Stress/Tensile Strength		
		65%	50%	40%
BE-RTM	150.5±7.6	59, 50, 35, 25, 75, 108, 49, 55, 72	23282, 14493, 20963, 10339, 73615, 15769	330826, 213215
BE	160.4±10.0	22, 77, 26, 41, 86, 106, 143	17982, 22855, 53850, 46982, 58103, 66413	531990, 638680
GE 1527-350	210.6±28.8	64, 53, 49, 32, 220, 62, 81	10648, 15140, 37137, 68799, 41256, 13694, 10190, 8551	45212, 48132, 31460

Table 2.14 Fatigue Test Results for the Composites, Distribution Fit

Materials	Distribution and 95% C. I. when maximum stress is 65% of tensile strength
BE-RTM	Lognormal, (39, 75) $f(x) = \frac{1}{0.4295\sqrt{2\pi x}} \exp\left\{-\frac{(Lnx - 3.993)^2}{0.3689}\right\}$
BE	Weibull, (52, 124) $f(x) = \left(\frac{1.81}{80.64}\right)\left(\frac{x}{80.64}\right)^{0.81} \exp\left[-\left(\frac{x}{80.64}\right)^{1.81}\right]$
GE 1527-350	Lognormal, (38, 116) $f(x) = \frac{1}{0.5987\sqrt{2\pi x}} \exp\left\{-\frac{(Lnx - 4.202)^2}{0.7169}\right\},$
Materials	Distribution and 95% C. I. when maximum stress is 50% of tensile strength
BE-RTM	Lognormal, (10280, 42754) $f(x) = \frac{1}{0.6791\sqrt{2\pi x}} \exp\left\{-\frac{(Lnx - 9.9510)^2}{0.9224}\right\}$
BE	Weibull, (37183, 67224) $f(x) = \left(\frac{2.83}{49997}\right)\left(\frac{x}{49997}\right)^{1.83} \exp\left[-\left(\frac{x}{49997}\right)^{2.83}\right]$
GE 1527-350	Lognormal, (10148, 37183) $f(x) = \frac{1}{0.7766\sqrt{2\pi x}} \exp\left\{-\frac{(Lnx - 9.8740)^2}{1.2062}\right\}$

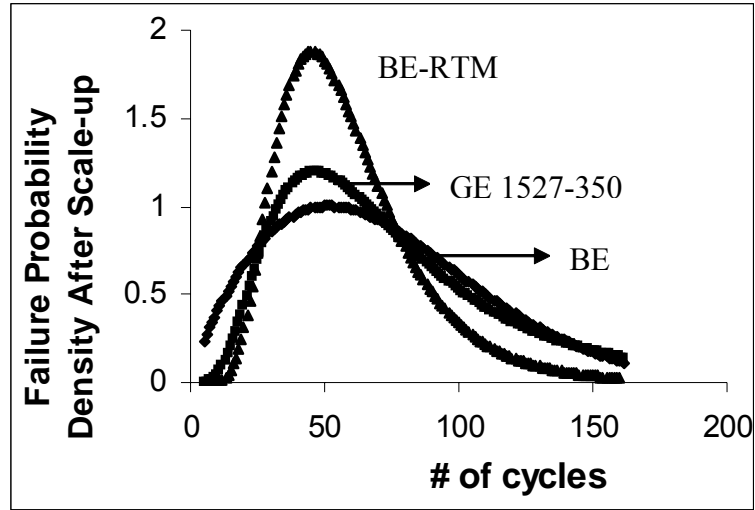


Figure 2.17 Comparison of Fatigue Life when Maximum Stress is 65% of Tensile Strength

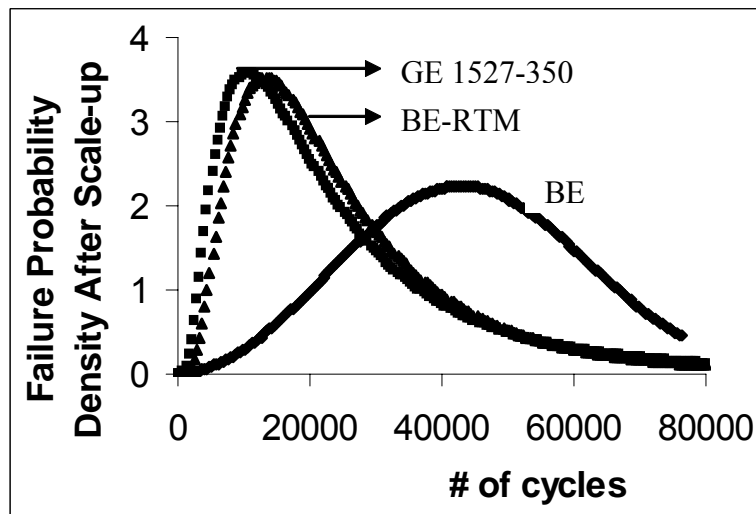


Figure 2.18 Comparison of Fatigue Life when Maximum Stress is 50% of Tensile Strength

Chapter 3. Permeability Measurement of Basalt Fabric

The permeability is an important parameter for producing polymer composites by liquid molding. Although the permeability does not directly affect the mechanical behavior discussed in the previous chapter, production quality plays an important role in determining material performance. Permeability plays a critical role in designing and operating liquid molding manufacturing facilities.

Based on the different available set-ups, especially the one developed by Hoes [13], et al, a new development is presented in this chapter for in-plane permeability measurement. Specifically, a new sensor design is developed for the in-plane set-up to permit the use of electrically conductive reinforcement, and Labview program is used to acquire data, control equipment and analyze data in a fast way. Besides, a new derivation procedure for the flow pattern from the triggering time of the sensors is developed which doesn't need the time-consuming processing of the digital pictures taken from the experiments, or the assumption that the permeability principal directions coincide with the material coordinates in Hoes' set up [13]. The new set-up was used to measure the permeability of a basalt woven twill fabric. The results showed some similarity with those for another glass twill fabric, as discussed below in the results section. And a high correlation was found between the permeability values in the warp and those in the weft direction.

Part I. Hardware Design

The central parts are two sensor plates: top plate and bottom plate, which are made of stainless steel, about 40 cm long and wide, and 3.2 cm thick. The thick metal plates don't have any deflection problem. On the back of the plate, channels of 1.9 cm wide were opened along every 22.5°. Six or 7 evenly spaced sensors are inserted into the channels along each angle. The front end of the sensor can be seen from the front of the plate, and it either sits on the same level of the plate surface for non-conductive fabrics or recesses a little bit down for conductive fabrics like carbon fabrics. The back end of the sensor is soldered to a ribbon cable, which goes to the DAQ cards inside the computer, PCI-DIO 96. Two DAQ boards

PCI-DIO 96 are inside the computer, one for the top plate and the other for the bottom one. There are 96 digital channels for each board, so 96 sensors are used for each plate. The view of the top plate is shown in Figure 3.1, and the bottom plate looks similar except that there is a hole in the center for fluid injection. In the center of the top plate, a sensor sits here to sense the coming fluid, i.e., when the fluid reaches this sensor, the computer program begins to count time. The radius of the hole is about 3.188 mm. And a hole of the same size is punched in the middle of the fabric to conduct fluid, so that fluid can expand along the top and bottom layers relatively simultaneously.

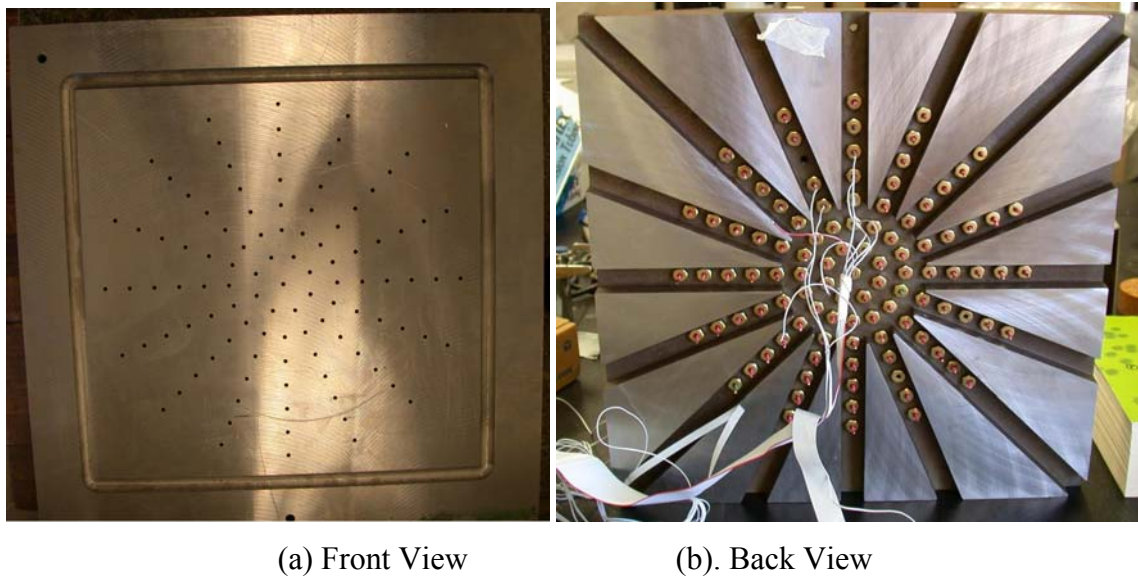


Figure 3.1 Top Sensor Plate

The sensor is basically a copper wire with nylon jacket. The sensor is fixed into the metal plate through the screw, and usually the sensor flushes with the surface. The O-ring is compressed when the sensor is screwed into the plate and so the O-ring seals the space and locks the wire. The sensor is electrically insulated from the metal plate initially. During the experiment, the computer offers 5 V potential to each sensor, while the plate is grounded. Whenever the conductive fluid reaches the sensor, it conducts electricity between the sensor and the metal plate. So it drops the potential of the sensor to below 0.8 V. This way the digital input which connects the sensor changes its state from on to off because its potential changes from 5V to below 0.8 V. The electric diagram is shown in Figure 3.2 below.

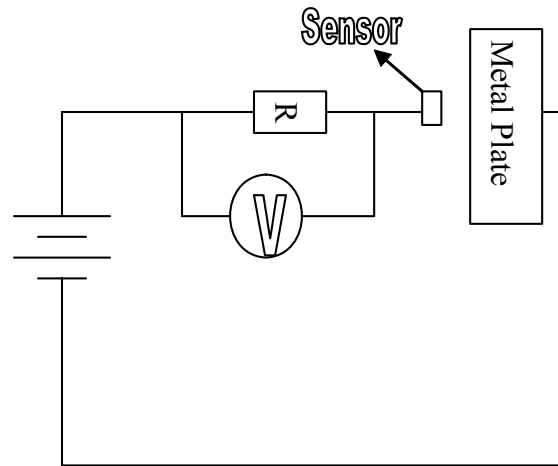
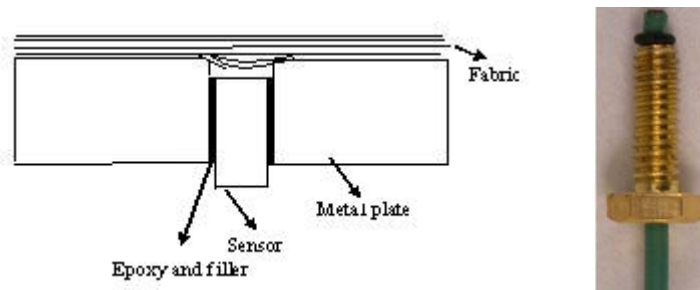


Figure 3.2 Electrical Diagram

The design allows the sensor to be slightly recessed below the plate level, to prevent the compressed electrically conductive fabric from touching and shorting out the sensors (See Figure 3.3). During an injection the electrically conductive fluid fills the small gap between the sensor core and the conductive fabric, thus still generating a trigger signal for the data-acquisition system. In this way the in-plane permeability values can also be measured for electrically conductive fabrics such as carbon.



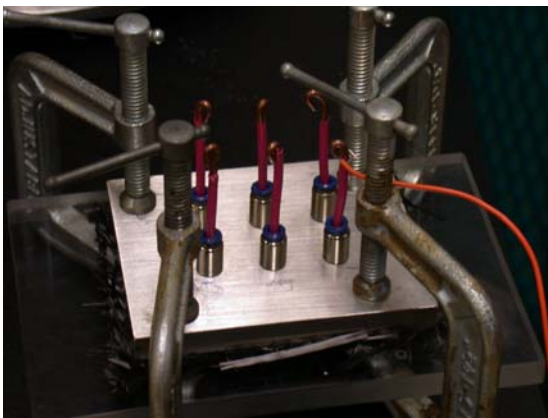
(a). Schematic Drawing (b). Sensor Used

Figure 3.3 Recessed Sensor

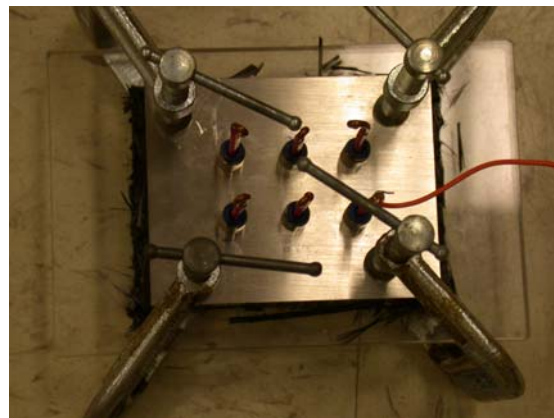
Experiments demonstrated the applicability of the proposed design. A prototype was designed as follows. A small rectangular metal plate was used with six evenly distributed sensors. The sensor plate is similar to the one used in Hoes' work [13]. The sensors

themselves consist of a metallic core with a diameter of 2 mm. The core is fitted in a hole with diameter 5 mm and is electrically isolated from the plate by a nylon screw in which a hole is drilled to hold the core. The sensor core is left unsupported for about 5mm from the top surface. This gap is then filled with an epoxy and filler mixture, after which the plate is machined flat. The design is shown in Figure 3.4 below. Then each sensor is recessed down by a small distance d . A piece of carbon fabric was placed on top of the sensor plate and compressed by means of a plexy glass plate of the same size. The plexy glass was used in order for us to visually observe the flow front.

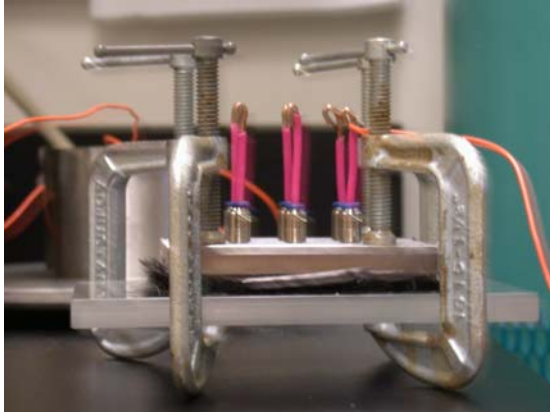
The sensor, used as a digital input, is connected to the Data Acquisition card in the computer, PCI-DIO 96 produced by Measurement Computing Company [199]. By properly recessing the sensor, the carbon fabric doesn't touch the sensor so it doesn't conduct electricity between the sensor and the metal plate. This time the sensor has a potential of 5 V. When fluid reaches any sensor, it behaves as an electric bridge between the sensor and the metal plate which is grounded. By properly choosing the internal resistor, the potential of the sensor is dropped to below 0.8 V, and the sensor is triggered because the state of the DIO (Digital input/output, here we use digital input) changes from 1 to 0. From the Test Panel of the DIO board, the triggered sensors are observed through the color change. Therefore, this design is good for electrically conductive carbon fabric. The view of the Test Panel is shown in Figure 3.5 below.



(a) From Above



(b) From Above

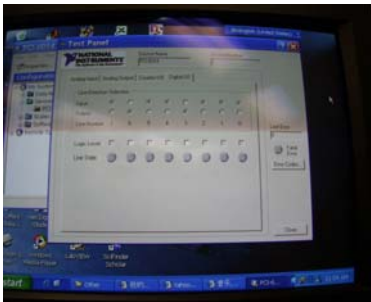


(c) Front View

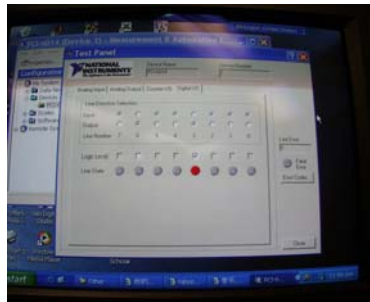


(d) From below

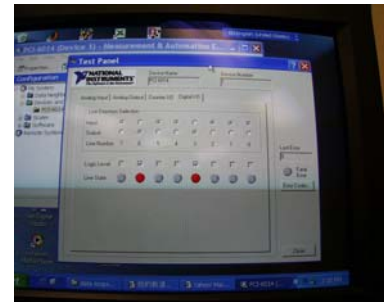
Figure 3.4 Prototype Design



(a) Untriggered



(b) One Sensor Triggered



(c) Two Sensor Triggered

Figure 3.5 View of the Front Panel

In our design, a pressure transducer is hooked up near the injection hole to measure the inlet pressure and the entrance effect is considered. The pressure transducer was calibrated by connecting it with a monometer filled with mercury and a nitrogen tank using a T connector. The pressure transducer is also connected with an analog input. Adjust the output pressure of the nitrogen tank carefully, read the pressure of the nitrogen tank through the mercury height difference in the monometer, and also read the output voltage from the pressure transducer through the analog input. This way a linear relationship between the pressure reading and the voltage output from the pressure transducer is constructed. Later the computer program used this relationship to calculate the inlet pressure from the analog input reading. The scheme is shown in Figure 3.6 below. Figure 3.7 below describes the relationship between the reading from the analog input and the pressure measured by the pressure transducer.

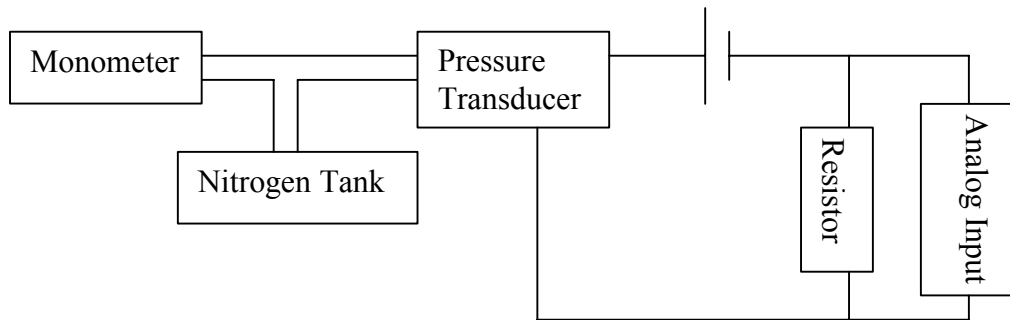


Figure 3.6 Scheme of Calibrating the Pressure Transducer

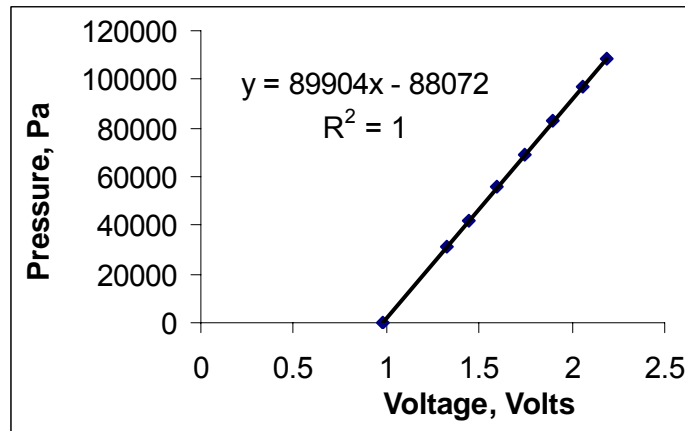


Figure 3.7 Calibration Result of the Pressure Gradient

The fluid is pumped into the equipment by a Masterflex I/P pump with model no. 77601-10. Before the fluid reaches the injection hole it passes through a flow meter, whose control valve can be adjusted to keep a constant injection flow rate. The flow meter was also calibrated using fluids with difference viscosity values. First the DCS fluid was mixed and its viscosity measured. Pumping such fluid through the flow meter, conducting the fluid from the exit of the flow meter to a large measuring tube (with a capacity of 1000 ml), adjusting the knob so that the flow meter reading was kept stable, then the time was recorded for the fluid to fill a volume (usually 900 ml). Dividing the volume by the time, calculate the flow rate. This way a relationship was constructed between the flow meter reading and the flow rate for a fluid with a fixed viscosity. Then the viscosity of the fluid was changed, and the procedures above repeated to obtain another relationship for another viscosity. Three such

relationships were constructed so that the flow rate is known from the flow meter reading and the fluid viscosity.

The whole equipment is shown in Figure 3.8. The experiment is monitored and controlled through Labview software. The information from the top plate (sensor trigger time) and that from the bottom plate is used separately to derive the flow pattern and in-plane permeability. If the answers from the two plates do not correspond with each other, the assumption that the permeability tensor lies in the plane of the material may be false. That is, the two principal permeabilities, K_{xx} and K_{yy} may not stay in the material plane. The fluid used is Diluted Corn Syrup (DCS), made of distill water and corn syrup bought from the supermarket (Light Corn Syrup with the brand name of ‘Nugget’, and bar code 4410502883). The weight ratio of corn syrup to distill water is 11:3, which gives the mixture a viscosity around 0.1 Pa·s at room temperature. The viscosity of the DCS is measured before and after the injection experiment and the average is used. From reference it is known that DCS is widely used as a Newtonian fluid [13]. In the experiment, the viscosity of DCS is measured over a wide range of shear rate to make sure the fluid has Newtonian behavior. The measurement result is shown in Figure 3.9 below.

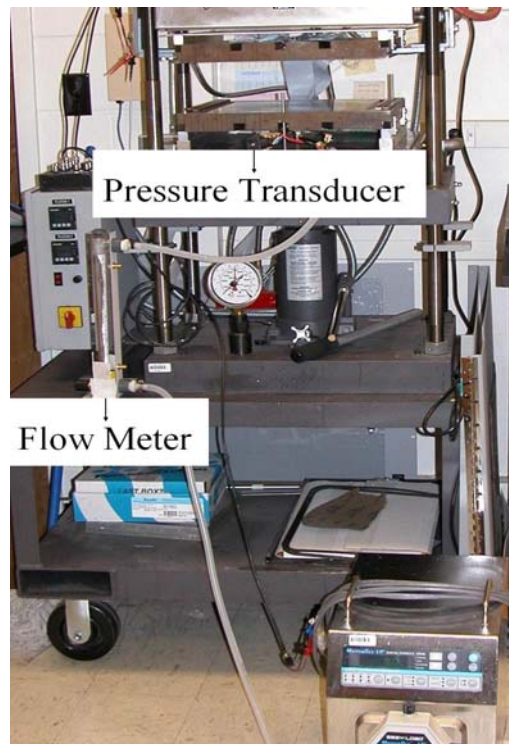


Figure 3.8 The Whole Equipment

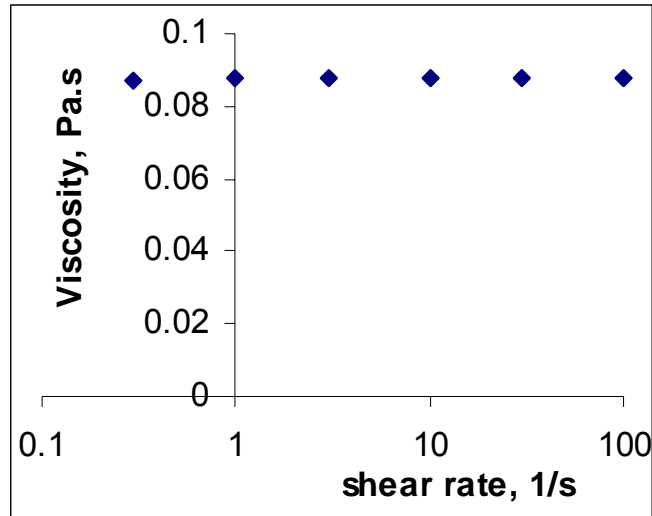


Figure 3.9 Measurement Result of the DCS Viscosity

Part II. Algebra of the Data Derivation

I. Derivation of Sensor Trigger Time

The fluid flow front is an ellipse, as shown in Figure 3.10 below. The blue area represents the area covered by the fluid, and the small white circle in the center represents the central injection hole. The material coordinate is the x' , y' system, and x' is defined as the warp direction. x , y are the directions of two permeability principal coordinates, usually $K_{xx} > K_{yy}$ is assumed. Finding the anisotropic ratio of the permeability, K_{xx}/K_{yy} or $(a/b)^2$, and the position of the permeability principal directions, the magnitude of θ angle, are the goals.

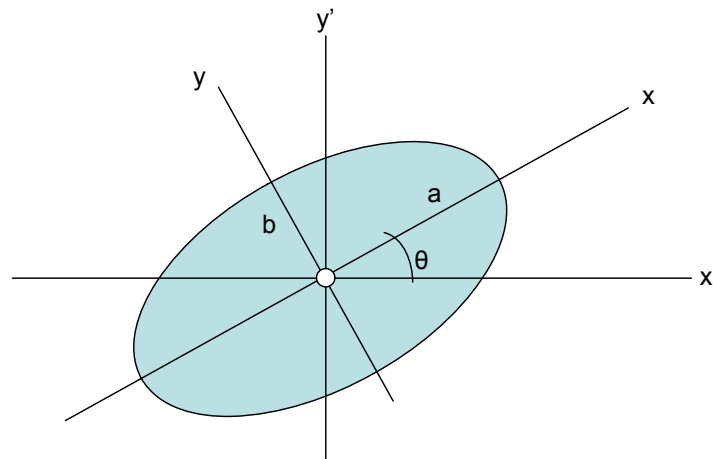


Figure 3.10 Fluid Flow Front

In x, y coordinate system, the equation of the ellipse is written as

$$\frac{x^2}{a^2} + \frac{y^2}{b^2} = 1 \quad (3-1)$$

The relation of a, b with time t

$$\pi(ab - r_0^2)h\phi = Qt \quad (3-2)$$

where t is time,

Q is injection flow volume rate, which is controlled,

r_0 is injection radius,

h is thickness of the preform, which is controlled,

Φ is porosity, which is controlled.

When the sensor in the center of the top sensor plate is triggered, the time is set equal to zero and the experiment clock starts running.

Equation (3-2) can be simplified to

$$ab = \frac{Q}{\pi h \phi} t + r_0^2 \quad (3-3)$$

And equation (3-3) can be further simplified to

$$ab = m_1 t + m_2 \quad (3-4)$$

where $m_1 = \frac{Q}{\pi h \phi}$, and $m_2 = r_0^2$, both are known.

Assumption: $a > b$, and both are large enough for us to omit the effect from the injection hole.

Define anisotropic ratio of the ellipse (unknown):

$$m_3 = a/b \quad (3-5)$$

The combination of equation (3-4) and (3-5) gives us the expression of a and b in terms of m_1 , m_2 and m_3 :

$$a = \sqrt{m_3(m_1 t + m_2)} \quad (3-6)$$

$$b = \sqrt{(m_1 t + m_2)/m_3} \quad (3-7)$$

Now, the line in which the sensor sits is:

$$y = x \tan(\alpha - \theta) \quad (3-8)$$

where $\alpha = 0, 22.5, 45, 67.5, 90, 112.5, 135, 157.5$ degree.

The cross points of the sensor line with the ellipse:

$$x_0 = \frac{\pm ab}{\sqrt{b^2 + a^2 \tan^2(\alpha - \theta)}}, \quad y_0 = x_0 \tan(\alpha - \theta) \quad (3-9)$$

The distance between the cross points and (0, 0) is

$$d = ab \sqrt{\frac{1 + \tan^2(\alpha - \theta)}{b^2 + a^2 \tan^2(\alpha - \theta)}} \quad (3-10)$$

From the relation between a, b and time, i.e. equation (6) and (7), obtain

$$d = \sqrt{\frac{(m_1 t + m_2)(1 + \tan^2(\alpha - \theta))}{\frac{1}{m_3} + m_3 \tan^2(\alpha - \theta)}} \quad (3-11)$$

Equation (3-11) describes the relationship between fluid flow distance along any angle α and time. Or the time when fluid reaches any radius on the line with angle α from x' axis can be expressed as:

$$t = \frac{d^2 [1 + m_3^2 \tan^2(\alpha - \theta)]}{m_1 m_3 [1 + \tan^2(\alpha - \theta)]} - \frac{m_2}{m_1} \quad (3-12)$$

In real system, like our system, the initial flow rate fluctuates a little bit, so the algebra requires a modification. If flow rate varies before t_1 and stabilizes as Q after t_1 , then equation (3-3) becomes

$$ab = \frac{Q}{\pi h \phi} (t - t_1) + a_1 b_1 = \frac{Q}{\pi h \phi} t + a_2 b_2 \quad (3-13)$$

In equation (3-13), $a_1 b_1$ represents the area filled before the flow rate stabilizes during time $t < t_1$. If during this period, the averaged unknown flow rate is less than Q , then $a_2 b_2 < 0$, otherwise $a_2 b_2 > 0$.

Define $m_2 + c = a_2 b_2$ (3-14)

Equation (3-4) becomes

$$ab = \frac{Q}{\pi h \phi} t + m_2 + c = m_1 t + m_2 + c \quad (3-15)$$

where c is an unknown constant, and it can be positive or negative depending on the sign of $a_2 b_2$.

Then equation (3-11) becomes

$$d = \sqrt{\frac{(m_1 t + m_2 + c)(1 + \tan^2(\alpha - \theta))}{\frac{1}{m_3} + m_3 \tan^2(\alpha - \theta)}} \quad (3-16)$$

And equation (3-12) becomes

$$t = \frac{d^2 [1 + m_3^2 \tan^2(\alpha - \theta)]}{m_1 m_3 [1 + \tan^2(\alpha - \theta)]} - \frac{m_2 + c}{m_1} \quad (3-17)$$

In this equation the three unknown parameters are θ , m_3 and c . For each sensor triggered in the experiment, we have one such equation as (3-17). In the experiment, 50~60 sensors are usually triggered from each sensor plate, so there are 50~60 such equations from each sensor plate. Do the regression in Sigma-Plot and get the answers for the three unknowns. Due to flow rate fluctuations in the beginning, ignore the data in the first 5 seconds which is enough to include the fluctuation region. After the first 5 seconds, the flow rate is constant.

II. Permeability Calculation Procedure

In the x, y coordinates system, Darcy velocity, v_r can be written as

$$v_r = v_{r0} \phi \quad (3-18)$$

where v_{r0} is the fluid velocity inside the pores. According to Darcy law,

$$v_r = -\frac{K_{rr}}{\mu} \frac{\partial P}{\partial r} \quad (3-19)$$

where K_{rr} is the permeability in the isotropic permeability case, μ is the fluid viscosity of the fluid, $\frac{\partial P}{\partial r}$ is the pressure gradient.

According to mass balance:
$$v_r r = \frac{Q}{2\pi h} \quad (3-20)$$

Combine equation (3-19) and (3-20) to obtain

$$\frac{Q}{2\pi h r} = -\frac{K_{rr}}{\mu} \frac{\partial P}{\partial r} \quad (3-21)$$

Integrate equation (3-21) to get

$$\Delta P = P_{in} = \frac{\mu Q}{2\pi h K_{rr}} \ln \frac{R}{r_0} \quad (3-22)$$

where P_{in} is the inlet pressure measured by the pressure transducer, i.e., the injection pressure minus the atmospheric pressure, R is the radius of the flow front.

$$\text{From Equation (3-21) \& (3-22), } \quad \frac{\partial P}{\partial r} = -\frac{P_{in}}{r \ln(R/r_0)} \quad (3-23)$$

$$\text{Mass balance tells us:} \quad 2\pi r dr h \phi = Q dt \quad (3-24)$$

If the flow rate is constant from the beginning, i. e., Q is constant in equation (3-24), equation (3-24) is integrated to provide

$$\frac{R}{r_0} = \sqrt{\frac{Qt}{h\pi\phi r_0^2} + 1} \quad (3-25)$$

Substitute equation (3-25) to (3-22) to obtain

$$P_{in} = \frac{\mu Q}{4\pi h K_{rr}} \ln\left(1 + \frac{Qt}{\phi\pi h r_0^2}\right) \quad (3-26)$$

Plot P_{in} versus $\ln\left(1 + \frac{Qt}{\phi\pi h r_0^2}\right)$, the slope is $\frac{\mu Q}{4\pi h K_{rr}}$. This result provides K_{rr} , the geometric permeability. Therefore, K_{xx} and K_{yy} are obtained using:

$$K_{rr} = \sqrt{K_{xx} K_{yy}}, \text{ so } K_{xx} = K_{rr} m_3, \text{ and } K_{yy} = K_{rr} / m_3 \quad (3-27)$$

Equation (3-26) describes the relationship between P_{in} and time in case of constant flow rate injection experiment, and is same as that in the reference [8].

However, due to flow rate fluctuations in the beginning, integrate equation (3-24), and according to the isotropic case of equation (3-16), obtain

$$R^2 = m_1 t + m_2 + c = \frac{Q}{\pi h \phi} t + r_0^2 + c = r_0^2 \left(1 + \frac{c}{r_0^2} + \frac{Q}{\pi h \phi r_0^2} t\right) \quad (3-28)$$

Therefore, instead of equation (3-25), there is

$$\frac{R}{r_0} = \sqrt{\frac{Qt}{h\pi\phi r_0^2} + 1 + \frac{c}{r_0^2}} \quad (3-29)$$

Substitute equation (3-29) into (3-22), then

$$P_{in} = \frac{\mu Q}{4\pi h K_{rr}} \ln\left(1 + \frac{Qt}{\phi\pi h r_0^2} + \frac{c}{r_0^2}\right) \quad (3-30)$$

Plot P_{in} versus $\ln(1 + \frac{Qt}{\phi\pi hr_0^2} + \frac{c}{r_0^2})$, the slope is $\frac{\mu Q}{4\pi h K_{rr}}$. Ignore the initial data of pressure in the first 5 seconds due to initial flow fluctuations. From the slope, derive K_{rr} , the geometric permeability. Use equation (3-27) to get K_{xx} and K_{yy} .

Part III. Experimental Results and Analysis

I. Permeability Measurement Results

The fabric used is basalt woven twill 3/1, from Albarrie company [200], Canada. The information about this fabric is shown in Table 3.1 below. Six layers of such fabric are used each time and they are compressed to 4.6615 mm and the resulted fiber volume fraction is about 35.75%. These layers of fabric are placed between the top and bottom sensor plates in a way that seen from above, each warp yarn goes over three weft yarns and under one. If the fabric is observed from the bottom, each warp yarn goes over one weft yarn and under three. The results of the basalt fabric are compared with those for some other fabrics. The results produced by Kris Hoes [13] for two glass fabrics, plain woven Syncoglas R420 and twill woven Syncoglas RE144/255 were chosen for comparison. These two fabrics are produced by Syncoglas company in Belgium [201]. Earlier results produced by Parnas (11, 13) for a CNF custom crowfoot, which came from Carolina Narrow Fabric company in United States [202] are also compared. The structure information of these fabrics is also listed in Table 3.1.

The results from 52 replicated measurements for in-plane permeability principle values K_{xx} and K_{yy} , and 64 replicated measurements for the permeability anisotropic ratio and the angle between the warp direction and the permeability principle axis K_{xx} were shown for the basalt fabric in Table 3.2. The data in each cell is (average \pm standard deviation) and the unit is Darcy for convenience, and $1 \text{ m}^2 = 1.01325 \times 10^{12}$ Darcy [155]. The angle θ , between the warp direction of the fabric and the permeability principle axis (the one with larger permeability values), is defined as the one going counter clockwise from the former to the later, seen from above in Figure 3.10. Since the data from the bottom and top plates are analyzed individually, independent results are obtained from both of them. The distribution is shown in Figure 3.11. The result from each experiment is listed in Table 3.3 below. In Table 3.3, the previous part of the ID represents the date on which the experiment was performed,

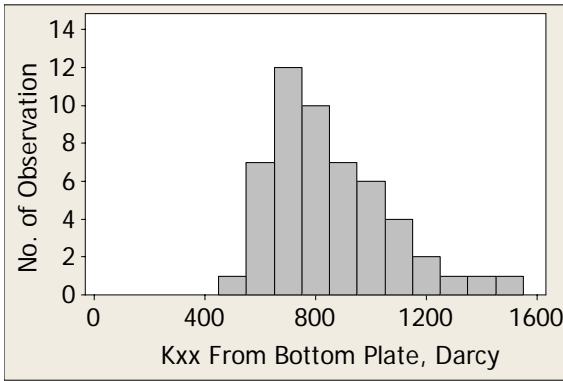
and the latter part after the signal ‘-’ represents the sequence. For example, 0405-2 represents the second experiment performed on April 5, 2005.

Table 3.1 Information of Basalt Fabric Used & Some Other Fabrics

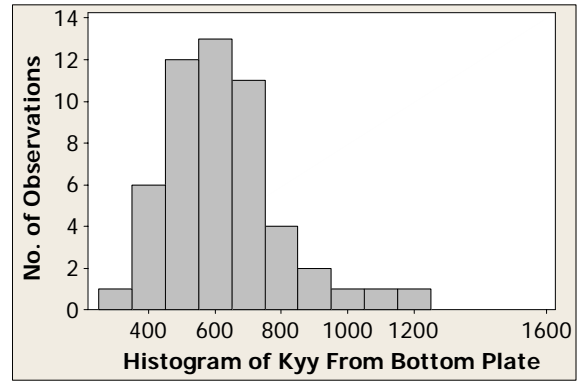
Properties	Basalt Fabric	Syncoglas R420	Syncoglas RE144/255	CNF crowfoot
Areal Density, g/m ²	750	420	380	2900
Fiber Density, g/cm ³	2.7	2.52	2.52	2.52
Warp Yarn Linear Density, tex (g/km)	660	600	310	66.14
Weft Yarn Linear Density, tex (g/km)	330	600	580	33.07
Weave pattern	Twill 3/1	Plain weave 1/1	Twill 2/2	Twill 3/1
Yarn number/10 cm in warp direction	59.5	36.0	45	220
Yarn number/10 cm in weft direction	78	34.0	40.8	213

Table 3.2 In-Plane Permeability Results for Basalt Fabric

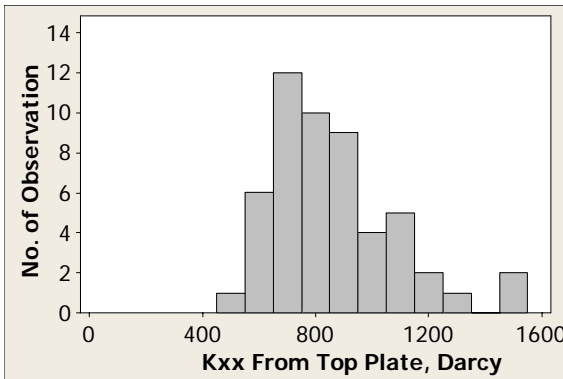
	Anisotropic ratio of permeability	angle γ , Deg	K_{xx} , Darcy	K_{yy} , Darcy
From Bottom Plate	1.374 ± 0.097	-3.47 ± 5.60	857.85 ± 218.88	625.71 ± 174.19
From Top Plate	1.389 ± 0.091	-6.34 ± 6.35	858.43 ± 227.46	617.98 ± 166.71



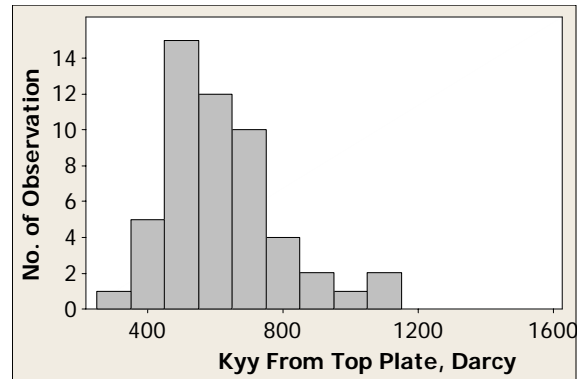
(a) Distribution of K_{xx} from the Bottom Sensor Plate



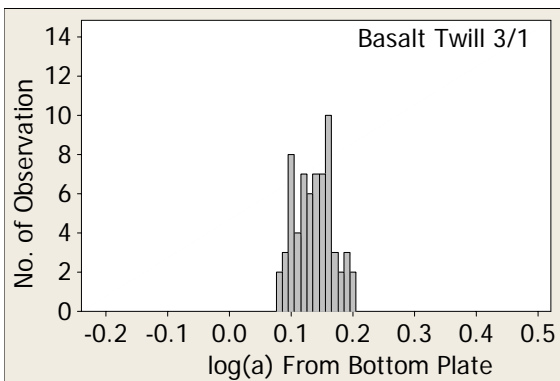
(b) Distribution of K_{yy} from the Bottom Sensor Plate



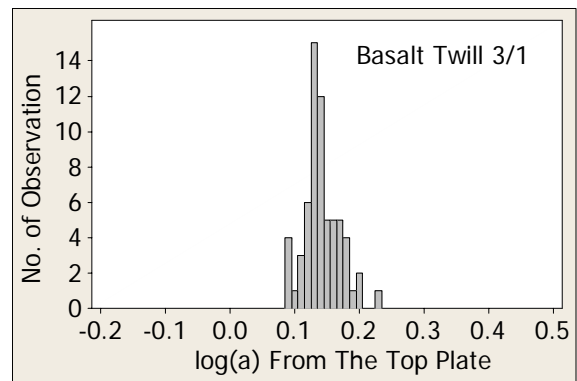
(c) Distribution of K_{xx} from the Top Sensor Plate



(d) Distribution of K_{yy} from the Top Sensor Plate



(e) Distribution of $\text{Log}(a)$ from the Bottom Sensor Plate



(f) Distribution of $\text{Log}(a)$ from the Top Sensor Plate

Figure 3.11 Distribution of Permeability, 'a' is the Permeability Anisotropic Ratio

Table 3.3 Experimental Results from Both Plates

	Bottom				Top			
ID	log α	Theta	Kxx	Kyy	log α	Theta	Kxx	Kyy
0405-1	0.096884	0.2929			0.094419	3.534825		
0405-2	0.155295	-4.64367			0.184949	-3.46451		
0405-3	0.118772	-10.7997			0.12824	-13.9062		
0413-1	0.12339	-7.60775	1327.71	999.3391	0.130963	0.458852	1333.058	986.0208
0413-2	0.082298	4.778073	1464.382	1211.592	0.12432	-12.8065	1529.482	1148.748
0413-3	0.134586	-13.1252	1131.291	829.8284	0.136112	-15.3828	1128.189	824.6497
0413-4	0.118422	-6.3469	1438.07	1094.858	0.143615	2.653053	1479.664	1063.037
0413-5	0.085425	3.529526			0.090684	-2.62158		
0415-1	0.147156	9.128619	988.46	704.3735	0.128191	7.034799	963.0309	716.885
0415-2	0.143744	-9.28756	1210.698	869.544	0.130483	-7.13512	1196.146	885.7302
0415-3	0.115867	-16.0956	1087.025	832.4784	0.126767	-8.08547	1095.077	817.8572
0425-3	0.12533	-9.92542	1166.669	874.2131	0.144511	-6.40781	1187.123	851.1083
0425-4	0.149627	-8.61709	946.8445	670.8907	0.136656	-7.93446	932.1263	680.4857
0425-5	0.156897	-3.9895	970.4042	676.1695	0.157225	-9.12721	965.2786	672.0912
0425-6	0.162523	-5.77286	909.8429	625.8108	0.173183	-5.5768	919.5475	617.1509
0505-2	0.141866	4.19954	794.0194	572.7496	0.147382	3.150276	793.8746	565.4182
0505-4	0.156375	-6.08167	1147.404	800.4631	0.153408	-5.85912	1139.017	800.0583
0505-5	0.135911	4.357775			0.130618	3.892419		
0510-1	0.169134	-1.37515			0.196449	-8.81238		
0510-2	0.188523	-2.34084	1103.739	715.0611	0.228292	-5.93528	1144.623	676.6592
0510-3	0.156072	-4.65644			0.161365	-5.74544		
0510-5	0.097557	-10.9875	840.7552	671.6026	0.117252	-18.5966	856.3115	653.7021
0510-6	0.099127	-7.42883			0.102821	-8.84625		
0510-7	0.104302	-4.57701	651.0305	512.0349	0.129272	-8.08746	667.8574	495.9196
0510-8	0.11747	-12.7466	786.8963	600.4088	0.132987	-11.5266	800.8383	589.6001
0515-1	0.103383	-8.45864			0.126876	-10.8707		
0515-2	0.152292	0.533493			0.133806	-3.49147		
0515-3	0.161858	-6.10946			0.184855	-8.14595		
0515-4	0.143553	2.164104	608.0418	436.8988	0.128362	-4.44055	592.9894	441.2498
0515-5	0.104893	-7.68522	1045.127	820.8742	0.132563	-13.9625	1080.51	796.2809
0524-1	0.111119	-3.53377	965.5759	747.5966	0.136437	-6.22945	981.6216	716.9808
0524-2	0.125217	-2.40683	876.9897	657.3208	0.145748	-5.17275	890.0151	636.2816
0524-3	0.138448	-10.2389	863.3397	627.6738	0.140705	-13.7643	858.8403	621.1655
0524-4	0.157735	-1.89087	845.9137	588.2893	0.124039	-7.80246	809.2447	608.1916
0527-1	0.092032	-18.5545	749.8615	606.6646	0.110951	-17.7215	763.0673	591.033
0527-2	0.163418	-1.01776	907.2625	622.7521	0.174676	-5.09244	911.6676	609.7626
0527-3	0.161282	1.364053	956.7595	659.9654	0.150417	-0.40696	929.0343	657.0742
0527-4	0.132615	0.002001	958.1004	705.9861	0.142005	-3.61445	961.1701	693.0993
0527-5	0.124071	3.452776	762.0299	572.6661	0.126605	-1.85193	757.608	566.0298
0527-7	0.082586	-7.18659	608.7373	503.32	0.088367	-14.6389	610.3306	497.9648
0602-1	0.19178	4.400352	826.8025	531.6454	0.174371	1.004715	804.9239	538.7454
0602-2	0.132474	0.949793	922.4366	679.9266	0.137678	-1.34246	919.2681	669.5213

0602-3	0.150146	-2.04782	920.634	651.5397	0.122258	-3.70563	880.4144	664.3997
0602-4	0.177295	3.151192	830.3892	552.0601	0.179017	-1.30154	823.753	545.4809
0602-5	0.152641	-3.89749	821.4869	578.0425	0.154554	-6.1433	818.0934	573.1246
0602-6	0.159989	3.419829	737.779	510.4315	0.155793	-0.83498	728.8182	509.1267
0602-7	0.172373	3.038696	618.9771	416.1994	0.159513	2.599716	607.1098	420.4885
0602-8	0.146938	-3.41204	562.8731	401.3027	0.141268	-8.84545	559.5409	404.1694
0602-9	0.10533	-3.70237	568.492	446.0606	0.11083	-7.69841	567.1411	439.4011
0804-2	0.097433	-13.0929			0.120444	-22.0135		
0804-3	0.130552	-8.07827	682.1636	505.0522	0.142366	-14.9565	690.7132	497.6586
0804-4	0.10719	-9.85397	690.1814	539.2291	0.125748	-14.7002	703.5549	526.6836
0804-5	0.094332	-5.15549	643.3769	517.7664	0.11767	-9.58761	658.4257	502.1536
0804-6	0.12335	-5.40437	614.2626	462.3854	0.110447	-8.99647	602.3723	467.109
0806-1	0.197314	-2.18888	494.5834	313.9967	0.188062	-1.71618	484.2067	314.0282
0806-2	0.147229	-3.20385	663.1552	472.4827	0.141823	-6.96007	653.8379	471.6792
0806-3	0.194454	-0.33747	703.1658	449.3692	0.198139	-4.20772	702.7259	445.2941
0806-4	0.199817	11.50932	703.1469	443.8425	0.167293	7.425814	672.663	457.6198
0806-5	0.137705	-2.281	715.0206	520.7316	0.135805	-6.69624	709.3933	518.8983
0806-6	0.112573	-0.50719	725.5196	559.856	0.132532	-4.48361	736.9124	543.1054
0806-7	0.18173	1.212631	730.8484	480.9474	0.176093	-2.28846	720.4829	480.3201
0806-8	0.165523	3.801168	793.3537	541.931	0.171597	0.426039	791.74	533.3167
0806-9	0.10093	-10.7489	701.3705	555.9261	0.090406	-20.2769	686.8201	557.7466
0806-10	0.142373	-0.0207	825.3663	594.6674	0.16387	-8.33454	838.1319	574.701

Table 3.3 (Continued) Experimental Results from Both Plates

Shown in Table 3.2, the results derived from the information which came from the bottom and top sensor plates corresponded with each other quite well. This was proved by our visual observation after each experiment, and demonstrated that the communication between the fluid flow along the top fabric layer and that along the bottom layer is good. Since the in-plane assumption is well satisfied, the permeability through the thickness is perpendicular to the material plane [125].

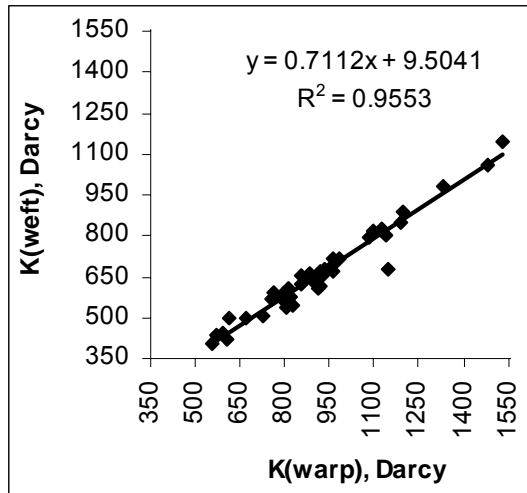
Figure 3.11 shows that the distributions of the permeability magnitude do not look like normal distributions, and probably the Weibull distribution describes them much better. This was proved by the Anderson-Darling tests for K_{xx} from the bottom sensor plate [203]. The AD and p-values for the normal test are 0.976 and 0.013 respectively, 1.285 and (<0.01) respectively for 2-parameter Weibull distribution, 0.267 and (>0.5) respectively for 3-parameter Weibull distribution. From the comparison between the AD and P-values (the smaller the AD numbers or the higher the P-values, the better the fit for the distribution), the

3-parameter Weibull distribution describes the distribution much better than the normal and 2-parameter Weibull distribution, and the 3-parameter Weibull distribution for K_{xx} from the bottom sensor plate was calculated to $P(K_{xx}) = 1 - \exp[-(\frac{K_{xx} - 466.72}{440.85})^{1.81}]$.

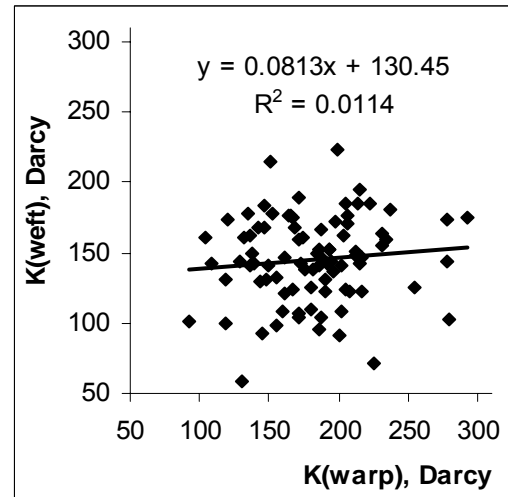
At 35.75% fiber volume fraction, the alignment of the principle axis for the basalt fabric, K_{xx} is quite close to the warp direction, from the small magnitude of angle θ and its small standard deviation in Table 3.2. This result is very similar to that of the CNF crowfoot fabric acquired from in-plane flow measurement also, which had an angle of -4.0° according to our designation [144]. Interestingly, the CNF crowfoot is also a twill 3/1 weave. In addition, according to the relationship for the CNF crowfoot between the effective permeability acquired from Unidirectional saturated measurements and the fiber volume fraction, the effective permeability of it at 35.75% fiber volume fraction (the one for our basalt fabric) and was estimated to be 700 Darcy [8], similar but a little smaller than the effective permeability of the basalt fabric, which was acquired from in-plane measurements. Besides, the permeability from UD saturated measurements should be a little smaller than from in-plane unsaturated measurement, due to the capillary effect [13]. Therefore, we speculate that fabrics with similar structures may show similar permeability.

The permeability anisotropic ratio is close to 1, which also corresponded well with our visual observation of the anisotropic ratio of the elliptical flow front, which indicates that at such fiber volume fraction, the materials behaves close to an isotropic media. The small and quite stable anisotropic ratio indicates a high correlation between K_{xx} and K_{yy} . This is demonstrated by the large correlation coefficient R^2 value in Figure 3.12 (a). Because the permeability principle axis is very close to the warp direction, K_{warp} is used to represent K_{xx} and K_{weft} to represent K_{yy} . In Figure 3.12, similar graphs for R420 and RE 144/255 glass fabrics are also presented. From Figure 3.12, glass fabric RE 144/255 has a little but much smaller correlation between K_{warp} and K_{weft} , compared to the basalt fabric. And glass R420 has negligible correlation. A test to determine the significance of the correlation coefficient r between K_{warp} and K_{weft} for basalt fabric is performed. The null hypothesis is: $r = 0$, and the alternative hypothesis is: $r \neq 0$. The test statistic for the correlation coefficient was computed according to reference (39) to obtain a P value < 0.001 . The P value is the weight of evidence

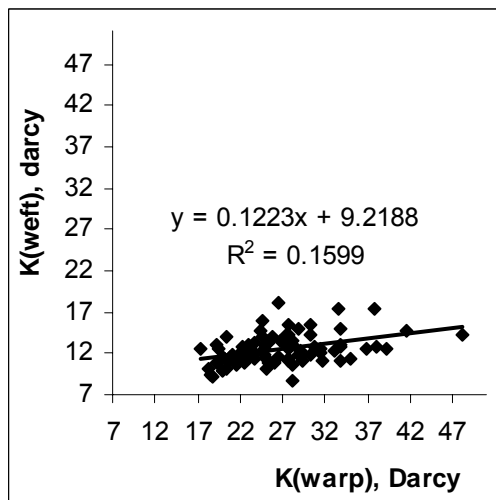
supporting the null hypothesis. $P < 0.001$ is quite small so the null hypothesis is rejected at a confidence level of 99.9%. Therefore, the correlation between K_{warp} and K_{weft} is significant for basalt fabric. When the same statistical tests are performed for R420 and RE144/255, the P values are 0.327 and smaller than 0.001, correspondingly. Therefore, the correlation between K_{warp} and K_{weft} is not significant for R 420 but is significant for RE 144/255.



(a) Basalt Fabric at 35.75% Fiber Volume Fraction



(b) R420 at 41.7% Fiber Volume Fraction



(c) RE 144/255 at 52.8% Fiber Volume Fraction

Figure 3.12 Correlations between Permeability in Warp and Weft Direction for Different Fabrics

Such huge difference in the correlation coefficients between these different fabrics may be caused by the difference in the fabric structures. From Hoes' work [13], it is known that

permeability broad distribution results from the nesting of yarns in the neighboring layers. For all the fabrics discussed above, nesting probably causes the broad distribution of the components of the permeability tensor. However, nesting appears to have different effects on the distribution of the permeability anisotropy, depending upon the fabric structure. Plain weave R420 has the broadest distribution of anisotropy and basalt twill fabric the narrowest.

The high correlation between K_{warp} and K_{weft} for basalt fabric is desirable for RTM processing because a consistent flow pattern will be obtained. In the cases where a broad distribution of anisotropy is obtained and there is therefore little correlation between K_{warp} and K_{weft} , variable flow patterns may occur for different injections, rendering control and part-to-part consistency difficult to achieve.

II. Characterization of Micro Flow behavior

To characterize the micro flow, measurements on DCS surface tension and contact angle between fiber surface and DCS fluid were performed. The equipment is DCA 322 [204]. The surface tension was measured using a Wilhelmy plate, made of glass. The Wilhelmy plate is a standard solid probe which gives 0 contact angle in the liquid because of its high surface energy. The Wilhelmy plate was hung from a fine balance and dipped into the liquid at a speed of 80 micron/sec. At the moment its lower edge touched the liquid, the weight change was measured using the fine balance. Wilhelmy equation was used to calculate the surface tension, $\gamma = F \times g / PR$, where γ is the surface tension of the fluid, F is the weight change when the Wilhelmy plate touches the liquid, g is the gravity acceleration term, and PR is the circumference of the Wilhelmy plate. Figure 3.13 shows the curve, weight change measured by the fine balance versus position, which is the distance the Wilhelmy goes down. When the plate goes down, it is called ‘advancing’. As can be seen, when the Wilhelmy plate advanced a little less than 5 mm, the weight suddenly changed. This means that the Wilhelmy plate just touched the liquid. The plate continued to advance as programmed, and then pulled out of the liquid (called ‘receding’). Theoretically the advancing curve and receding curve should overlap, but they often didn’t, because the Wilhelmy plate was not completely clean, there was static electricity effect, the Wilhelmy plate was not straight when it entered the liquid. In such cases, the weight measured in the receding curve is used to calculate the surface tension. Such experiment was replicated for 6 times for the DCS (corn

syrup/water = 11/3, weight ratio). And the surface tension measured was $(79.02 \pm 1.91) \times 10^{-3} \text{ Pa}\cdot\text{m}$ (mean \pm standard deviation). The result was a little higher than that measured by Hoes [13], $(68.1 \pm 0.4) \times 10^{-3} \text{ Pa}\cdot\text{m}$, who had a DCS solution with different weight ratio of corn syrup. In addition, the deviation of the surface was very small compared to the mean, which demonstrated that the wettability of the DCS was quite stable. Since the viscosity measurements demonstrated DCS satisfied Newtonian behavior over a wide range of shear rate ($0.1 \sim 100 \text{ s}^{-1}$), there only remains the question concerning the significance of capillary flow or the sink effect.

As discussed before, the capillary flow is a complex function of porosity, injection pressure or fluid flow velocity, fluid surface tension, and contact angle between the fiber and fluid.

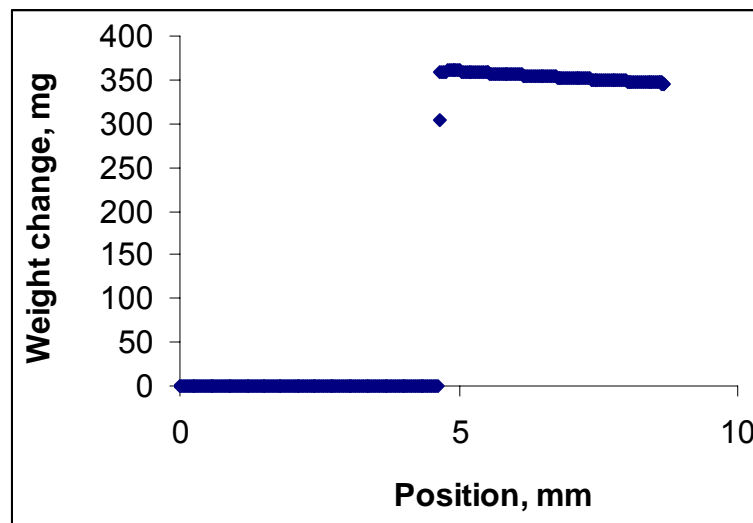


Figure 3.13 Measurement of Surface Tension

The measurement of contact angle between fiber and DCS was similar, but it was difficult to prepare the single fiber sample because they were only about 9 micron thick. A single filament from a yarn was carefully selected, fixed one end to a metal rod by glue with the other end sticking out of the rod, and cut the rest of the fiber so that the hanging part had a length about 3~5 mm. Such short length helped the hanging part of the fiber to stay rigid like a rod. Similar procedures as those in the measurement of surface tension were used, except that a single fiber was used, not the Wilhelmy plate. The weight change in the advancing and receding curves was measured to obtain the advancing contact angle and receding contact

angle. Such measurement was replicated for 10 times and the results for the contact angles between DCS and basalt and glass fibers (mean \pm standard deviation) are listed in Table 3.4 below. There is no significant difference between basalt and glass, concerning the contact angles between them and DCS. In addition, there was a large difference between advancing and receding contact angles. This was due to the stickiness of the DCS: after a first immersion, the DCS remained on the fiber surface as a film. When receding the fiber, what was actually measured was the contact angle between DCS and its film, which was completely different from the interaction between DCS and the dry fiber surface. This explanation was confirmed by [138].

Table 3.4 Contact Angles between Fiber and DCS

Fiber type	θ , advancing, degree	θ , receding, degree
Basalt	70.2 ± 5.4	1.5 ± 3.2
Glass	65.4 ± 8.3	0

In the radial flow measurements for permeability, the flow rate, Q used was approximately 0.3 liter per minute, or 5×10^{-6} m³/s. The thickness of the preform, h was about 4.7 mm, or 4.7×10^{-3} m. The radius of flow front, r was from 0.05 m to 0.136 m, considering that data was ignored for the first 5 seconds. The porosity of the preform, ϕ was about 0.64. The relationship between the flow rate Q and fluid interstitial velocity v is

$$2\pi r h \phi v = Q \quad (3-31)$$

Equation (3-31) can be written as
$$v = \frac{Q}{2\pi r h \phi} \quad (3-32)$$

Therefore, from equation (3-31), the fluid interstitial velocity was calculated to be from 1.95×10^{-3} m/s to 5.29×10^{-3} m/s. The density of the DCS, ρ was measured to be approximately 1.2 g/cm³, or 1.2×10^3 kg/m³. The characteristic pore size, D was estimated as the square root of the geometric mean of the permeability value, $D = \sqrt{K_{rr}} = \sqrt[4]{K_{xx} K_{yy}}$, to be 2.68×10^{-5} m. The viscosity of DCS was taken as 0.1 Pa • s. Then the Reynolds number, Re was calculated as [131]

$$\text{Re} = \frac{\rho D v}{\mu} = 6.26 \times 10^{-4} \sim 1.70 \times 10^{-3} \quad (3-33)$$

Such range is much smaller than 1, so the flow behavior was typically within the laminar flow [131], and this satisfied the assumption of Darcy's law quite well.

According to surface tension and contact angle measured, the capillary number, Ca was calculated according to equation (1-22), $Ca = \frac{v\mu}{\gamma \cos\theta}$, to be $7.27 \times 10^{-3} \sim 1.98 \times 10^{-2}$. As discussed before, when Ca is smaller than 0.003 for flow parallel to the UD preform, 0.005 transverse to the UD preform, or 0.001 for bi-directional preforms, the flow is dominated by capillary effect, or micro-flow inside the yarn. When Ca gets larger and larger, the flow is more and more dominated by viscous effect [159, 162, 163]. The capillary number in our experiment was much larger than 0.001, so the capillary effect can be deemed negligible. The way of judging the effect of the capillary flow from the magnitude of capillary number doesn't account for the fiber volume fraction. Usually the higher the fiber volume fraction, the lower the porosity, the more important the capillary flow is. Fortunately the fiber volume fraction used was only about 0.36, which was very small. Therefore, significant effects on the measured permeability from the capillary effects are not expected.

From the derivation in the previous paragraph, the Ca approximately ranged from $7.27 \times 10^{-3} \sim 1.98 \times 10^{-2}$. According to references, $7.27 \times 10^{-3} \sim 1.98 \times 10^{-2}$ is very close to the transition region (Ca = 0.001) from capillary dominated flow to viscous dominated flow, and still falls into the latter category. Although some reference [159] demonstrated sink effect increases as Ca increases, it didn't give quantitative results as how to calculate the sink effect on the permeability measurement results. At this moment, the magnitude of the sink effect is not known.

Part IV. Comparison of Permeability Measurement Results between UD Wetting Measurements and Radial Measurements

For comparison purposes, UD wetting permeability measurements were performed at the University of Montreal, Department of Mechanical Engineering, under the help of Philippe Causse, Prof. Edu Ruiz and Francois Trochu, using the same basalt fabric.

The mold width is 11 cm, and length is 94 cm. The schematic drawing is shown in Figure 3.14. The materials were cut to be 11cm×41cm. The mold cavity thickness was 4.617 mm, which resulted in a similar but a little larger nominal fiber volume fraction, 36.10%. But when the weight of the materials was measured, the claimed areal density has a little deviation from the real one. After correction, the fiber volume fraction, V_f , was recorded for each test.

When materials were cut, the edges were taped to avoid any yarn dropping from the edge. There is a rubber band along the inside edge of the mold, and width of the material was just fit into the space inside the rubber band. Silicon seals were placed along the edges of the rubber band, to reduce the edge effect (race-tracking problem) to the minimum. Then, the materials were placed inside the rubber band. The mold is covered with plexiglas (about 20 mm thick) and a metal frame is placed on the plexiglas plate. The metal frame was fixed over the plastic glass using small screws around the edges.

Constant flow injection was used in the experiment. A line injection was performed along one edge of the preform. During injection, the flow front was observed through the glass cover and the following data were recorded at various times: sample time t_i , front position x_i and injection pressure $P(t_i)$, corresponding with the time the fluid front reaches the i th line perpendicular to the flow direction. There are altogether 21 lines, and the time when the fluid front reaches the 1st line was defined as time=0. The space between the neighboring lines is 20 mm. When the fluid front reaches the last line, the experiment was halted. The material injection edge coincides with the 1st line. The diagram is shown in Figure 3.14 below. Choose the injection pressure by closing the control valve of the injection pump. The real injection pressure was measured through a pressure transducer just at the injected edge of the

perform. The injection pressure should be such that the fluid fills the mold (40 cm long flowing distance) around 5 minutes. The choice of the parameters (injection pressure, injection time, and material length.) takes into account the uncertainty on the position of the flow front [143], which is usually very fuzzy in the experiment.

During the experiment, video recordings were obtained from above the glass cover. If problems like race-tracking were observed, the experiment was stopped and declared invalid. After the injection was done, the software ‘PolyPer’ [205] was used to calculate the effective permeability. The principle how to calculate the UD permeability from constant injection pressure experiment was described in the previous chapter (equation (1-17) and (1-18)). Experiments were performed in warp, weft and 45 ° directions, so effective permeability values in these three directions were obtained. The ‘PolyPer’ software was then used to calculate the permeability principal values, angle θ as defined in Figure 3.10, and the anisotropic ratio of permeability. The detailed procedures how to derive these parameters from the three effective permeability values are described by Parnas [125].

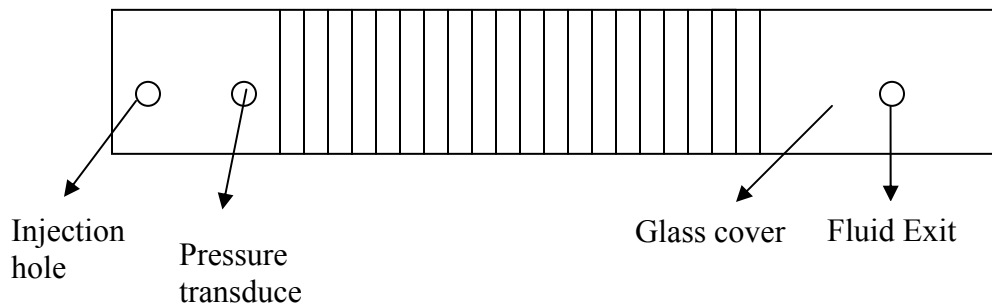


Figure 3.14 The Diagram of the UD Experimental Set Up

At each test, the material was weighed to calculate the real fiber volume fraction. The averaged fiber volume fraction for all the tests was 37.99%, and the nominal fiber volume fraction was 36.10% according to the information of the manufacturer. After the UD permeability was obtained at several fiber volume fractions, V_f , the $\ln(\text{permeability})$ was plotted versus $\ln(V_f)$, then extrapolate V_f to 37.99% and get the corresponding permeability, the procedure is shown in Figure 3.15 below and the results are listed in Table 3.5 below. In Figure 3.15, a linear relationship between $\ln(\text{permeability})$ and $\ln(V_f)$ is observed. From the tests, permeability values at point A are measured, and extrapolated to the permeability at point B according to the linear relationship. The method is discussed and confirmed by Hoes

[13]. The UD permeability values in warp, weft and 45° directions are shown in Figure 3.16 below. There were 7 UD measurements in the warp direction, 3 in the weft direction and 5 in the 45° direction. Averaging the values on the same directions, and using the averaged results with the help of ‘PolyPer’ software, the permeability principal values, angle θ , and anisotropic ratio were calculated. The comparison of the results from radial tests and UD tests are shown in Table 3.6 below.

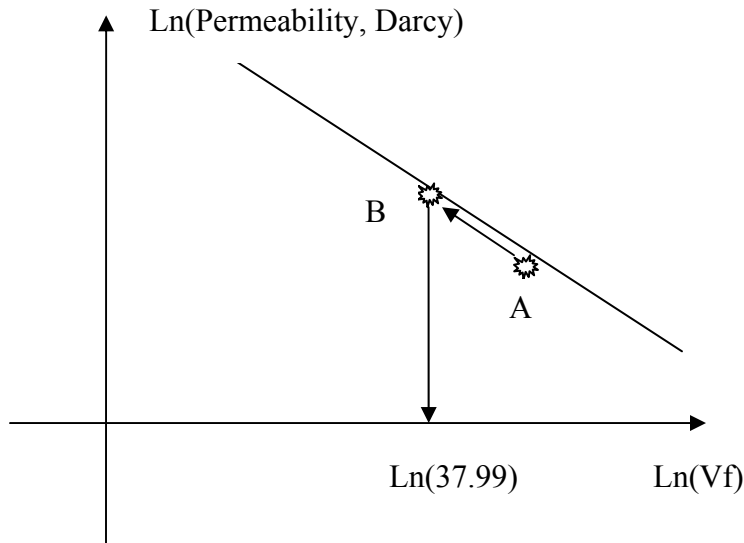


Figure 3.15 Scheme of Getting the Extrapolated Permeability

Table 3.5 UD Permeability Measurement Results

Experiment ID	Direction	V_f , %	Permeability, K, Darcy	Extrapolated K at $V_f = 36.10\%$
0826-1	Warp	37.95	871.09	865.51
0829-1	Warp	37.37	845.96	765.09
0829-3	Warp	37.56	851.94	794.73
0901-1	Warp	37.90	814.05	802.34
0902-2	Warp	34.94	1353.70	812.03
0902-3	Warp	36.04	1183.48	857.85
0902-4	Warp	35.83	1122.68	785.26
0829-4	Weft	37.32	607.95	582.72
0830-1	Weft	38.56	564.28	584.80
0830-2	Weft	38.68	556.58	581.14
0830-3	45°	36.71	765.11	658.48
0831-1	45°	36.89	835.32	734.48
0831-2	45°	39.11	619.40	703.24
0831-3	45°	39.71	561.95	682.19
0831-4	45°	40.07	552.83	698.17

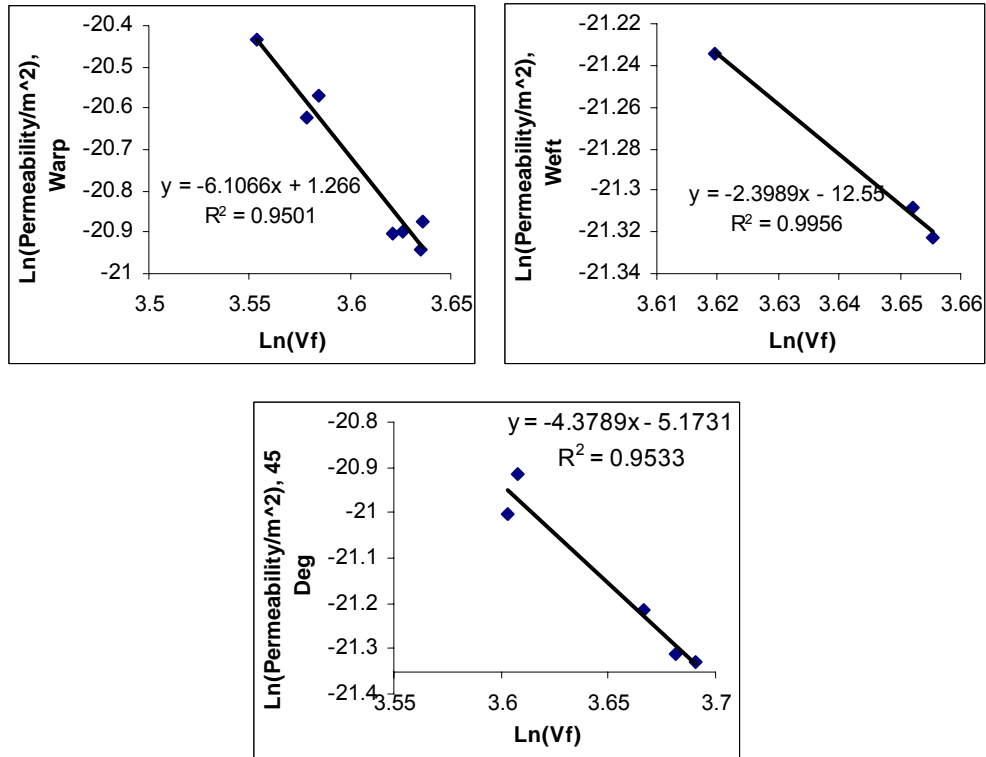


Figure 3.16 Data from UD Experiments

Table 3.6 Comparison of Permeability Results from UD and Radial Tests

	Radial Flow	UD flow	Relative Difference
Fiber volume fraction, %	N/A	37.99	
Nominal fiber volume fraction, %	35.75	36.10	0.01
Anisotropic ratio	1.374 ± 0.097 (bottom) 1.390 ± 0.091 (top)	1.396	0.0058
Principle axis angle, deg	-3.47 ± 6.00 (bottom) -6.34 ± 6.35 (top)	-4.06	0.17
K _{xx} , darcy	857.85 ± 218.88 (bottom) 858.43 ± 227.46 (top)	812.83	0.053
K _{yy} , darcy	625.71 ± 174.19 (bottom) 617.98 ± 166.71 (top)	582.42	0.061

Table 3.6 shows that the results from the two kinds of measurements correspond well with each other. The differences between the means stay well within the experimental scatter. The comparison between the distributions of permeability values in the warp direction (K_{xx}) obtained from UD and radial tests is shown in Figure 3.17 below. The comparison showed that the scatter from UD tests was much smaller than that measured from radial tests. The most important reason may be that only 7 measurements are not enough to construct the distribution. Besides, the surface density variation of the materials in the UD tests were considered, but not accounted for in the radial tests. But Hoes' results showed that such consideration did little help to reduce the experimental scatter [13].

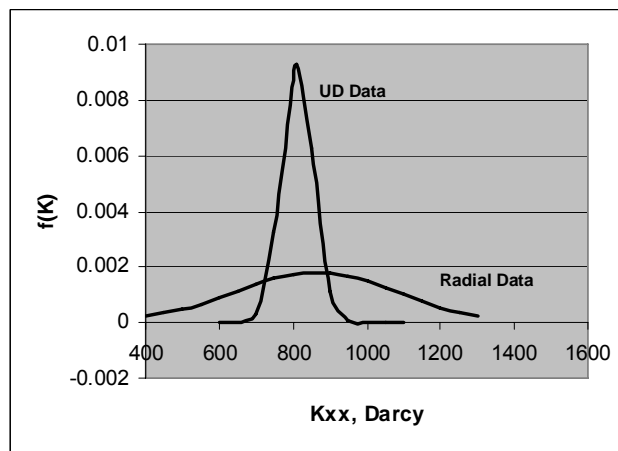


Figure 3.17 Comparison of K_{xx} Distribution between UD and Radial Flow Tests

Chapter IV. Recommendations & Suggestions for Future Work

Part I. Summary

The most interesting result of this study was from the tension-tension fatigue tests. Basalt epoxy composites had a significantly longer fatigue life than their closest glass epoxy composite counterparts. It was also found that basalt epoxy composites made from hand lay-up have a longer fatigue life than the same materials made from RTM. Thus, the manufacturing method may play a significant role in determining the performance of the material.

Perhaps the most significant result of this study is that after extensive statistical analysis of the mechanical measurements, it was found that the strength and stiffness of the basalt epoxy reinforced composites were no greater than the glass epoxy reinforced material. This was unexpected since the properties of basalt fiber have been reported much higher than for glass. Upon careful measurement of the single fiber properties of the basalt and glass used in this study, no statistical difference was found. The glass fiber properties were very close to those expected from the literature, while the basalt fiber properties were much lower than the literature values.

In the comparison of the environmental aging behavior, it was found that the interfacial zones of basalt fiber reinforced composites were more sensitive to the aging conditions than those in the glass fiber reinforced composites. In contrast to the fatigue results noted above, the apparent sensitivity of the basalt epoxy interface is a cause for serious concern.

The interfacial region of basalt vinyl ester composite looked different than that in the other composites. Lower than expected mechanical performance in the basalt vinyl ester composite was attributed to a poor interface, and this indicates that the basalt fiber is probably not compatible with vinyl ester polymers without the application of a sizing finish to mediate the chemical interactions.

When the composite materials were produced, the reinforcements were heat treated to remove the sizing finishes on the fiber surfaces, and such heat treatment may have modified the chemical structure of the fiber surfaces [226-230]. Xiao, et. al., found that heating the glass fiber can improve the wetting ability and interfacial adhesion between the fiber and PET matrix, and the interfacial shear strength of long glass fiber reinforced PET increased with the heating time [228]. Zhang, et. al., found similar results with carbon nano-tube reinforced polymer composites [229]. Wu [227] and Liu [226] found that heating the fiber reinforcements helps to lower the fiber surface free energy, remove fiber surface contaminants, and improve the interfacial shear strength. However, the temperatures they used (80~200 °C) were much lower than used in this work (300~500 °C). Under such low temperature (80~200 °C), it was unlikely that the fiber weakened. In this study, the glass fibers were almost certainly weakened by the high heat treatment temperatures, and careful statistical data analysis was required to compensate for these effects.

Part II. Future Work on Basalt for the Civil Engineering Community

The wide disagreement between the literature properties of the basalt fibers and the properties measured in this work renders any further consideration of basalt reinforced composites highly problematical. While the measurements conducted in this investigation

contain some uncertainty, many repetitions were conducted, and the controls using glass fibers agreed well with literature. Therefore, the uncertainties reported in the data are likely caused by random errors expected in any such measurements.

The only further work recommended to the Civil Engineering community with basalt is a careful verification of the properties advertised by manufacturers. This activity is worthwhile since the fatigue life results are highly encouraging and significant. If reliable sources of basalt fiber were identified, and then the fatigue life measurements verified, an important new reinforcement may become available. Current commercial materials reinforced with basalt, however, should be treated with great care.

Many other research activities with basalt can be envisioned if the properties of the fiber can be validated, and these longer range activities center on the interfacial interactions of basalt with polymers. Such interactions are extremely important for maximizing the performance and durability of polymer composites, and should be performed by the composite materials community.

Appendix. Composite Material Overview

Part I. Fiber Reinforced Composite Materials Generalities

I. Introduction to Composite Materials

A composite is a material that contains two or more distinct constituents or phases, and the amount of the minor phase must be greater than a reasonable proportion (~5%) so that the composite properties are much different from those of the constituents [1]. The continuous and often major phase is termed matrix, which can be ceramic, metallic or polymeric. The second phase is referred to as the reinforcement, either fibrous or particulate.

Composites are produced to optimize material properties, including mechanical, chemical and physical properties, such as thermal, electrical, optical and acoustical properties [2]. Composites have been used by people for thousands of years but the major developments have taken place recently due to their high specific properties (properties such as Young's modulus, GPa per unit mass) and easily tolerable properties compared to single component materials. Some of typical applications of polymer matrix composites are listed in Table A.1 [1] below.

Composite materials can be divided into particle reinforced or fiber reinforced composites, and the later can be further divided into short fiber (whisker) and continuous fiber (fabric) reinforced composites. Continuous fibers are usually weaved into fabrics for purpose of easy handleability. Fabric is a manufactured assembly of fibers and/or yarns that has substantial surface area in relation to its thickness and sufficient inherent cohesion to give the assembly mechanical strength. Fabrics are commonly woven or knitted, but the term includes assemblies produced by braiding, felting, lace-making, net-making, nonwoven processes and tufting [3]. Composites can also be divided into synthetic and natural composites. An old example of synthetic composites is bricks made from mud reinforced by straw used in ancient civilization. Another example of synthetic composites used now is concrete, a mixture of stones held together by cement. The best example of natural composites is bone,

composed of organic fibers (collagen), small inorganic crystals, water and fats, or wood, made of long and spirally wound cellulose fiber bonded together by lignin.

Figure A.1 below represents a common classification of composite materials [1] according to reinforcement forms. Textile composites are those reinforced by fabric reinforcement. **This report focuses on the processing and mechanical properties of woven fabric (reinforced) polymer composites.** Woven fabrics consist of at least two threads woven together perpendicularly: the warp and the weft. According to crimp and drapeability, woven fabrics can be classified into plain, basket, twill and satin weave [3]. A woven fabric is characterized by the following parameters: warp and weft yarns fibrous nature and yarn size, weave pattern, number of warp yarns per unit of the fabric width (ends count), number of weft yarns per unit of the fabric length (picks count), and fabric areal density.

Table A.1 Current Large Scale Applications of Polymer Composites

Industrial Sector	
Aerospace	wings, fuselage, radomes, antennae, tail-planes, helicopter blades, landing gears, seats, floors, interior panels, fuel tanks, rocket motor cases, nose cone, launch tubes.
Automobile	Body panel, cabs, spoilers, consoles, instrument panels, lamp-housings, bumpers, leaf springs, drive shafts, gears, bearings.
Boats	Hulls, decks, masts, engine shrouds, interior panels.
Chemical	Pipes, tanks, pressure vessels, hoppers, valves, pumps, impellers.
Domestic	Interior and exterior panels, chairs, tables, baths, shower units, ladders
Electrical	Panels, housings, switchgears, insulator, connectors.
Leisure	Motor homes, caravans, trailers, golf clubs, racquets, protective helmets, skits, archery bows, surfboards, fishing rods, canoes, pools, diving boards, playground equipment.

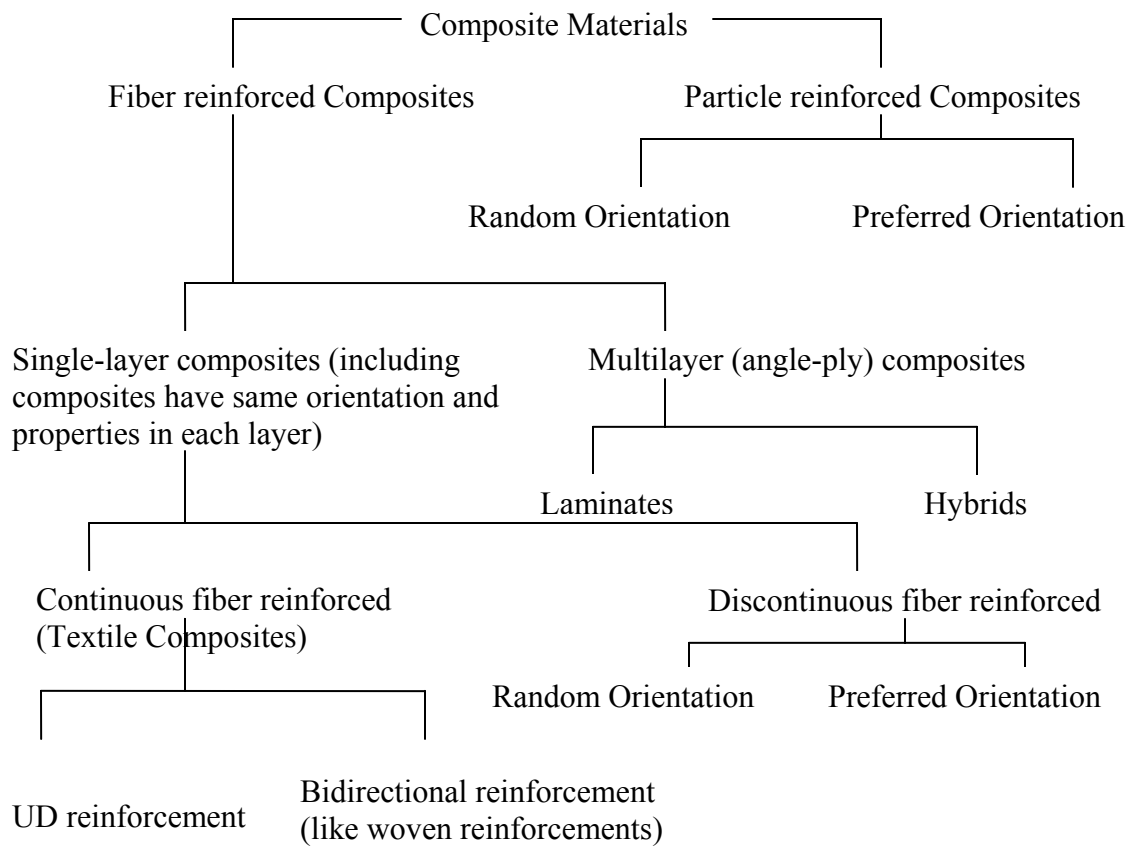
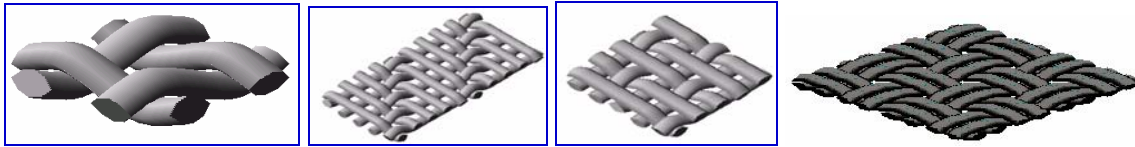


Figure A.1 Classification of Composite Materials

The size of yarn is a very important parameter in textile composites [4]. Yarn size is characterized by filament count, the number of fibers, and by linear density, either denier (the weight in grams of 9 km single yarn) or tex (the weight in grams of 1 km single yarn) or yield (length per unit mass). Yarns are often twisted to facilitate the weaving process, which reduces the axial stiffness and strength. Larger yarns favor crack deflection and increase the pull-out lengths of broken tows that continue to carry load across the fracture plane, increasing the work of fracture [4].

According to the weave pattern, 2D woven fabrics are divided into plain weave, twill weave, satin weave and basket weave. Their figures are shown in Figure A.2 below. Plain weave is the simplest weave pattern in woven fabrics, characterized by over-one-under-one pattern. It has regular surface, excellent stability but low drapability. Twill is a weave that produces

diagonal lines on the fabric surface. Twill has medium stability and drapability. Compared to twill, satin weave has the binding places arranged with a view to produce a smooth fabric surface, and satin has low stability but good drapability.



(a) Plain Weave (b) Twill Weave (c) Satin Weave (d) Basket Weave

Figure A.2 Commonly used 2D Weave Patterns

When a fabric contains same number of equal weight warp and weft yarns per unit length, the fabric is balanced, and unbalanced if not. When the density of yarns in one direction is much larger than that in the other direction, i.e. the ratio of the density in the two directions is 80/20, the fabric is unidirectional fabric [5].

II. Basic Components in Fiber Reinforced Composite Materials

1. Matrix Materials

As discussed above, matrix is the phase that holds the reinforcement phase together and transfers the load in composites. It transfers the applied load to the fibers, thereby keeping the fiber in their position and orientation. Matrix also resists all kinds of environmental corrosion and determines the maximum service temperature of the composites.

Polymer Matrix

According to the extent of crosslinking during processing, polymer matrix can be classified as thermosets (thermoset polymers) and thermoplastics (thermoplastic polymers). Thermosets, particularly epoxies and polyesters are the most widely used matrix materials. They are highly crosslinked polymers made from small molecular weight resins and catalysts. Thermoset polymers are widely used in composites because of their excellent stability under high temperature and physical stress. Rigid network structures due to highly crosslinking also give them dimensional stability under a wide variety of conditions [6].

When heated, they don't flow but just decompose. So the big disadvantage of thermosets is that reshaping is not possible afterwards. The two most important processing parameters for thermosets are initial viscosity and pot-life. Initial viscosity determines the ease with which the resin can be incorporated into the reinforcement. Pot-life determines the time needed for curing before demoulding. Besides epoxies and polyester resins, thermosets also include [2] vinyl ester, bismaleimide, polyimide, and phenolics.

Thermoplastics are uncrosslinked polymers. They soften and flow when heated. Before processing, thermoplastics are usually heated until they flow, then are introduced and shaped in a mold and cooled down to solidify the polymer. This process is completely reversible since no chemical reaction happens. The main processing parameters for thermoplastics are melting temperature and melt viscosity [6]. Thermoplastic polymers include polypropylene (PP), polyamide (PA), poly (p-phenylene sulfide) (PPS), polyetheretherketone (PEEK), polyetherimide (PEI), and polyamideimide (PAI).

Other Matrix Materials

In some special cases other matrix materials are used to obtain special properties, like high temperature resistance, high flammability resistance, high radiation resistance, and high electrical conductivity. Other matrix materials include metals, ceramics, and carbon.

2. Fibrous Reinforcements

They can be differentiated by origin: artificial fibers and natural fibers.

Artificial Fibers

Glass fiber: Glass fibers are made from the traditional materials to produce glass, mainly silica, lime, aluminum oxide and magnesium oxide. Glass fiber is formed when thin strands of raw materials are extruded into fibers with small diameters at temperature about 1550 °C. The most commonly used glass fibers are E-glass fiber, electrical glass fiber, and S-glass fiber, high strength glass fiber. Fiber diameters often range from 3.5 to 13 micron, and designated as B (3.5 micron), C (4.5 micron), D (5 micron), DE (6 micron), E (7 micron), G (9 micron), H (10 micron), K (13 micron) fibers [7]. Glass fibers have intermediate to high strength, low material cost, high temperature resistance (800 °C), transparency to visible light

and isotropic properties due to amorphous structures [8]. But glass fibers have high density, susceptibility to surface damage, sensitivity to attack by moisture or alkaline [8]. In addition, During glass fiber production and recycling, high-toxic metals and oxides may be produced and come out to the environment [9].

During the glass fiber spinning operation, “size”, “finish” or “coating” is often applied to the fiber surface. Sizing protects the glass fiber from abrasion, damage or degradation during the subsequent handling processes and molding operations, and sizing also helps to bind the filaments together. A finish or coating, like a silane coupling agent may be incorporated into in the sizing to control the degree of wetting and bonding of the filaments by matrix. The degree of coherence of the strand and the choice of the finish are very important to the glass fiber behavior during processing [10].

Carbon/Graphite fiber: The raw materials of carbon fibers are polyacrylonitrile (PAN), cellulose (rayon) and pitch [11]. Fibers are made from these materials in three steps: stabilization at 400 °C, carbonization at 1200 °C, and graphitization at 1000-3000 °C [12]. Fiber diameters are usually 4-10 micron and may be of circular, dog-bone, or irregular cross sections [10]. Carbon fibers have high strength and stiffness with low density, high thermal and electrical conductivity with low thermal expansion coefficient. They are chemically inert. However, they are much more expansive than glass fibers and they show high anisotropy and brittleness [8].

A surface treatment usually by oxidation for carbon fibers is designed to improve the adhesion between fiber and matrix. A light size compatible with the matrix is also often applied for easy handling [10].

Basalt fiber: Basalt fibers have similar chemical components and mechanical properties as glass fibers. Basalt has a brown color whereas glass fiber is usually much lighter in color.

Synthetic fibers: they are polyaramid fibers, such as Kevlar [11], a polymer that is stiffened by benzene rings. They have cost, strength and stiffness intermediate between glass and carbon with low density. They are tougher than glass and carbon fibers but more difficult to

cut and weak in compression. They do not bond as well to conventional matrix like epoxy and vinylester so the choice of sizing or finish is very important [10].

Natural fibers

Raw materials of natural fibers come from [13] mineral, vegetable and animals, such as bamboo, banana, flax, jute, sisal or agave, hemp, wheat straw, pineapple and silk. The advantages of natural fibers are recyclability, low raw material cost and high raw material availability, low density. So they are used a lot [14-19]. However, they are usually non-compatible with polymer matrix, and they have low dimensional stability, low mechanical properties, low durability and poor fire resistance.

III. Fabrication of Fiber Reinforced Composite Materials

1. Hand Layup

Hand layup of prepregs followed by autoclave cure is the most important process for composites in aerospace application [20]. In hand layup [2], first the mould is cleaned and coated with mold release agent, a thin gel coat (resin or some pigment) is applied and will become the outside surface of the finished part, successive layers of resin and mats of fiber are applied when the gel coat is partially set, with the mat of fiber rolled to have the resin fully impregnate the fiber and remove air bubbles, finally part is fully cured and removed.

Hand layup is very flexible, capable of making a lot of shapes. It doesn't require large investment because of its simple molds. However, this process is labor intensive and time-consuming. The properties of the finished parts also depend on operators' experience greatly.

2. Spray-up

Spray-up is also an open mold technique. Chopped fibers together with liquid resin are sprayed onto an open mold surface until the desired thickness is reached. Spray-up is used to produce various components: boat hulls, shower stalls, bathtubs, automotive body parts, tanks, containers and furniture.

Compared to hand lay-up where fibers may be continuous and aligned, short fibers are randomly oriented in spray-up. Therefore, products made by spray-up have lower strength

than those produced by hand lay-up. And, due to the mixing methods in spray-up, there is a limitation to the fiber volume fraction: 30~35%, while in hand lay-up it can reach 65~70%. However, spray-up has its advantages. Spray-up is much quicker and less labor-intensive than hand lay-up. Simpler and cheaper molds can be used in spray-up and the process sometimes is portable and versatile.

3. Bag Molding and Curing [2]

In hand lay-up and spray-up processes, bag molding is used sometimes as a supplementary process to curing, in order to compact the lamination on the open mold surface, or drive out volatiles by applying pressure or vacuum. There are two basic methods: vacuum bag molding and pressure bag molding.

4. Autoclave Molding Process

Autoclave includes a pressure vessel inside which a complex chemical reaction occurs. Continuous load-carrying fiber architecture is impregnated with resin and is ready for use. The material is layed up to the final shape and put in the pressure vessel. The material is covered with a flexible film and vacuum is applied to evacuate air. The pressure vessel is closed and then pressure and heat is applied to cure the material.

Autoclave process produces high-quality composite materials for aerospace applications, because high fiber volume fraction can be reached (up to 75%) and continuous fibers can be aligned in the desired directions. But it requires high investment and operation costs, so it's only suited for high-end applications like aeronautical industry or race cars.

5. Liquid Composite Molding (LCM)

First, the reinforcement, or the fabric material is pre-placed in the mold. Catalyzed liquid resin is injected to the mold and resin flows inside the reinforcement material, which is a porous media. Resin is cured during and after the injection process. Many variants of this technique exist. Injection/compression molding has fast resin driven by mold closure with unknown product quality. Resin transfer molding (RTM) has slow to medium flow (approximately 10 ml/sec) of resin driven by pump, and the part quality is low to medium due to difficulty in controlling fluid flow behavior. Seeman Composite Resin Infusion

Molding Process (SCRIMP) has solid tooling on one side, vacuum bag on the other side, slow resin (approximately 1 ml/sec) driven under vacuum pressure, and medium quality products due to consolidation pressure. SCRIMP is good for large part production. Structural Reaction Injection Molding (SRIM) has solid and strong tool. Resin is injected to the mold fastly (approximately 100 ml/sec) by high pressure, and the part quality is low to medium due to problem in controlling flow and perform deformation. Vacuum Assisted Resin Transfer Molding (VARTM) has solid tool. Medium resin flow is driven by pump and vacuum pressure, and the part quality is medium to high because the vacuum helps to remove air bubbles and moisture.

6. Filament Winding

Filament winding involves wrapping (usually wetted) continuous reinforcements (fibers) or mono-filaments around a rotating mandrel and curing to produce closed-form hollow parts [20] Filament winding works well with parts of rotational symmetry. It has a high repeatability, low capital and process cost. It can easily exploit the dimensional strength of the continuous fibers by changing the winding angles and patterns. Huge parts can be produced in filament winding. High fiber volume fraction can be achieved and so high strength can be reached. However, in case of complex shaped parts, complex mandrel designs and cost are required. Mandrels are usually indispensable but expensive. In addition, surface quality is usually low and extra surface machining is required.

7. Pultrusion

Continuous strands of reinforcement are being fed into the resin bath, and they are subsequently led into a curing die. The curing die is the mold which shapes the final part. The resin is cured completely when it exits the curing die. The cured part is then pulled by a clamping and pulling system, and such process automatically introduces new materials to the curing die. Pultrusion is a continuous process which generates composites mainly in longitudinal direction.

8. Reaction Injection Molding (RIM)

RIM is a closed system. The reaction components are mixed together before they enter the mold. Sometimes there are chopped reinforcement strands in one of the reaction components,

and such system is called Reinforced RIM (R-RIM). Sometimes there is reinforcement pre-placed in the mold, and this is called Structural RIM (S-RIM). RIM requires strong solid molds since usually injection pressure is high. So the production facility costs a lot and is good for high volume production.

9. Sheet Molding Compound (SMC)

SMC is the most widely used composite production technique. In 1999, 52% of the total production in European Composite market came from SMC [21]. In SMC, dry chopped reinforcement strands are sprayed onto a film of catalyzed resin and additives, which was held by a carrier film. And the system is covered by a second film of resin, and then compressed to a certain thickness. This pre-impregnated and reinforced layer can be rolled and stored for a few days. Before application, the necessary amount of prepreg is cut from the roll and placed in the mold, where it is shaped and cured to the final product. SMC is able to produce large parts in a high production rate and the cost is less than RTM. However, it's difficult to control the orientation of the reinforcement.

10. Bulk Molding Compound (BMC)

In BMC, the mixture of catalyzed resin and chopped reinforcements is immediately injected into the mold by extruder, without the prepreg stage in SMC. Due to the injection step, the fibers are shorter than those in SMC and the achieved fiber volume fraction is usually lower. However, BMC allows adding more filler material to the resin [20].

11. Thermoplastic Compounding and Injection Molding

The thermoplastic material like PP is melted and mixed with chopped fibers in the extruder, and thin rods are produced and then solidified by cooling. Next they are chopped into small pellets and bagged. In the production of composite parts, the pellets are remelted and injected into the closed mold.

12. Glass Mat Thermoplastic (GMT)

A random mat is consolidated with a sheet of PP. The system is heated in the oven to the melting point of PP so that the mat is impregnated. Then it is cooled to half-product. The

half-product can be used for the production in a compression mold where the sheet is reheated and shaped. GMT offers a high level of automation.

Part II. A Brief Description of Textile Polymer Composite

Mechanical Properties & Durability

Solids are divided into four classes: metals, ceramics, glasses and polymers [22]. Polymer composites are made using polymer matrix and fibers or fillers, and they are the most important category of composites. The reinforcement can be particle, short fibers (also called whiskers) and long (or continuous) fibers.

I. Static Mechanical Properties

1. Unidirectional (UD) Composites

Composite materials reinforced with straight and parallel fibers are usually referred to as UD composites. The direction where the fiber goes is called the longitudinal direction, and the other two are referred to as transverse directions.

The properties in the longitudinal direction depend greatly on the fiber volume fraction, not weight fraction, like Young's modulus, tensile strength, compression strength. The first approximation of the extensional modulus in the fiber direction for UD (unidirectional) composites is given by rule of mixtures [23], which is only valid for longitudinal extensional modulus:

$$E_1 = v_f E_f + v_m E_m \quad (\text{A-1})$$

The rule of mixtures states that Young's modulus of the composite materials in the longitudinal direction E_1 is a summation of those of the two components E_f and E_m , weighted by their individual volume fraction, v_f and v_m .

For UD composites, the transverse moduli E_2 and E_3 and shear moduli are sensitive to fiber geometry [24-28]. In the transverse directions, properties can be thought as isotropic if fibers

have no preferred orientation in these two directions. If two directions are labeled as 2 and 3, with 1 referred to as the longitudinal direction, transverse isotropy is described as

$$G_{23} = \frac{E_2}{2(1 + \nu_{23})} \quad (\text{A-2})$$

where G_{23} represents the shear modulus, E_2 the Young's modulus in the 2 direction.

Unlike the moduli, strength properties are governed by very complex failure modes and difficult to predict [5]. However, since the modulus of fiber is much larger than the matrix, most of the stress is carried by the fiber in the composite. So fiber volume fraction is also extremely important for composite axial tensile and compressive strengths. Composite axial stiffness and strength depend mainly on fiber properties, while polymer matrix is also important to axial tensile strength. Due to the size effect, fiber tensile strength decreases as the length increases. So in large composite structures, the projected mean fiber strength is quite low. Fortunately polymer matrix localizes the effect of fiber breaks [5] so that the ineffective length [22] rather than overall length becomes the reference dimension for tensile strength. Thus composite tensile strength is much higher than these values. The ineffective length depends on the mechanics of stress transfer between the matrix and fiber [23]. Usually it is of the order 10^{-4} m and the better the interfacial bonding, the smaller the ineffective length. More specifically speaking, once a fiber breaks in tension, any of the four possible subsequent failures may happen, depending on the properties of the fiber, matrix, interface, shown in Figure A.3 below [29, 30]. In Figure A.3, 'F' represents a single fiber. In case (a), there is a tough matrix and strong interface, so fiber fractures at another location as the stress increases. In case (b), there is a weak interface and the interface was destroyed near the broken part of the fiber. In case (c), there is a weak matrix and the matrix was destroyed after the fiber breaks. In case (d), both the matrix and the interface are strong, stiff and tough, and there is a stress concentration large enough to cause the fracture of the neighboring fibers. Usually in case (a), the best tensile strength is achieved [31, 32]. The subsequent failure mode also depends on the load level and loading rate, in that high loading rate may result in case (c) to happen and decrease the composite strength.

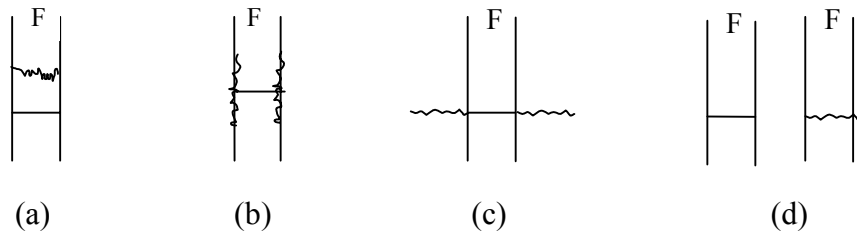


Figure A.3 Crack Growth Modes in Tension Stress

The study of tensile failure also led to the study of size effect on composite strength [33]. Usually the more volume of the materials under stress, the higher the possibility the material fails. This is also demonstrated by our experiment in this paper.

In axial compression, fibers buckle at small stress, but the composite axial compressive strength can be very high because matrix stabilizes the fibers and prevent them from further buckling. At high stresses, materials can fail by kink band formation due to fiber compressive failure, internal instability like buckling, interface debonding, matrix failure due to shear or delamination [4]. It's usually difficult to determine what the initial failure is which causes kink band formation, except that the instability failure is sensitive to imperfections like fiber local curvature and misalignment [34]. Local shear instability causes fiber buckling and then kink band. Polymer matrix helps to prevent fiber buckling, which causes kink band formation. In the case of delamination, the composites rely on the matrix toughness alone to resist delamination crack growth, so delamination resistance depends mainly on matrix materials and is usually low, especially in the presence of cracks. Therefore, Polymer matrix and interfacial properties are very important to composite axial compression properties, especially compression strength.

Transverse strength properties, including transverse tensile and compressive strength, and axial and interlaminar shear strength depend mostly on matrix strength properties, interfacial properties (the interaction between polymer matrix and fiber), imperfections like voids and microcracks due to curing stress and thermal stresses [5]. The failure may happen in the interfacial bonds, matrix phase around the interfacial area, or fiber, depending on which is

the weakest point. Brelant and Petker found [35] that the interlaminar shear strength of UD glass epoxy composite increased with the increase of matrix strength until the latter reached 83 MPa, and then kept stable with the latter because the failure happened on the interfacial bonds after that. Adams and Doner modeled internal stress concentration problem in UD composite with a square array of fibers [36]. They found that the axial shear stress concentration factor increases with the increases of the ratio of axial fiber shear modulus over matrix shear modulus, and usually composites have the shear concentration factor between 2 and 3. Their modeled results qualitatively corresponded well with the experimental results of Woodberry and Boromeier [37]. Adams and Doner also found that the axial shear stress concentration factor increases with the decrease of fiber spacing (or with the increase of fiber volume fraction). Besides, it is common to find transverse cracking in composite systems subjected to a big temperature change due to the mismatch of CTE values (Coefficient of thermal Expansion) between fiber and polymer matrix.

2. Textile Composites

Compared to UD composites, fabric reinforced composites usually have less fiber volume fraction, which causes lower modulus and strength. Fabric composites also have fiber curvature due to crimp and twisting, which results in local stress perturbations and then lower modulus and strength [5]. Many fabrics are made from twisted yarns to facilitate the weaving process and reduce the damage problems. Crimp [38] is the waviness of the yarn due to interlacing of the fabric and calculated as the difference between yarn length and fabric length divided by the fabric length. Yarn thickness, rigidity and weave patterns control crimp values. Usually the thicker the yarn or the higher the yarn rigidity is, the higher the crimp. Crimp also decreases in compression. Due to the waviness, fabric composites have modulus lower than corresponding UD composites. Cox [39] derived the knockdown factor for stiffness due to crimp by assuming that the waviness takes the sinusoidal oscillation form with wavelength λ and amplitude d , and either the stress or strain remains uniform along the tow:

$$\eta = \left\{ 1 + 2 \left(\frac{\pi d}{\lambda} \right)^2 \left[\frac{E_x}{G_{xy}} - 2(1 + \nu_{xy}) \right] \right\}^{-1} \quad (\text{A-3})$$

where E_x and G_{xy} are axial and shear moduli of the tow and ν_{xy} is the axial Poisson ratio. So, the fractional loss of modulus, $(1-\eta)$, rises as d/λ increases. For satin weaves, $(1-\eta)$ is typically 10%, and plain weave has even larger $(1-\eta)$ [37].

Tow waviness also generates off-axis local stresses, which decreases tensile or compressive strength of the composites. While the mechanism that waviness lowers tensile strength is less clear, it does greatly affect the tensile strength [40, 41]. Therefore, fabric reinforcing efficiency strongly depends on the percentage and severity of fiber curvature [42]. The reinforcing efficiency is the ratio of the composite property (modulus, strength) over the fabric property. Long shaft satins tend to have higher stiffness and strength than corresponding plain weave with the same thick yarns, and the same fabric (made of thinner yarns) reinforced composites are stiffer and stronger than that (made of thicker yarns) reinforced composites [5]. The composite tensile strength is also sensitive to the fiber damage, in that the knockdown of tensile strength due to fiber damage is much larger than that of compression strength [37].

In compression, the composite fails when one set of tows have kink band formation [37, 43-45] (shear failure between matrix and fiber results in debonding or matrix cracking) or delamination happens [43]. These two mechanisms sometime combine each other, with one following the other. Argon's law [46, 47] illustrated the kink band formation as a local shear instability in which a bundle of fibers rotates or ruptures and then causes the loss of axial strength.

$$\sigma_c = \tau_c / \phi \quad (\text{A-4})$$

where σ_c is the critical axial stress for kinking, τ_c is the critical shear stress, and ϕ is the misalignment angle in radians of the fiber relative to the load direction. In the curve of shear stress versus strain, τ_c is the shear stress at which the deflection of the curve happens and after which the response is totally plastic. τ_c depends mainly on polymer matrix properties [37]. Even before Argon's law, Davis [34] already demonstrated the importance of fiber curvature on compression strength. Because fiber damage has a negligible effect on dynamics and kinetics of shear flow and fiber rotation, which are the reasons for kink band formation, fiber defects have only marginal effect on compression strength. As for

delamination, composite resistance to delamination crack growth depends mainly on polymer matrix properties [37]. Fortunately, a few percent by volume of through thickness reinforcement can greatly increase the fracture toughness [48-50].

The in-plane shear strength also decreases as waviness increases [51], or one may say shear strength decreases as float [38] decreases.

In textile composites, geometrical irregularity is manifested in many ways [37], like uneven tow spacing due to draping process, tow waviness due to tow misalignment, tow pinching due to irregular pressures imposed on each tow during processing, fabric shearing in processing. The severity of irregularity is related to the fabric architecture, as explained earlier in the discussion of the difference between different woven fabrics: plain weave, twill, satin, and harness. For example, usually the more crossovers per unit area, the less severe is the shear deformation problem [8]. And even in UD composites, such irregularity exists, like fiber curvature during processing. This curvature is different from the curvature in woven fabric. The curvature of fibers can result in tensile modulus increases with tensile strain, but compressive modulus decreases with compressive strain [5]. And such phenomena usually do not exist for the curvature of fiber in woven composites, because the curvature is constrained by the fabric architecture. Irregularity is very difficult to predict, but affects considerably composite stiffness [39, 52, 53], fracture toughness, strength and fatigue life [53-57]. The effect of irregularity on fabric permeability will also be discussed.

3. Silane Coupling Agents

From the discussion of the mechanical properties, especially strength properties, the interaction between fiber and matrix material is clearly of great importance. The fiber surface chemical or physical structure, and fiber surface treatments are known to change the compatibility between resin and fiber, and the durability and resistance of the composites to environments [58]. Silane coupling agents are well-documented surface treatments designed to improve the fiber-matrix interfacial bonding strength [58]. In fiberglass industry, glass fiber is given a treatment about 1% or 2% by weight at the time of forming, called size, which consists of lubricant, binder and antistat, and provides surface lubricity and binding action. After the fiber is weaved to fabric, the fabric can be heated in air-circulating ovens to

burn the size away, and then another surface treatment, finish is applied on the fiber surface from solution. Finish is usually 0.1% by weight of the fabric. Silane coupling agent is the main component in finish.

Generally silane coupling agents have structure, $R(\text{CH}_2)_n\text{SiX}_3$. The X groups represent hydrolysable groups, like chloro, alkoxy or acetoxy groups. These groups hydrolyze in the presence of water, and then react with the silanol groups on the glass fiber surface through condensation reactions. They also undergo a self-condensation reaction with one another. The R groups represent organofunctional groups which react and adhere to the polymer phase. The basic concept of the coupling effect is to “bridge” the chemically incompatible components through chemisorptions or physisorption of some chemical reagents to both components and so improve the adhesion between them. The chemical bonding theory proposed [59] that covalent bonds are formed between chemical functional groups on coupling agents and silanol groups on glass, and that coupling agents also contain different functional groups which coreact with matrix resin during cure.

The interaction between silane coupling agents and matrix polymer was indirectly demonstrated by FTIR [60, 61]. And Cross-condensation between coupling agent and fiber was observed during cure [62]. Due to the different interaction between silane modified filler surface and the matrix polymer, the interfacial zone can be deformable [63] because silane coupling agent provides mechanical relaxation through a deformable layer of silicone resin, which maximize the composite toughness, or restrained [64] because coupling agents function by “toughening up” the polymer structure at the interface and simultaneously provides silanol groups for bonding to the interface, which results in excellent chemical resistance.

Since silanol groups are necessary for proper performance of silane coupling agents, a period of time is needed for silane to hydrolyze in the presence of water. Generally alkoxy silanes with neutral organofunctional groups don't have good solubility in water until slowly hydrolyze, and the hydrolyzation can be catalyzed by acid or base [58]. Solubility of the hydrolyzates also decrease as silanols condense to oligomeric siloxanols, and the hydrolyzates lose the usefulness at the point of haze formation [65].

Silane coupling agents are not deposited on the fiber surface as simple oriented monomolecular films [66, 67], but are a thick and non-uniform layer. This thick layer consists of three fractions according to the adhering tenacity to the fiber surface. Fraction I, about 98% of the total and 270 monolayer equivalents, consists of silane hydrolyzates physically adsorbed on the fiber surface, and can be easily removed by cold water or organic solvents. Fraction II, about 10 layer equivalents, is a chemisorbed polymer of the coupling agent, can be removed by 3-4 hours' exaction in boiling water. Fraction III, equivalent of a monolayer, appears after fraction II is removed. This layer consists of silane monomer, dimer and trimers which are chemically bonded to the fiber surface. Only fraction II and III helps the interfacial bonding.

For the proper silane performance, the molecules should orient themselves so that they have organofunctional groups toward the matrix resin. The properties of the filler surface, like IEPS (isoelectric point of the surface) and acidity, and the silane application method, like PH value of the solution, water content, temperature, functional group on silane structure affect the orientation of silanes, all affect composite mechanical properties [68, 69]. Vice versa, application of silanes changes IEPS of the filler surface. The interaction between filler surface and silanes can be simple electrostatic force, acid-base reaction, hydrogen bonding, or covalent oxane bonds. In reference [36], a cationic vinylbenzyl functional silane (CSS) (structure shown below) was applied on the silica surface, from aqueous solution in a PH range from 2 to 12. Silica has an IEPS of 2 to 3, the negative charges on its surface increases as PH increases, so the cationic silane orients with amine towards the silica surface. When PH is decreased toward 2, silica becomes less negative and amine becomes more positive. Below PH=2, silica repels amine so now the silane orientation is just the opposite. At IEPS, there is minimum charge on both silica and silane, so they approach each other and form hydrogen bonding and siloxane, so the flexural strength of the silica reinforced polyester composites attains maximum.



The orientation of silane coupling agents on the filler surface also has an effect on the surface tension, which affects the wettability of the surface.

It is noteworthy that the performance of silanes paralleled reactivity of the R groups with the matrix, and not polarity (characterized by solubility parameter δ), nor wettability of the treated filler surface [70, 71]. While solubility effects may alter macromolecular orientation in the interphase region.

Through optimized applications of silane coupling agents, composite mechanical properties and environmental durability are greatly improved [70-76]. The flexural strength of Silica/polyester composites was improved from 115 MPa to 156 MPa at dry state through application of Z-6032 silane [71], and from 70 to 139 MPa for the samples aged in boiling water for 2 hours. The flexural strength of polyester-glass laminates with methacrylate silane coupling agent was 668 MPa at dry state and 641 MPa after aging in boiling water for 2 hours, compared to 482 and 365 MPa for the laminates without such silane modification [72].

However, the interfacial bond strength is very difficult to measure. A number of methods have been utilized to measure interfacial bond strength [58, 77], like short beam strength test, single fiber pull-out test, single fiber fragmentation test, and Nano-Indentation test. The failure mode in the pull-out experiment is quite complex and this test only gives a lower bound of the interfacial shear strength.

Some people have done the surface treatment on basalt fibers [78-90]. Park [78, 86] found that 3-(4-methoxyphenyl) propylmethyldichlorosilane improved the interfacial bonding between basalt fiber and phenolic resin, and 3-aminopropyltriethoxysilane bonded basalt fiber quite well with isocyanate resin. Shu [81] found that basalt fiber modulus dropped as diameter increased and strength decreased as fiber length increased. He used single fiber pull out experiment to test the interfacial bonding strength, and found the interfacial shear strength to be over 50 MPa with γ -methacryloxypropyltrimethoxy silane for basalt polyester composite, much higher than 23 MPa for E-glass obtained by the same method. In addition, Aminopropyltriethoxy silane and Glycidoxypropyltrimethoxy silane worked well with epoxy resin matrix since they have R group reactive with epoxy. Furthermore, n-butyl amine

could promote hydrolysis and self-condensation of the Glycidoxypropyltrimethoxy silane. Besides, PH of the application solution had a great effect on the performance of a cationic vinylbenzyl functional silane (CSS), and the reason was discussed above.

Although these references gave us how different silane coupling agents behave in basalt reinforced polymer composites, the optimum application condition can not be predicted from a knowledge of basalt fiber compositions, but should be determined experimentally. Because, Auger electron spectroscopy showed basalt fiber surface composition varied considerably with the fiber processing history [81]. Similarly the difference also was found for glass fiber [91]. The surface compositions [91] of E-glass and S-glass fibers examined through Auger spectroscopy were much different from bulk glass. Compared to bulk glass, E-glass surface is low in magnesium, boron and calcium, but high in fluorine, silicon and aluminum. S-glass surface is rich in magnesium and aluminum. When fiberglass is exposed to heat or acid environments, the concentration of elements on E-glass surface is changed [92], as has been observed by ESCA (Electron spectroscopy for chemical analysis) test.

4. Variability in composite mechanical properties

It is noteworthy that there is a real and inherent variability in even the most carefully prepared composite materials [93]. The variability can be attributed to the scatter in fiber and matrix properties, fiber spatial distribution, and void content. First of all, there is some variability in measured fiber volume fraction, which is an important source of the variation in published data. Even though, at a fixed fiber volume fraction, there is still considerable property variation. In reference [94], at fiber weight content = 20%, composite (E-glass mat/polyester hand lay-up laminates) tensile modulus ranged from 2.8 GPa to 6.9 GPa, and flexure strength ranged from 145 MPa to 185 MPa. It was also difficult to determine whether such big variation resulted from real property variability or poor test results, probably both.

Voids cause severe internal stress concentrations in the materials, so the composite strength drops quickly with void content. Yushida [95] found that interlaminar shear strength of a glass/epoxy composite dropped linearly from 89.62 MPa at 0% void content to 16.55 MPa at 16% void content.

Due to such statistical nature, in engineering design, people usually define design allowable under which (stress or strain) the composite material is able to be used safely [5]. When material weight is not a primary concern, allowables are typically calculated by dividing the strength by a sufficiently large number, which is called a safety factor. In aerospace applications, extra weight is obviously a drawback. Another set of allowables, A-basis, or B-basis is used. A-basis is the value above which at least 99% of the population of the strength is expected to fall, with a confidence level of 95%. B-basis is the value above which at least 90% of the population of the strength is expected to fall, with a confidence level of 95%. Simply speaking, if the stress on the material \leq A-basis, then the survival probability for the material $\geq 99\%$, with a confidence level of 95%. If the stress on the material \leq B-basis, then the survival probability for the material $\geq 90\%$, at a confidence interval of 95%. A-basis value is more stringent, used in situations where failure of a component would cause structural failure. When A-basis or B-basis is used, care is required because complications may come into the calculations. First, if tensile strength is measured for n specimens, for example, the functional form of the ‘smooth curve’ which represents the population of the material tensile strength is not well known. Typically, only the normal distribution is assumed as the description for the various data scenarios. Secondly, the population mean may vary with some factors like temperature, humidity, and aging time under some environment. Or, as the outer environment changes, population also changes as well. In addition, population mean may vary from batch to batch. In this case, the population variance should consist of between-batch variance and within-batch components. If the data from all batches is pooled, there is a risk of underestimating the population variance and overestimating the design allowables.

Besides fabric architecture and void content which affect the composite mechanical properties, different fibers also have different reinforcing efficiency. Zweben and Norman [96] compared the mechanical properties, including tensile modulus, tensile strength and compression strength between a [0/90] laminate and a balanced 8-harness satin fabric composite, to study the effect of fabric architecture on reinforcing efficiency. They found that the reinforcing efficiency was strongly fiber dependent, in that aramid fabric composites have similar strengths to [0/90] laminate, while graphite fabric or graphite/aramid hybrid fabric have much lower reinforcing efficiencies. This is due to the interaction between fiber

and matrix. Different interfacial bonding strength may affect composite strength a lot. For example, epoxy matrixes seem to provide higher room temperature strength values and elevated temperature characteristics for composites than polyester or vinyl ester matrixes, because they bond better to the fiber surface. But for elastic properties, they are quite similar as long as the fiber volume fractions don't differ too much [5]. In reference [5], the representative mechanical properties of different fiber reinforced epoxy UD composites at fiber volume fraction of 0.60 are given as reference. According to the dependence of different properties on fiber volume fraction, the properties over the range of fiber volume fraction from 50% to 70% can be extrapolated. Caution is in order when the matrix is not epoxy, when the fiber volume fraction is very high so that void contents tend to increase, and when the transverse properties are particularly important in the design.

II. Fatigue Properties

In fatigue tests, there are several stages for continuous fiber reinforced composites (CFC): cracks are initiated very early in the weakest ply relative to the loading direction, the number of cracks increases in the ply, cracks appear in the next weakest ply and cracks are joined by delamination, fibers in the load direction fail. Usually crack multiplication and delamination take most of the fatigue life, and crack multiplication process decelerate with fatigue. In a microscopic scale, fatigue cracks in the matrix can be initiated at free surfaces. Weak fibers can fail at a stress level much lower than the strength [29, 97] or in fatigue [29, 97, 98]. The broken fibers lead to more fiber fractures through crack growth modes (c) and (d), shown in Figure A.3 [29, 98] until composite fails.

In fatigue tension, the failure is similar to what happens in static tension, except that the fatigue sensitivity must be considered, which reflects the degree of the fatigue strength reduction as fatigue life increases. When the number of fatigue cycles is low, the failure of the composite depends on the fiber properties, but when the number becomes high, the matrix may fail before the fiber does because of its higher fatigue sensitivity [5]. Another difference between fatigue failure and static failure is that a laminate may not delaminate in static tension, but it may do so in fatigue. In addition, some people claim that the maximum number of cracks in the plies before final failure is larger in fatigue than in static tension [99,

100], while Reifsnider holds different views that the crack density in both fatigue tests and static tests reach the same equilibrium value before the material fails [101].

The stress-rupture lifetime exhibits a large scatter in fatigue [102], as also seen in our study. One of the most widely used functions to describe this distribution is the 2-parameter Weibull distribution:

$$R(t) = \exp\left[-\left(\frac{t}{t_0}\right)^\alpha\right] \quad (\text{A-5})$$

where α and t_0 are called the shape parameter and location parameter (or characteristic lifetime) respectively. t is the lifetime and $R(t)$ represents the probability of surviving time t . In static tension, Weibull distribution can be written as:

$$R(\sigma) = \exp\left[-\left(\frac{\sigma}{\sigma_0}\right)^\alpha\right] \quad (\text{A-6})$$

where σ represents the stress level and $R(\sigma)$ represents the probability of surviving stress σ . The Maximum Likelihood Method can be used to calculate the shape and location parameters [103] shown below, where σ_i is the stress level at which the material fails. Solving equation (A-7) gives parameter α . Then, substitute α into equation (A-8) to get location parameter σ_0 .

$$\frac{1}{\alpha} = \frac{\sum_{i=1}^N \sigma_i^\alpha \ln(\sigma_i)}{\sum_{i=1}^N \sigma_i^\alpha} - \frac{1}{N} \sum_{i=1}^N \ln(\sigma_i) \quad (\text{A-7})$$

$$\sigma_0 = \left[\frac{1}{N} \left(\sum_{i=1}^N \sigma_i^\alpha \right) \right]^{\frac{1}{\alpha}} \quad (\text{A-8})$$

Different shape parameters tell different rupture stories [30], and it may change with stress level. The study on Kevlar/Epoxy and S-Glass/Epoxy showed that at stress larger than 80% of the ultimate strength, α is less than 1 and the stress-lifetime relation is flatter. The stress rupture is controlled by initial defects. At stress less than 80% of ultimate strength, the shape parameter becomes larger than unity and the stress-lifetime relation assumes larger slope. Now the initial defects are not so important as they are in the previous case. The shape parameter may also depend on temperature. In [30], Hahn found that above 23 °C, the shape parameter doesn't depend on stress level, for Kv 49/Ep A system. The location parameter

also has a dependence on temperature. Hahn also found that for the Kv 49/Ep A system, the relationship was described as

$$\frac{S}{UTS} = -8.01 \times 10^{-2} \log(t_0 / a_T) + 1.065 \quad (\text{A-9})$$

where S is the applied stress. The factor a_T depends on temperature by

$$-\log a_T = 4.83 \times 10^3 \left(\frac{1}{T_R} - \frac{1}{T} \right) \quad (\text{A-10})$$

where T_R is room temperature (=296 K), and t_0 in equation (A-9) is for room temperature.

As material undergoes cyclic load in fatigue, its modulus and strength may go down with time [5]. Composites with viscoelastic matrix in cyclic load may also produce heat [104]. In the test, if the frequency is large enough to produce heat and increase material temperature, it results in a shorter life. Otherwise, an increased test frequency usually leads to a long fatigue life [105-107], and the number of cycles to failure increases with frequency in a manner that the total time under load remains constant [108]. In tension-tension fatigue tests for the polymer composites in this report, 0.5 Hz was used to make sure no extraneous temperature effects occurred.

III. Environmental Aging Behavior

People have done a lot to investigate composite material durability in different environments [109-123]. Fujji [109] found that for glass fiber reinforced vinyl ester composites, in acid condition, glass fiber was destroyed quickly, while in alkaline condition, the interfacial area is mainly destroyed.

The reason for the degradation people usually believe is the attack by water molecules, especially with ions, but sometimes fresh water can damage the materials more within a short time because free water molecules enter the material more quickly. Acid or alkaline environments do damage the materials, and salt ions also do because they help the oxidation process. Temperature really plays an important role in that high temperature usually accelerates the degradation in a very significant way, and high-low (freeze-thaw) cycling destroys the interfacial area very effectively due to the mismatch of the coefficients of thermal expansion (CTE) between fiber and matrix materials.

Zhang [112] found that the tensile strength of glass reinforced UD vinyl ester composites dropped by 26% in room temperature distilled water after 350 days and by 41% in 40 °C distilled water after the same amount of time, but it dropped by 30% and 69% in alkaline solution (PH=13) under room temperature and 40 °C, respectively, after the same amount of time.

Wu [114] aged some glass reinforced vinyl ester composites in room temperature salt water, room temperature distilled water, and wet-dry cycling in salt water. After 365 days, the tensile strength and Young's modulus of the materials dropped in all conditions. Tensile strength had the largest drop in salt water and minimum in wet-dry cycling in salt water, because water molecules diffused in to the specimen slower in wet-dry cycling and salt ion helped the oxidation process. The Young's modulus had the largest drop in salt water immersion and wet-dry cycling in salt water, which indicated that wet-dry cycling destroyed the interfacial region very effectively. The interlaminar shear strength dropped the largest in distilled water, because free water molecules diffused faster than water molecules with ions, into the midplane of the materials which sustained the highest shear stress.

If the interfacial area in the material is protected properly, the degradation happens much slower. Schultheisz [113] investigated two systems' aging distilled water: glass fiber reinforced epoxy composites with epoxy compatible silane on the fiber surface, and those with vinyl ester compatible silane. After 205 days' aging, the tensile strength of the composites with epoxy compatible silane stayed much the same, while it dropped by 30% for those with vinyl ester compatible silane.

Some people attained an interesting result about the relationship between moisture amount and the mechanical properties of the aged materials. Pritchard [116] found that the changes of the Young's modulus and tensile strength only depended on the water absorption, for the composite materials aged in distilled water, regardless of the immersion temperature. So he used such relation, and the water absorption kinetics of the materials under room temperature to predict the durability of the materials. Such predict was very primitive because it ignored the continuous damaging process of water on the fiber, matrix and interface inside the

materials even though the water amount is constant. Water continues to decompose the resin matrix and pit the fiber surface. Water attacks the glass fiber surface and this promotes pitting and produces free alkali hydroxide groups that further degrade the silica surface. Water molecules in the matrix continue to plasticize, lubricate the matrix with the movement of the macromolecular chains. All of these change the interfacial region. Matrix degradation and interface debonding may lead to continuous water absorption after a certain saturation, which the people might not be able to measure in their experiments [111, 116]. However, such prediction also indicated that the importance of the water amount in the materials. Since the absorption pretty much depends on the matrix materials, the matrix should be much more important to the durability of the materials than the reinforcement.

Part III. A Brief Description of RTM and Permeability for Textile Materials

Liquid composite molding techniques such as resin transfer molding (RTM) and vacuum assisted RTM (VARTM) are appropriate for producing large structures appropriate for civil engineering applications. A unique feature of RTM processing technique is that liquid resin has to flow a long distance to impregnate the dry fibers. The measure for the ease of the resin flow in the fiber preform is the permeability of the preform. Accurate permeability values are extremely important for the resin flow simulation and mold design due to the often encountered problems of non-uniform impregnation, void and dry spot formation [124], and lengthy impregnation cycles. With known permeability one can compute flow behavior in large complex molds with Darcy's equation, the pressure distributions accumulating in the mold to define the required pumping power, the required clamping pressure to hold the mold closed, and the required strength of the mold to retain its shape during the molding operation [125].

I. Introduction

Among all the composite processing techniques [13, 126], RTM, Resin transfer molding, is one that has gained rapid development recently [127]. RTM allows the molding of large complex shaped composite parts with a good surface finish and little pollution. This process consists of filling a rigid and closed mold cavity with reinforcements preplaced inside, by injecting a resin through one, or several points. (See Figure A.4 below) The acronym LCM

comprise a whole range of closely related production techniques including RTM: RTM, VARTM, SCRIMP and SRIM [13].

In the past, RTM was mainly used in aerospace and airforce department due to long formation cycle resulting from the trial-and error method [13]. Recently, RTM forwarded a large step in advanced sport goods, and automobile and architecture, with the help of software developed to assist the evaluation of a new mold design [124, 128] even long before mold making [129, 130]. But the rapid development for RTM depends on the understanding of the fabric perform to promise the production automation [127]. The key factor in studying the preform and simulating RTM process is by far the permeability of fibrous reinforcement in the mold cavity, while it's very difficult to model due to many influencing factors.

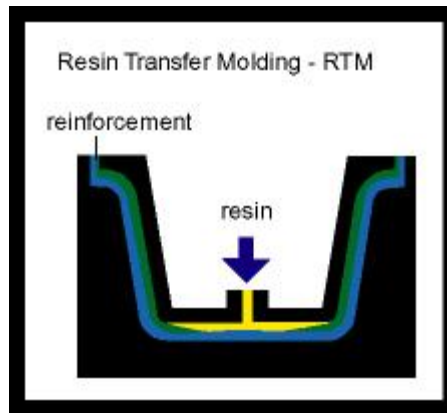


Figure A.4 Resin Transfer Molding Scheme

II. Theories

1. Darcy's Law [125]

The detailed flow behavior of liquid resins within a porous medium are described with the Navier-Stokes equation for incompressible flow [131].

$$\rho \frac{D\mathbf{v}}{Dt} = -\nabla P + \mu \nabla^2 \mathbf{v} \quad (\text{A-11})$$

If the problem is simplified by neglecting the material derivative of the fluid velocity vector because the typical flows in composites processing are very slow, then Navier-Stokes equation changes to the Stokes flow equation, or Creeping flow equation

$$\mathbf{0} = -\nabla P + \mu \nabla^2 \mathbf{v} \quad (\text{A-12})$$

To further simplify the problem, through the volume averaging procedure [132], the Darcy Equation is obtained

$$\langle \mathbf{v} \rangle = -\frac{\mathbf{K}}{\mu} \langle \nabla P \rangle \quad (\text{A-13})$$

where \mathbf{v} and ∇P are vectors, \mathbf{K} is a second rank tensor and μ is a scalar. \mathbf{v} is the fluid velocity, defined as the volume rate of flow through a unit cross-sectional area of the solid plus fluid, averaged over a small region of space—small compared to the macroscopic dimensions in the flow system, but large with respect to the pore size. ∇P is the pressure gradient, and the pressure is also averaged over a region available to flow that is large with respect to the pore size. μ is the viscosity of the fluid, and \mathbf{K} represents the three dimensional permeability tensor, a function of the porous medium geometry through the volume averaging operations, with units of L^2 . The brackets around the velocity and pressure gradient represents the volume averaging operation. Then our problem changes to computing averaged flow behavior with an equation containing an unknown quantity \mathbf{K} .

Although there exist some assumptions and limitations to it [13], Darcy Law has been widely used for many applications.

2. Definition of Permeability

The Permeability \mathbf{K} is an inherent property of a porous media, which characterizes the ease with which a fluid can be made to flow through the material under an applied pressure gradient [12, 133-137]. And it can be described as the ease with which fluid can pass through.

\mathbf{K} is uniquely determined by the pore geometry [138]. The most important parameter which affects permeability is the overall porosity of the media. From reference [125] one can see that permeability values may drop by an order of a magnitude once the porosity decreases by 10%. For the materials with the same porosity, the average hydraulic radius also affects the permeability behavior. Usually the larger the average hydraulic radius, the larger the permeability is [138]. Fabric materials have pores inside in the yarn and pores between the

yarns. Since the latter have much higher hydraulic radius, they contribute to the overall permeability for the materials much more importantly. Besides, the way the pores interconnect with each other also affects the permeability values. For fabric materials, every time they are laid in the mold, the ways they stack are not always the same, and so the pore structures created by the stacking for the system are not the same from time to time, which resulted in the broad distribution of permeability values for the same material with the same porosity (the standard deviation may range from 20~25% of the mean). For woven fabrics, more specifically, it is the different ways the neighboring layers nest with each other that result in the broad distribution [13]. Because of the frequent anisotropy of porous media (the pore structures are different in different directions), the relationship between flow rates and pressure gradients is often characterized by different values of the permeability for different flow directions. So normally K is a three dimensional symmetric tensor [13] which can be visualized by an ellipsoid in 3D or ellipse in 2D. K can be computed analytically for simple cases or numerically for more complex cases [139]. However, in real composite fabrication, K is difficult to determine by calculation because of too complicated porous media geometry.

From the previous part, the amount of fiber is very important to the properties in the fiber direction, like Young's modulus, tensile strength, compressive strength, and flexure strength. So from the point of the product final properties, it is preferred to have as much fiber in the materials as possible. However, when the fiber volume fraction goes up, the porosity of the fabric goes down, and the permeability drops quickly as well, which poses much more difficulty in the composite manufacturing in RTM. That is, the penalty of increasing the fiber volume fraction to improve the properties is to make the manufacturing more difficult and consequently enhance the cost of the materials, from an engineering point of view. Therefore, a balance between the properties and cost for the materials is required.

III. Permeability Measurements

The usual way of obtaining permeability values is by experiments. Two kinds of experimental methods for permeability measurement are distinguished: unidirectional flow methods [128, 137, 140-144] and radial flow methods [128, 134, 142, 144-146].

1. Unidirectional (UD) flow measurements

Unidirectional (UD) flow methods can also be distinguished by saturated and unsaturated flow methods (shown in Figure A.5 below). In the UD flow methods, permeability values in a specified direction are measured. In the saturated UD method, experiments are conducted by forcing a test fluid through the entire mold in which the fabric is preplaced and compressed, and measuring the steady-state relationship between the flow and the pressure drop across the whole length of the mold [144]. Usually a linear relationship is obtained between the steady-state flows of a Newtonian fluid and its pressure drops. In the unsaturated UD test, the fluid flows through the dry fiber bed, replacing the air present in the material.

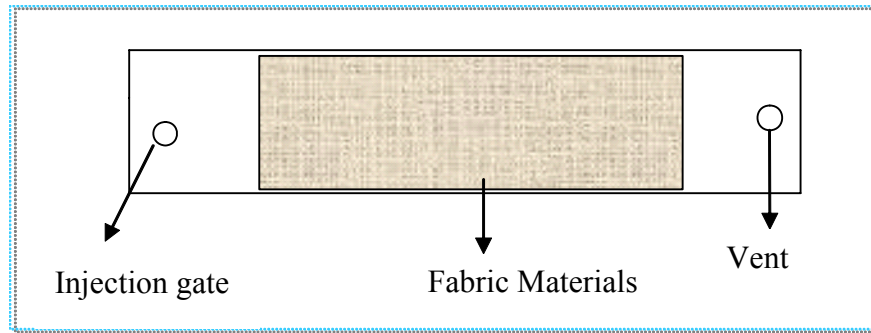


Figure A.5 Diagram of UD Permeability Measurement

In case of constant injection flow rate, unsaturated/dry UD tests,

$$\frac{Q}{A} = -\frac{K}{\mu} \frac{dP}{dL} = c \quad (\text{A-14})$$

$$L = \frac{Q}{A\phi} t \quad (\text{A-15})$$

where Q is the injection flow rate, A in the cross sectional area for the fluid flow, K is the permeability in the tested direction, μ is fluid viscosity, dP/dL is the pressure gradient, and L is the wetted length, c is a constant, ϕ is the overall porosity.

Then,

$$P = \frac{Q^2 \mu}{A^2 K \phi} t \quad (\text{A-16})$$

Plot the inlet pressure P versus injection time t, and from the slope derive the permeability K.

In case of unsaturated, constant injection pressure experiment,

$$v = -\frac{K}{\mu} \frac{dP}{dL} = \frac{K}{\mu} \frac{P_{in}}{L} = \frac{dL}{dt} \phi \quad (\text{A-17})$$

where P_{in} is the pressure measured at the inlet, which is the real injection pressure minus the atmosphere pressure. Integrate this equation to get

$$K = \frac{1}{2} \frac{\mu \phi L^2}{P_{in} t} \quad (\text{A-18})$$

By measuring the time t needed for the fluid flow front to reach a certain distance L at constant injection pressure, derive permeability K . In case of constant flow rate injection, saturated UD experiment,

$$\frac{Q}{A} = -\frac{K}{\mu} \frac{dP}{dL} = \frac{K}{\mu} \frac{P_{in}}{L} \quad (\text{A-19})$$

Then
$$P_{in} = \frac{L\mu}{AK} Q \quad (\text{A-20})$$

At different flow rates, Q , different P_{in} values are obtained. Plot P_{in} versus Q , and from the slope derive the permeability K . In case of constant injection pressure, saturated UD experiment, control the inlet pressure P_{in} , measure the flow rate Q , and plot P_{in} versus Q to get K .

In the derivations above, the overall porosity, ϕ , is used. In the material, there are between-yarn pores and between-fiber pores inside a yarn, therefore

$$\phi = \phi_y + \phi_f \quad (\text{A-21})$$

where ϕ_y represents the volume fraction taken by the inter-yarn space, and ϕ_f that taken by intra-yarn space. For the basalt fabric used in this report, $\phi_y + \phi_f = 0.6425$ because the total porosity of the fabric specified is 0.6425. Besides, the fiber volume fraction inside the yarn in the composite materials is 60~70% generally [3], and 0.92 for closest packing. If $\frac{1 - 0.6425}{1 - \phi_y} = 0.65$, then $\phi_y = 0.4500$ and $\phi_f = 0.1925$. In the permeability test, the distance

between yarns is much larger than that between fibers inside a yarn, which results in that the hydrolytic radius [138] for the inter yarn pores is much larger than that for the intra yarn pores, so the contribution from the inter yarn pore spaces is much more important than that from the intra yarn pore spaces, especially at low fiber volume fraction (< 0.50).

Although the UD test is the most straightforward set-up, there are a number of errors associated with it. The most serious one is the “race tracking”, or “edge effect” error [125]: a small gap between the edges of the preform and the mold wall results in that the fluid prefers to flow through the edge. Race tracking makes the apparent permeability much larger than the real values. According to Neale [147] and Parnas [148], the sensitivity of the UD test to the edge effect is a function of the mould width. Many people have made efforts to minimize the error due to the edge effect in their measurement. Diallo [140] et al. and Binetruy [149] et al. used silicone sealant, Parnas [150] et. al. and Lekakou [145] et. al. used a piece of sticky tape on the material edge. Another disadvantage of the UD test is that at least three measurements have to be done to fully characterize the in-plane permeability tensor: one for the permeability values in two perpendicular axes and one to derive the angle with respect to the reference axis. Thirdly, mold deflection problems (especially associated with transparent plastic mold lids) and the problems due to incomplete saturation also exist [8]. Besides, in the UD tests, if the direction for measuring the effective permeability is not one of the principal directions and the anisotropic ratio of the material is high, then the fluid flow front may not be perpendicular to the flow direction because the non-diagonal components of the permeability are not zero. Such phenomena may pose some difficulty in determining the flow front, which is already fuzzy.

2. Radial Flow Measurements

The radial test (or 2D test) can only be used in unsaturated flow. The set-up typically consists of a lower metallic mold-half with an injection hole in the middle, and a transparent mold top. Inside the mold, the fluid flows through the fabric from the central injection port. Constant injection flow or constant injection pressure can be used as injection conditions and the procedures how to derive the permeability can be found in the reference [8]. Pressure transducers can be used to measure the pressure at different positions. The transparent top-half allows recording the flow front progression by means of a video camera for later derivation of fluid superficial velocity. The main advantage of the 2D test is that it allows the determination of both in-plane permeability components and their angle with respect to the reference axes all in one single experiment [13]. This implies that it is much less time-consuming than a set of UD tests. However, the data reduction procedure which converts the

pictures of flow front positions to usable digital values is still time-consuming. In addition, the material and the flow front have to be visible throughout the experiment to allow the use of a video camera. In case carbon fabric is used, the contrast of the image or video is not very good which results in difficulty in processing. Furthermore, the mold deflection problems [142] associated with the transparent top of the mold are at least as troublesome as in the UD method. To counter this problem, the transparent top plate is often covered with a steel frame to enhance bending stiffness [142], but this reduces the visibility. Another problem with the radial flow comes from the error in the inlet hole dimension. The inlet hole has to be cut in the radial flow measurement, in order to help the flow expand within the material thickness evenly. The error in the determination of the hole radius has a big effect on the results of the permeability measurement [141]. Finally, the radial flow measurement is also associated with the problem of the diverging flow: the deformation of the preform and so the deviation of permeability value from the overall permeability near the inlet hole [141].

To counter the mold deflection problems associated with the 2D tests, Hoes [13] designed and built equipment in which both the top-half and the bottom-half were made of stiff metal plates. The bottom-half is a sensor plate, and contains 43 electrical sensors located on straight lines at 0, 22.5, 45, 67.5, 90, 180, and 270°. The sensor plate is placed at a low electrical potential of e.g. 5V. So, if an electrically non-conductive fabric is used in combination with a conductive test fluid, the fluid will generate a conductive bridge between the plate and the sensor core, which allows recording the flow front progression as a function of time. A pressure transducer is positioned in the injection tube just below the surface of the sensor plate to measure the injection pressure. All the sensors and the pressure transducer are connected to a PC through an automated data acquisition system. Automated software provides the permeability in a few seconds after the experiment. Automation of the experiment and data analysis greatly saved time compared to the usual 2D tests. A test frequency of five to ten measurements per hour is easily achieved. A drawback of the set-up is the fact that only non-conductive materials can be tested, since conductive materials would short out all the sensors at once. In addition, the distribution of the sensor only on one quarter area of the sensor plate causes relatively large experimental errors. Besides, this set-up only takes data from the bottom sensor plate, so it is not able to check whether the fluid has any preferential flow direction through the thickness, i. e. whether the direction of the principal

permeability through the thickness of the fabric material is perpendicular to the material plane. Finally, Hoes had to make the assumption that permeability principal directions coincide with the material coordinates, and for each system he measured he had to use the traditional methods to check the validity of his assumption.

From Hoes and other results, permeability data exhibits a large relative standard deviation, as much as 20% [128, 136, 141, 151-155], as discussed before. So permeability is a statistically distributed parameter and can not be characterized by only a few experiments. Rapid measurement methods for permeability may therefore prove useful for validating models and providing realistic processing data.

IV. Factors that can Affect the Measurement of Permeability [13]

The measured K can be different than the real value of K because of many experimental artifacts [135, 136, 156], which should be taken good care of in the real composite processing although this paper mainly deals only with mathematical models for true permeability calculation.

1. Test Methods

a) Wet versus Dry Experiments [140, 141, 149, 152, 153, 157-161]

In wet or saturated experiment, the situation satisfies Darcy's law. But in dry experiment, it doesn't and there may be some effect from wettability of fluids. Different wettability results in different contact angle between fluid and fiber surface, and so different capillary pressure, which produces the micro flow inside the yarns. If the micro flow front is well ahead of the macro flow, because capillary pressure plays an important role under low injection pressure, the fluid may enter the macro pores from the micro pores, and entrap an air bubble. The process is shown in Figure A.6 below. If the macro flow is well ahead of the micro flow, because the capillary pressure is so small compared to the mechanically applied driving pressure, then the fluid may come from the macro pores to the micro pores and also entrap air bubbles, as shown in Figure A.7 below. If the case as in Figure A.6 happens, then theoretically one expects higher permeability measured from the experiment than the real value.

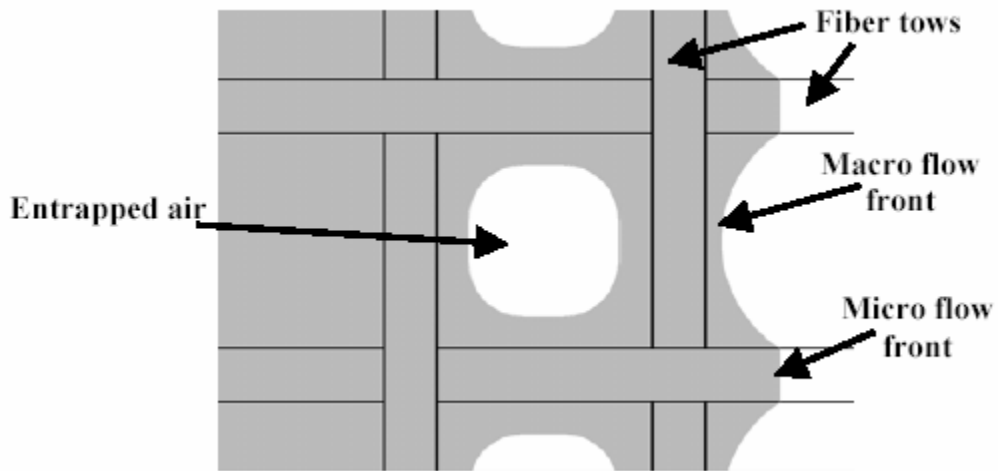


Figure A.6 Air-Entrapment Mechanism I

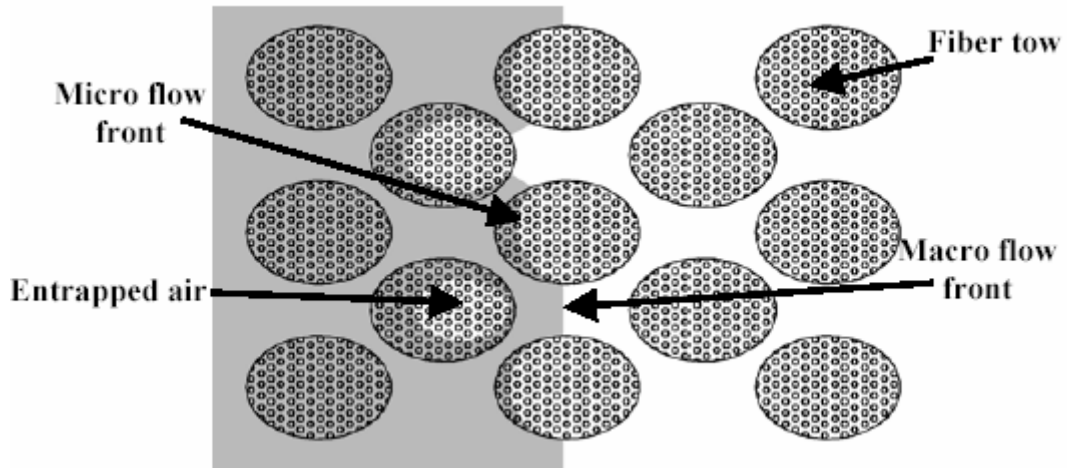


Figure A.7 Air-Entrapment Mechanism II

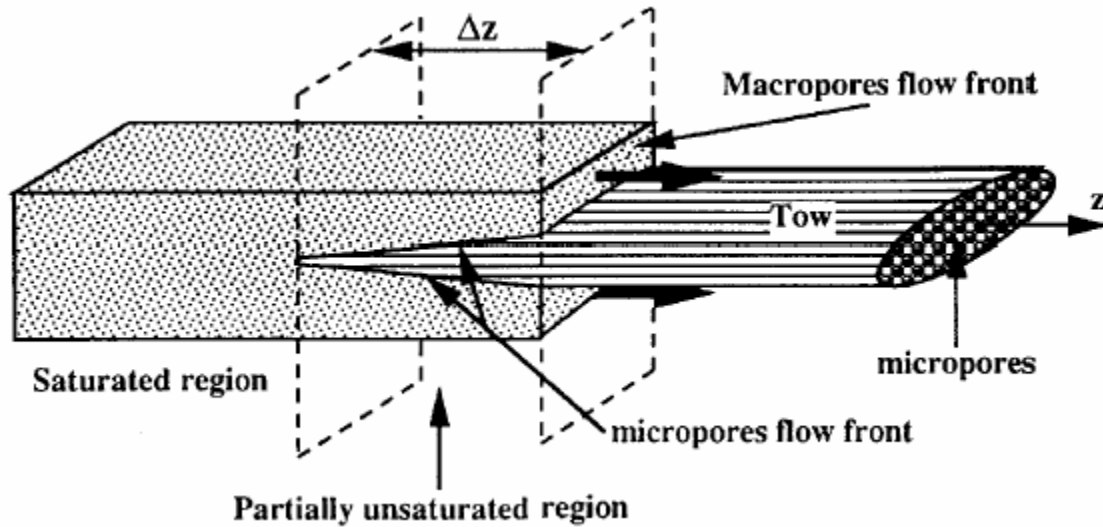


Figure A.8 Dual Scale Flow in Fibrous Reinforcement Material

Usually the lower the surface tension of the fluid, the better the wetting behavior, the higher the capillary pressure and so the higher the measured permeability values [140, 153], and the capillary pressure usually plays a more important role when the fiber volume fraction is higher [149], but the difference in measured permeability values between unsaturated and saturated measurements still stay within experimental scatters [141, 146, 152, 153, 157] in most results, considering the larger scatter of the permeability magnitude, especially for those of random mats [152], Slade [159] and Patel [162, 163] described the capillary effect through the Capillary Number, Ca :

$$Ca = \frac{v\mu}{\gamma \cos \theta} \quad (A-22)$$

where v is the interstitial fluid velocity, μ is the fluid viscosity, γ is the fluid surface tension, θ is the contact angle between the fluid and the fiber surface. The transition region from capillary dominated flow to viscous dominated flow happens when Ca is 0.003 for flow parallel to the UD preform, 0.005 transverse to the UD preform, or 0.001 for bi-directional performs. As Ca becomes smaller and smaller, the flow is more and more dominated by capillary effect (micro-flow inside the yarn), when Ca gets larger and larger, the flow is more and more dominated by viscous effect. The results that the difference between wet and dry experiments was within the experimental scatter contradicted Diallo's and Amico's results [137, 140]. He found that the permeability of a glass fabric (Thermoformable glass fabric

from Brochier, called EB 315) at 47% fiber volume fraction measured with Glycerin was 70% higher than that measured with DCS. He ascribed this to different wetting behavior because DCS wets the glass fabric much worse than Glycerin oil does, so capillary flow in the later has a more important effect. However, Diallo or Amico didn't specify the number of experiments he performed, nor did they have the statistical distribution of permeability measured with different fluids, so made such difference ambiguous. Lekakou, et. al. [145] measured the permeability values from UD measurements, and when they increased the flow rate they found much higher permeability values. Obvious they have race-tracking errors.

Contrary to capillary effect is the sink effect [149, 159, 160]: when the injection pressure or flow rate is very high the fluid flow is macro flow dominated, as the fluid flows through the macro-pores, it is possible that a considerable amount of fluid is drawn from the macro flow and impregnates the fiber tows transversely, which happens behind the fluid flow front. This process was described as Figure A.8 above, in which micro voids may exist inside the tows. When the fluid flows around the fiber tows without impregnating them due to high flow rate, the pressure measured is higher than the real value, and so the permeability measured is lower than the real value. When sink effect happens, it helps to lower the injection pressure needed, which makes the measured permeability approach the real value (saturated permeability value). In reference [149], Binetruy measured the unsaturated UD permeability for a nearly unidirectional woven glass fabric firstly, using constant injection pressure condition. And then he applied a small partial vacuum at the mold inlet to remove the liquid (BP oil) from the macro pores, with the assumptions that such vacuum was able to withdraw all the liquid from the macro pores, and that the surface tension of the fluid was able to keep all the fluid inside the yarns. Then he did the injection experiment again and he found that the average velocity for the flow front in the latter was about 1.6 times as much as that in the first time. So he arrived at the conclusion that the tow impregnation from the fluid in the macro pores led to the velocity drop. However, his assumption and experiment details described above were worthy great debate. Slade's work [159] described the interaction between macro flow and micro flow very well: the sink strength is a function of the capillary number in that the higher the later and the higher the former, and is a function of the ratio of flow resistances in the tow and inter-tow regions. When sink effect happens, it lowers the slope of the inlet pressure versus time in the case of constant flow rate injection experiment.

b) 1D measurement vs 2D. UD and Radial experimental techniques are often, but not always consistent [144], the difference was explained by Parnas, et. al. as that the radial flow mold and the UD flow mold were closed differently, thus it's plausible that the layers of fabric packed differently in the two molds. Lekakou, et. al. [145] found the permeability in the 1D case to average 10 times those found in 2D, probably due to the edge effects in the 1D case.

2. Material Parameters

a) Fiber volume fraction, V_f which is the most important influence on permeability values. The higher V_f , the lower the permeability value in the same direction.

b) Porous media geometry, probably the most important reason for the statistical nature of the permeability values [128, 137, 157, 164-166], i. e. the complex pore geometry and its ease of change during lay up may be the most important reason for the permeability broad distribution observed.

So any factors that influence V_f and porous media geometry also affect permeability values. These factors include compaction pressure [167] and speed, fabric creep behavior [167], number of layers [158], fabric deformation during handling or placing in the mold [12, 156], compression of the perform near the injection gate [168], and sizing of yarns [165, 166].

c) Type of Fluids [136, 137, 140, 153, 157]

The commonly used fluids are silicon oil or diluted corn syrup (DCS), because they have typical Newtonian behavior over a broad range of shear rates, and are easy to clean and inexpensive. Sometimes Epon epoxide liquid, motor oil, corn oil, vinyl ester, polyester, paraffin based oil, or glycerin is also used [140, 153]. The viscosity of DCS has larger variation with temperature [157] and it is also sensitive to the amount of dilution and so water evaporation. The viscosity of fluid doesn't affect the measured results, but it's important that it keeps constant during the measurements.

In addition, DCS has higher surface tension and so wets the fiber surfaces worse [153, 157]. In case of carbon fabric, a qualitative inspection revealed that the carbon fiber tows are not evenly wet by the DCS even after the permeability experiment [140]. Steenkamer, et. al. [136] found that the surface tension of DCS > that of vinyl ester > that of motor oil, and that the permeability measured using DCS < that of vinyl ester < that of motor oil. The most direct measure of wetting of work was defined as the Spreading Coefficient [138], given as $W_s = \gamma_{sv} - \gamma_{sl} - \gamma_{lv}$ (A-23) where γ_{sv} , γ_{sl} , γ_{lv} are surface tensions between the solid and the vapor, the solid and the liquid, and the liquid and the vapor, respectively. When W_s is larger than 0, the liquid can completely wet the solid surface, i.e., the contact angle is 0.

3. Instrument effects: Edge effects, the most commonly associated error with the UD experiment [125], Wall resistance [143, 169, 170], Mold deformation [125] under high compaction pressure [167] and injection pressure [135].

4. Other experimental parameters, which may change the fabric structural features when change: Compacting pressure [167], Injection pressure/flow rate [8, 13, 134, 140, 141, 149, 152, 171-173], Temperature, The size and homogeneity of the sample [150], The size or shape of injection holes [8, 135, 136, 141, 144, 146, 173], and Time/Relative Position. Diallo [140] found that for saturated steady flow experiments, the fabric showed a slight increase in permeability at high pressure gradients (above 600 KPa/m) due to the perform deformation under high injection pressures.

V. Modeling of Permeability

Due to the complexity of the dependence of experimental permeability on these factors listed above, the most reliable way of assessing the permeability is experiment, in spite of numerous drawbacks in the experimental approach [174]. But people have proposed a lot of models to calculate the permeability.

1. Analytical Models

a) The Carman-Kozeny model, also called the “Hydraulic radius theory”, provides good permeability estimation for longitudinal flow along fibers under low porosities up to 0.5

[164]. The porous media is assumed to be equivalent to a conduit with a constant cross sectional area but an extremely complicated shape. Fluid flow in a capillary pipe was assumed as Hagen-Poiseuille flow, then the permeability can be described [133]:

$$K = \frac{1}{k_s} \frac{D_f^2}{4} \frac{\varepsilon^3}{(1-\varepsilon)^2} \quad (\text{A-24})$$

where D_f is the average fiber diameter and ε is the porosity [138] (the volume fraction of porous sample that is occupied by the pore and void space). k_s is defined as $k_0(L_e/L)^2$, the Kozeny constant, which contains the tortuosity information [137, 175] and usually explains the deviation from experimental permeability values in this model despite the other reasons [133].

b) Brinkman model, in which Brinkman treated the mold filling situation in RTM as the flow around submerged objects, then derived the permeability [133]:

$$K = \frac{D_p^2}{72M} \left\{ 3 + \frac{4}{1-\varepsilon} - 3 \left(\frac{8}{1-\varepsilon} - 3 \right)^{1/2} \right\} \quad (\text{A-25})$$

where M is the effective porosity, D_p represents the averaged particle size, ε is the porosity. The modified Brinkman's treatment is good for estimation of permeability in high porosity media above 0.7.

c) Navier-Stokes Equation, is the most general law to describe fluid flow within the porous media for incompressible flow [125].

2. Numerical Models

a) Lattice Boltzman Model (LBM), LBM is particularly important for simulations of fluid flow in complex geometries [176, 177], multi-scale porous media [178] and for studies of interfacial dynamics/ multiphase flow with moving boundaries [179].

The LBM is based on microscopic models and mesoscopic kinetic equations [175]. Microscopic models are used to derive the most probable fabric structure and mesoscopic

kinetic equations are used to derive the fluid flow behavior. Firstly, the reinforcement and its deformability are characterized. Then with the input data and the simulation tool, LBM is used to get the permeability tensor. LBM has the simple algorithm and wide applicability [13, 174, 180], but the calculation is extremely CPU time consuming.

b) Finite Element Models are the most important numerical models in which Darcy's law is solved in discretized space [181, 182]. In FEM, the choice of the type of elements and mesh has great influence on the simulation outcome [129]. People are trying to implement and validate re-meshing algorithms to adapt the constant changing flow front.

One point to note is that these researchers in modeling start from a well-defined unit-cell and assume such unit-cell repeats throughout the material. Such practice does not account for the real dimensional fluctuations of fabric structure and so the variability of real permeability values [134].

REFERENCES

1. Matthews, F.L., Rawlings, R. D., *Composite Materials: Engineering and Science*. 1994.
2. Akovali, G., *Handbook of Composite Fabrication*. 2001.
3. Chou, T.-W., and Ko, Frank K., *Textile Structural Composites*. 1988, Amsterdam, The Netherlands: Elsevier Science Publishing Company Inc.
4. Cox, B.N.F., Gerry, *Handbook of Analytical Methods for Textile Composites*. March 1997.
5. Zweben, C., Hahn, H. T. and Chou, Tsu-Wei, *Delaware Composites Design Encyclopedia*. Mechanical Behavior And Properties of Composite Materials. Vol. 1. 1989: Technomic.
6. Odian, G., *Principles of Polymerization*. 4th ed. 2004, Staten Island, New York: A John Wiley & Sons, INC.
7. *Technical reference of BGF: <http://www.bgf.com/techRefGlassFilament.asp>*.
8. Kruckenberg, T.P., R., *Resin transfer moulding for Aerospace Structures*. 1998, Dordrecht, The Netherlands: Kluwer Academic Publishers.
9. Medvedyev, O.O.T., Y. L., *The Outlook for the use of basalt continuous fibers for composite reinforcement*. International SAMPE Symposium and Exhibition, 2004. **49**: p. 2299-2303.
10. Bader, M.G., Smith, Wilburn, Isham, Allan B., Rolston, J. Albert, Metzner, Arthur B., *Delaware Composites Design Encyclopedia*. Processing and Fabrication Technology. Vol. 3. 1990.
11. Hull, D., *An Introduction to Composite Materials*. 1985, New York, NY: Cambridge University Press.
12. Rudd, C.D.e.a., *Liquid Moulding Technologies*. 1997, Cambridge, UK: Woodhead Publishing Limited.
13. Hoes, K., *Development of a New Sensor-based Set-up for Experimental Permeability Identification of Fibrous Media*. 2003, University of Brussels: Brussels.
14. Wambua, P.a.V., I. *Hemp fabric reinforced polypropylene composites: an investigation of the mechanical properties*. in *Composite for the future - 10th European Conference on Composite Materials*. 2002. Bruges, Belgium.
15. Katayama, T.e.a. *Study on injection molding of bamboo fiber reinforced thermoplastics*. in *the International Conference on High Performance Structure & Composites*. 2002. Seville, Spain.
16. Wool, R.P., Hu, B. and Shenton, H. W. *Composites from Soybeans*. in *Composite for the future - 10th European Conference on Composite Materials*. 2002. Bruges, Belgium.
17. Katori, S.a.K., T. *Injection molding of silk fiber reinforced biodegradable composites*. in *the International Conference on High Performance Structure & Composites*. 2002. Seville, Spain.
18. Vazquez, A.e.a. *Processing and properties of biodegradable composites based on Mater-Bi and sisal fiber*. in *the 12th International Conference on Composite Materials ICCM-12*. 1999. Paris, France.
19. Liholt, H.e.a. *Natural Composites based on cellulosic fibers and polypropylene matrix - their processing and characterization*. in *Composite for the future - 10th European Conference on Composite Materials*. 2002. Bruges, Belgium.

20. Gutowski, T.G., *Advanced Composites Manufacturing*. 1997: John Wiley & Sons, Inc.
21. Icardi, G., *Market Overview of Industrial Processes In Composites: Future Trends*. 2000, Internal Report Saint-Gobain Vetrotex Italia s. p. a. p. 1-61.
22. Ashby, M.F.a.J., D. R. H., *Engineering Materials 2 - An Introduction to Microstructures, Processing and Design*. 1988: Pergamon Press.
23. Jones, R.M., *Mechanics of Composite Materials*. 1975, Boston: McGraw-Hill Book Corporation.
24. Hill, R., *Elastic properties of Reinforced Solids: Some Theoretical Principles*. Journal of the Mechanics and Plastics of Solids, 1963. **11**: p. 357.
25. Chamis, C.C.a.S., G. P., *Critique on Theories Predicting Thermoelastic Properties of Fibrous Composites*. Journal of Composite Materials, 1968. **2**: p. 332.
26. Hill, R., *Theories of Mechanical Properties of Fiber-Strengthened Materials. I. Elastic Behavior*. Journal of the Mechanics and Plastics of Solids, 1964. **12**: p. 199.
27. Hill, R., *A Self-Consistent Mechanics of Composite Materials*. Journal of Mechanics and Plastics of Solids, 1965. **13**: p. 213.
28. Hastin, Z., *On Elastic Behavior of Fiber Reinforced Materials*. Journal of the mechanics and Plastics of Solids, 1965. **13**: p. 119.
29. Steele, J.H.a.H., H. W., *Failure Modes In Composites*. 1973: The Metallurgical Society of the American Institute of Mining, Metallurgical and Petroleum Engineers.
30. Hahn, H.T.a.T.T.C., *Advances in Composite Materials*. Vol. 1. 1980: Pergamon Press.
31. Rosen, B.W., *Fiber Composite Materials*. 1965.
32. Gurland, D.E.G.a.J., Journal of the mechanics and physics of solids, 1962. **10**: p. 365.
33. Zweben, C., *Tensile Failure Analysis of Fibrous Composites*. AIAA Journal, 1968. **6**(12): p. 2325.
34. Davis, J.G., *Compressive Strength of Lamina Reinforced and Fiber Reinforced Composite Materials*. 1973, Virginia Polytechnic Institute and State University.
35. Brelant, S.a.P., I., *Fabrication and Environmental Interaction Effects of Filament-Wound Composites, Mechanics of Composite Materials*. 1970: Pergamon Press.
36. Doner, D.F.A.a.D.R., *Longitudinal Shear Loading of a Unidirectional Composite*. Journal of Composite Materials, 1967. **1**: p. 4.
37. Woodberry, R.F.H.B., D. E. *Application of Advanced Fibers to Chambers for Solid Propellant Rocket Motors*. in *Chemical Propulsion Information Agency Meeting*. Nov 1973. Silver Spring, Maryland.
38. Tubbs, M.C., *Textile Terms and Definitions*. 9 ed. 1991: Biddles Limited.
39. Cox, B.N.D., M. S., *The Macroscopic Elasticity of 3D Woven Composites*. Journal of Composite Materials, 1995. **29**(6): p. 785-819.
40. Curtis, P.T.a.B., S. M., *An assessment of the Potential of Woven Carbon Fiber-Reinforced Plastics for High Performance Applications*. Composites, 1984. **15**(4): p. 259-265.
41. Curtis, P.T.a.M., B. B. *A Comparison of the Fatigue Performance of Woven and Non-woven CFRP Laminates*. in *ICCM V*. 1985. San Diego.
42. Shibata, N., Nishimura, A. and Norita, T., *Graphite Fiber's Fabric Design and Composite Properties*. SAMPE Quarterly, 1976: p. 25.
43. Evans, A.G.a.A., W. F., *Kinking as a Mode of Structural Degradation in Carbon Fiber Composites*. Acta Metallurgica, 1978. **26**: p. 725-738.

44. Reifsnider, K.L.a.M., K. L., *Compressive Strength and Mode of Failure of 8H Celion 3000/PMR15 Woven Composite Material*. Journal of Composites Technology & Research, 1988. **10**: p. 156-164.
45. Karayaka, M.a.K., P., *Deformation and Failure Behavior of Woven Composite Laminates*. Journal of Engineering Materials & Technology, 1995. **116**: p. 222-232.
46. Argon, A.S., *Treatise on Materials Science and Technology*. Vol. 1. 1980, New York: Academic Press.
47. Fleck, B.B.a.N.A., *Compressive Failure of Fiber Composites*. Journal of the mechanics and physics of solids, 1993. **41**: p. 183-211.
48. Cox, B.N. *Fundamental Concepts in the Suppression of Delamination Buckling by Stitching*. in *9th DoD/NASA/FAA Conference on Fibrous Composites in Structural Design*. 1991. Lake Tahoe, Nevada.
49. Cox, B.N., Massabo, R. and Kedward, K., *The Suppression of Delamination in Curved Structures by Stitching*. Composites.
50. Cox, B.N., *Delamination and Buckling in 3D Composites*. Journal of Composite Materials, 1994. **28**: p. 1114-1126.
51. Adams, D.F.a.W., D. E., *In-Plane and Interlaminar Iosipescu Shear Properties of Various Graphite Fabric/Epoxy Laminates*. Journal of Composites Technology & Research, 1987. **9**(3): p. 88-94.
52. Xu, J., Cox, Brain N., McGlockton, M. A. and Carter, W. C., *A Binary Model of Textile Composites-II. The Elastic Regime*. Acta Metallurgica et Materialia, 1995. **43**(9): p. 3511-3524.
53. Dadkhah, M.S., Flintoff, J. G., Kniveton, T. and Cox, B. N., *Simple Models for Triaxially Braided Composites*. Composites, 1995. **26**: p. 91-102.
54. Cox, B.N., Dadkhah, M. S., Inman, R. V. and Morris, W. L., *Mechanics of Compressive Failure in 3D Composites*. Acta Metallurgica et Materialia, 1992. **40**: p. 3285-3298.
55. Cox, B.N., Dadkhah, M. S., Morris, W. L. and Flintoff, J. G., *Fatigue Mechanism of 3D Woven Composites in Tension, Compression, and Bending*. Acta Metallurgica et Materialia, 1994. **42**: p. 3967-3984.
56. Roy, A.K., *In situ Damage Observation and Fatigue in Model Laminates Containing Planar Yarn Crimping of Woven Composites*. Mechanics of Composite Materials and Structures, In Press.
57. Dadkhah, M.S., Cox, B. N. and Morris, W. L., *Compression - Compression Fatigue of 3D Woven Composites*. Acta Metallurgica et Materialia, 1995. **43**: p. 4235-4245.
58. Plueddemann, E.P., *Silane Coupling Agents*. 2 ed. 1991: Plenum Press.
59. Plueddemann, E.P., Clark, H. A., Nelson, L. E. and Hoffmann, K. R., *Silane coupling agents for reinforced plastics*. Modern Plastics, 1962. **39**: p. 136-146.
60. Plueddemann, E.P.a.S., G. L., *Catalytic and electrokinetic effects in bonding through silanes*. Modern Plastics, 1974. **51**(3): p. 74-84.
61. Ishida, H.a.K., J. L., *An investigation of the Coupling Agent/Matrix Interface of Fiberglass Reinforced Plastics by Fourier Transform Infrared Spectroscopy*. Journal of Polymer Science, Polymer Physics Edition, 1979. **17**: p. 615-626.
62. Ishida, H.a.K., J. L., *Fourier transform infrared spectroscopic study of the silane coupling agent/porous silica interface*. Journal of Colloid and Interface Science, 1978. **64**(3): p. 567-576.

63. Erickson, P.W., *Silane treatment of glass fabric from nonaqueous solvents*. Annual Technical Conference, SPI (Soc. Plast. Ind.) Reinforced Plastics /Composite. Divison, Proceeding, 1969. **24**: p. 19-B-1-10.
64. Kumins, C.A.a.R., J., *Effect of solid-polymer interaction on transition temperature and diffusion coefficients*. Journal of Polymer Science, Part A: General Papers, 1963: p. 527-540.
65. Plueddemann, E.P., *Aqueous solutions of organoalkoxysilanes*. Annual Technical Conference, SPI (Society of Plastic Industry) Reinforced Plastic /Composite Divison, Proceeding, 1969. **24**: p. 19-A-16.
66. Schrader, M.E., Lerner, I. and D'Oria, F. J., *Radioisotope study of coupling agents in reinforced plastics*. Modern Plastics, 1967. **45**(1): p. 195-197.
67. Vogel, G.E., Johannson, O. K., Stark, F. O. and Fleischmann, R. M., *Chemical nature of the glass-coupling agent interface*. Proceedings of the Annual Conference - Reinforced Plastics/Composites Institute, Society of the Plastics Industry, 1967(13-B): p. 10.
68. Parks, G.A., *The isoelectric points of solid oxides, solid hydroxides, and aqueous hydroxo complex systems*. Chemical Reviews, 1965. **65**(2): p. 177-198.
69. Plueddemann, E.P.a.S., G. L., *Catalytic and electrostatic effects in bonding through silanes*. Proceedings of the Annual Conference - Reinforced Plastics/Composites Institute, Society of the Plastics Industry, 1973. **28**(21E): p. 12.
70. Plueddemann, E.P., *Promoting adhesion of coatings through reactive silanes*. Journal of Paint Technology, 1968. **40**: p. 1-9.
71. Vanderbilt, B.M.a.C., R. E., *Bonding of fibrous glass to elastomers*. Industrial & Engineering Chemistry Product Research and Development, 1965. **4**(1): p. 18-22.
72. Clark, H.A.a.P., E. P., *Bonding of silane coupling agents in glass-reinforced plastics*. Modern Plastics, 1963. **40**(10): p. 133-135.
73. Kaas, R.L.a.K., J. L., *Improved performance of silane coupling agents by catalysis of surface reactions*. Technical Papers - Society of Plastics Engineers, 1976. **22**: p. 22-26.
74. Vaughan, D.J.a.P., R. C., *Why silanes? An SEM Investigation of The Effects of Finishes On The Incursion of Liquids Into Glass Reinforced Composites*. Anniversary Technical Conference, 1975. **30**(Section 22-B): p. 1-5.
75. Plueddemann, E.P., *Composites Having Ionomer Bonds With Silanes at The Interface*. Journal Of Adhesion, 1989. **3**(2): p. 131-139.
76. ThomINETTE, F., Salmon, L., Pays, M. F. and J. Verdu, J., *Influence of The Nature of The Coupling Agent On The Aging Of Glass Fiber-Epoxy Composite Materials*. European Conference On Composite Materials, 1998. **8**: p. 157-158.
77. Shortall, J.B.a.Y., H. W. C., *The interfacial bond strength in glass fiber-polyester resin composite systems. Part I. The measurement of bond strength*. Journal of Adhesion, 1976. **7**(4): p. 311-332.
78. Park, J.M.a.S., R. V., *Interfacial shear strength and durability improvement by monomeric and polymeric silanes in basalt fiber/epoxy single-filament composite specimens*. Journal of Adhesion Science and Technology, 1991. **5**(6): p. 459-477.
79. Subramanian, R.V.a.S., K. H., *Silane Coupling Agents For Basalt Fiber Reinforced Polymer Composites*. Polymer Science and Technology, 1985. **27**: p. 205-236.
80. Subramanian, R.V.a.S., K. H., *Silane coupling agents for basalt fiber reinforced polymer composites*. Polymer Preprints, 1983. **24**(1): p. 208-209.

81. Shu, K.H., *Interfacial Bonding In Basalt Fiber Polymer Composite Systems*. 1978, Washing State University.
82. Subramanian, R.V., *Basalt Fiber - A New Cost Mineral Fiber For Composites*. Advanced Composites Technology - Conference on Advanced Composite Technology, 1978.
83. Subramanian, R.V., Tang, T. J. Y. and Austin, H. F., *Reinforcement of Polymers By Basalt Fibers*. SAMPE Quarterly, 1977: p. 1-10.
84. Jung, T.H.a.S., R. V., *Alkali Resistance Enhancement of Basalt Fiber by Hydrated Zirconia Films Formed by the Sol-gel Process*. Journal of Materials Research, 1994. **9**: p. 1006-1013.
85. Subramanian, R.V.a.S., K. H., *Interfacial Bonding In Basalt Fiber - Polymer Composites*. Annual Technical Conference, SPI (Soc. Plast. Ind.) Reinforced Plastics /Composite. Divison, Proceeding, 1979(Section 17C): p. 1-10.
86. Park, J.M., Subramanian, R. V. and Bayoumi, A. E., *Interfacial Shear Strength and durability improvement by silanes in single-filament composite specimens of basalt fiber in brittle phenolic and isocyanate resins*. Journal of Adhesion Science and Technology, 1994. **8**(2): p. 133-150.
87. Subramanian, R.V.a.A., H. F., *Silane Coupling Agents In Basalt - Reinforced Polyester Composites*. International Journal of Adhesion and Adhesives, 1980. **1**: p. 50-54.
88. Artemenko, S.E., *Polymer Composite Materials Made From Carbon, Basalt, And Glass Fibers. Structure and Properties*. Fiber Chemistry, 2003. **35**(3): p. 226-229.
89. Bashtannik, P.I., Ovcharenko, V. G. and Boot, Y. A., *Effects of Combined Extrusion Parameters on Mechanical Properties of Basalt Fiber-Reinforced Plastics Based On Polypropylene*. Mechanics of Composite Materials, 1997. **33**(6): p. 600-603.
90. Park, J.M., Subramanian, R. V., *Effects of silane coupling agents on internal reinforcement of wood by E-glass and basalt fibers*. Journal of Adhesion Science and Technology, 1994. **8**(12): p. 1473-1483.
91. Wong, R., *Recent Aspects of Glass Fiber-Resin Interfaces*. Journal of Adhesion, 1972. **4**: p. 171-179.
92. Nichols, G.D., Peek, D. M. H., Roy, C. and Vaughan, D. J., *Application of x-ray photoelectron spectroscopy to the study of fiberglass surfaces*. Applied Spectroscopy, 1974. **28**(3): p. 219-222.
93. Knoff, W.F., *A Modified Weakest-Link Model for Describing Strength Variability of Kevlar Aramid Fibers*. Journal of Materials Science, 1987. **22**: p. 1024.
94. *Design Properties of Marine Grade Fiberglass Laminates*. March 1997, Owens-Corning Fiberglass Corporation.
95. Yoshida, H., Ogasa, T. and Hayashi, R., *Statistical Approach to the Relationship Between ILSS and Void content of CFRP*. Composites Science and Technology, 1986. **25**: p. 331.
96. Zweben, C.a.N., J. C., *Kevlar 49/Thornel 300 Hybrid Fabric Composites for Aerospace Applications*. SAMPE Quarterly, 1976: p. 1.
97. Swanson, G.D.a.H., J. R. *ASTM STP 497*. in *Composite Materials: Testing and Design*. 1972: American Society for Testing and Materials.
98. Owen, M.J., *Composite Materials, Fracture and Fatigue*. Vol. 5. 1974, NY: Academic Press.

99. Carlsson, L., Eidefeldt, C. and Mohlin, T., *Influence of Sublaminar Cracks on the Tension Fatigue behavior of a Graphite/Epoxy Laminate*. Composite Materials: Fatigue and Fracture, ASTM STP 907, 1986: p. 361.
100. Kim, R.Y., *Composite Materials*. Vol. 2. 1980: Pergamon Press.
101. Reifsnider, K.L.a.C., S. W., *Damage Tolerance & Durability of Material Systems*. 2002, New York: John Wiley & Sons, Inc.
102. Wagner, H.D., Schwartz, P. and Phoenix, S. L., *Lifetime Statistics for Single Kevlar 49 Filaments in Creep Rupture*. Journal of Materials Science, 1986. **21**: p. 1868.
103. http://www.weibpar.com/support/docs/Weibull_Theory.PDF.
104. Lang, R.W.a.M., J. A., *Crack Tip Heating in Short Fiber Composites under Fatigue Loading Conditions*. Journal of Materials Science, 1987. **22**: p. 3576.
105. Hahn, H.T. in *Composite Materials: Testing and Design (5th Conference)*, ASTM STP 674, American Society for Testing and Materials. 1979.
106. Dally, J.W.a.B., L. J., Journal of Composite Materials, 1967. **1**: p. 424.
107. Sun, C.T.a.C., W. S. in *Composite Materials: Testing and Design (5th Conference)*, ASTM STP 674, American Society for Testing and Materials. 1979.
108. Sendekyj, G.P.a.S., H. D. in *Composite Materials: Testing and Design (4th Conference)*, ASTM STP 617, American Society for Testing and Materials. 1977.
109. Fujii, Y., Mizoguchi, M. & Hamada, H., *Durability and degradation mechanism of E and ECR glass reinforced vinylester resin under acid and alkali conditions*. Durability Analysis of Composite Systems, 2001: p. 137-140.
110. Ellyin, F.a.R., Christof, *The Influence of Aqueous Environment, Temperature and Cyclic Loading on Glass-Fibre/Epoxy Composite Laminates*. Journal of Reinforced Plastics and Composites, 2003. **22**(7): p. 615-636.
111. Zhang, S., Karbhari, Vistasp M., Ye, Lin and Mai, Yiu-Wing, *Evaluation of Property Retention in E-Glass/Vinylester Composites after Exposure to Salt Solution and Natural Weathering*. Journal of Reinforced Plastics and Composites, 2000. **19**(09): p. 704-731.
112. Zhang, S.a.K., Vistasp M. *Investigation of Environmental Effects on Pultruded E-Glass/Vinyl ester Composites*. in Proc ACUN-3 "Technology Convergence in Composites Applications". 6-9 Feb 2001. Sydney, Australia: UNSW.
113. Schultheisz, C.R., McDonough, Walter G., Kondagunta, Srikanth, etc., *Effect of Moisture on E-Glass/Epoxy Interfacial and Fiber Strengths*. Composite Materials: Testing and Design, 1997. **13**: p. 257-286.
114. Wu, L., Murphy, Karen, Karbhari, Vistasp M. and Zhang, James S., *Short-Term Effects of Sea Water on GV*. Journal of Applied Polymer Science, 2002. **84**: p. 2760-2767.
115. Karbhari, V.M.a.Z., S., *E-Glass/Vinylester Composites in Aqueous Environments - I: Experimental Results*. Applied Composite Materials, 2003. **10**: p. 19-48.
116. Pritchard, G.a.S., S. D., *The Use of water absorption kinetic data to predict laminate property changes*. Composites, 1987. **18**(3): p. 227-232.
117. Boinard, E., Pethrick, Richard A., Dalzel - Job, Jody and Macfarlane, Colin J., *Influence of resin chemistry on water uptake and environmental ageing in glass fiber reinforced composites - polyester and vinyl ester laminates*. Journal of Materials Science, 2000. **35**: p. 1931-1937.
118. Ikegawa, N.a.H., Hiroyuki. *Degradation behavior in hot water environment of GFRP parts by structural resin transfer moulding*. in Joint Canada-Japan Workshop on Composites. 1997.

119. Sridharan, S., Zureick, Abdul-Hamid and Muzzy, John D. *Effect of Hot-Wet Environments On E-Glass/Vinylester Composites*. in *Annual Technical Conference - Society of Plastics Engineers*, 56th. 1998.
120. Karbhari, V.M., Rivera, J. and Zhang, J., *Journal of Applied Polymer Science*, 2002. **86**: p. 2255-2260.
121. Foster, D.C. *The Feasibility of a Composite Highway Bridge*. in *Proceedings of the ACUN-3 International Composites Conference*. 2001.
122. Otaigbe, J.U., *Effect of Coupling Agent and Absorbed Moisture on the Tensile Properties of a Thermoplastic RRIM Composite*. *Journal of Applied Polymer Science*, 1992. **45**: p. 1213-1221.
123. Shen, C.-H.a.S., George S., *Moisture absorption and desorption of composite materials*. *Journal of Composite Materials*, 1976. **10**: p. 2-20.
124. Baichen, L., Bickerton, S., and Advani, S. G., *Modeling and simulation of resin transfer moulding (RTM) - gate control, venting and dry spot prediction*. *Composites, Part A*, 1996. **27**(2): p. 135-141.
125. Parnas, R.S., *Liquid Composite Molding*. 2000, Verlag, Munchen: Carl Hanser.
126. *Vetrotex - Saint Gobain, Brochure: Memento 2001*.
127. Xu, J.a.M., Yulu, *The Technology and Applications of Resin Transfer Molding (RTM)*. *China Plastics*, 1992. **6**: p. 9-16.
128. Gauvin, R.e.a., *Permeability Measurement and Flow Simulation Through Fiber Reinforcement*. *Polymer Composites*, 1996. **17**(1): p. 34-42.
129. Huber, U.a.M., M. *Methodical application of liquid composite molding simulation*. in *Proceedings of the International Conference on High Performance Structures & Composites*. 2002. Sevilla, Spain.
130. Blanchard, P. *Structural Design of Lightweight Tooling for Liquid Composite Molding*. in *Proceedings of the Third Canadian International Composites Conference (CANCOM 2001)*. 2001. Montreal, Quebec, Canada.
131. Bird, R.B., Stewart, W. E. and Lightfoot, E. N., *Transport Phenomena*. 2001, John Wiley, NY.
132. Slattery, J.C., *Momentum, Energy, and Mass Transfer in Continua*. 2 ed. 1981, Huntington, NY: Robert E. Kreiger.
133. Dullien, F.A.L., *Single Phase Flow Through Porous Media and Pore Structure*. *The Chemical Engineering Journal*, 1975. **10**: p. 1-34.
134. Greve, B.N.a.S., S. K., *Directional Permeability Measurement of Fiberglass Reinforcements*. *SAE Transactions*, 1990. **99**: p. 331-343.
135. Weitzenbock, J.R., Sheno, R. A., and Wilson, P. A., *Radial Flow permeability measurement. Part A: Theory*. *Composites Part A*, 1999. **30**: p. 781-796.
136. Steenkamer, D.A.e.a., *Experimental characterization of permeability and fiber wetting for liquid moulding*. *Journal of Materials Science*, 1995. **30**(12): p. 3207-3215.
137. Amico, S.a.L., C., *An experimental study of the permeability and capillary pressure in resin-transfer moulding*. *Composites science and Technology*, 2001. **61**: p. 1945-1959.
138. Dullien, F.A.L., *Porous Media - Fluid Transport and Pore Structure*. 1992: Academic Press, INC.
139. Adler, P.M., *Porous Media*. 1992: Butterworth-Heinemann.

140. Diallo, M.L., Gauvin, R., and Trochu, F. *Key factors affecting the permeability measurement in continuous fiber reinforcements*. in *Proceedings of ICCM-11*. 1997. Gold Coast, Australia.
141. Lundstrom, T.S.e.a., *In-plane permeability measurements: a Nordic round-robin study*. *Composites Part A*, 2000. **31**: p. 29-43.
142. Gebart, R.B.a.L.m., P., *Measurement of In-Plane Permeability of Anisotropic Fiber Reinforcements*. *Polymer Composites*, 1996. **17**(1): p. 43-51.
143. Ferland, P., Guittard, D., and Trochu, F., *Concurrent Methods for permeability measurement in Resin Transfer Molding*. *Polymer Composites*, 1996. **17**(1): p. 149-158.
144. Parnas, R.S.a.S., A. J., *A Comparison of the Unidirectional and Radial In-Plane Flow of Fluids Through Woven Composite Reinforcements*. *Polymer Composites*, 1993. **14**(5): p. 383-394.
145. Lekakou, C.e.a., *Measurement Techniques and effects on in-plane permeability of woven cloths in resin transfer moulding*. *Composites Part A*, 1996. **27**: p. 401-408.
146. Adams, K.L.a.R., L., *In-plane Flow of Fluids in Fabrics: Structure/Flow Characterization*. *Textile Research Journal*, 1987. **57**: p. 647-654.
147. Neale, G.a.N., W., *Canadian Journal of Chemical Engineering*, 1974. **52**: p. 475-478.
148. Parnas, R.S.a.C., Y., *Coupled parallel flows of power-law fluids in a channel and a bounding porous medium*. *Chemical Engineering Communications*, 1987. **53**: p. 3-22.
149. Binetruy, C., Hilaire, B., and Pabiot, J., *The interaction between flows occurring inside and outside fabric tows during RTM*. *Composites Science and Technology*, 1997. **57**: p. 587-596.
150. Parnas, R.S.e.a., *Permeability Characterization. Part 1: A Proposed Standard Reference Fabric for Permeability*. *Polymer Composites*, 1995. **16**(6): p. 429-445.
151. Luthy, T.e.a., *Dependence of the 1-D permeability of fibrous media on the fiber volume content: comparison between measurement and simulation*. *Structures and Materials*, 1998. **3**: p. 433-442.
152. Chick, J.P.e.a., *Material Characterization for Flow Modeling in Structural Reaction Injection Molding*. *Polymer Composites*, 1996. **17**(1): p. 124-135.
153. Hammond, V.H.a.L., A. C., *The effects of fluid type and viscosity on the steady-state and advancing front permeability behavior of textile performs*. *Journal of Reinforced Plastics and Composites*, 1997. **16**(1): p. 50-72.
154. Dunkers, J.P.e.a., *The Prediction of Permeability for an Epoxy/E-glass Composite Using Optical Coherence Tomographic Images*. *Polymer Composites*, 2001. **22**(6): p. 803-814.
155. Pan, R.e.a., *Statistical Characterization of Fiber Permeability for Composite Manufacturing*. *Polymer Composites*, 2000. **21**(6): p. 996-1006.
156. Rudd, C.D.e.a., *In-plane Permeability Determination for Simulation of Liquid Composite Molding of Complex Shapes*. *Polymer Composites*, 1996. **17**(1): p. 52-59.
157. Luo, Y.e.a., *Permeability measurement of textile reinforcements with several test fluids*. *Composites Part A*, 2001. **32**(10): p. 1497-1504.
158. Breard, J., *Materiaux composites a matrice polymere: Modelisation numerique de la phase de remplissage du procede R.T.M. et determination experimentale de la permeabilite d'un renfort fibreux*. 1997, University Du Havre.
159. Slade, J., Pillai, K. M., and Advani, S. G., *Investigation of Unsaturated Flow in Woven, Braided and Stitched Fiber Mats during Mold-filling in Resin Transfer Molding*. *Polymer Composites*, 2001. **22**(4): p. 491-505.

160. Parnas, R.S.a.P., F. R., *The Effect of Heterogeneous Porous Media on Mold Filling in Resin Transfer Molding*. Sampe Q., 1991. **23**(2): p. 53-60.
161. Binetruy, C.a.P., J. *Effects of Fabric architectural heterogeneities on effective and saturated permeabilities in RTM*. in *Proceedings of the 12th International Conference on Composite Materials ICCM-12*. 1999. Paris, France.
162. Patel, N.a.R., V., *Effects of fiber mat architecture on void formation and removal in liquid composite molding*. Polymer Composites, 1995. **16**(5): p. 386-399.
163. Patel, N.a.R., V., *Micro scale flow behavior and void formation mechanism during impregnation through a unidirectional stitched fiberglass mat*. Polymer engineering and science, 1995. **35**(10): p. 837-851.
164. Ahn, K.J.a.S., J. C., *Simultaneous Measurement of Permeability and Capillary Pressure of Thermosetting Matrices in Woven Fabric Reinforcements*. Polymer Composites, 1991. **12**(3): p. 146-152.
165. Parnas, R.S.e.a., *The Interaction Micro- and Macroscopic flow in RTM Preforms*. Composite Structures, 1994. **27**: p. 93-107.
166. Ranganathan, S., Easterling, Robert G., Advani, Suresh G., and Phelan, Jr. Frederick R., *The Effect of Micro-Structure Variations on the Permeability of Preform Materials*. Polymers and Polymer Composites, 1998. **6**(2): p. 63-73.
167. Gauvin, R.e.a. *Compaction and Creep Behavior of Glass Reinforcement for Liquid Composites Molding*. in *Proceedings of the 10th Annual ASM/ESD Advanced Composites Conference*. 1994. Dearborn, Michigan, USA.
168. Parnas, R.S., Schultheisz, C. R., and Ranganathan, S., *Hydrodynamically Induced Preform Deformation*. Polymer Composites, 1996. **17**(1): p. 4-10.
169. Gibson, A.G., *Modification of Darcy's law to model mould interface effects in composites processing*. Composites Manufacturing, 1992. **3**(2): p. 113-118.
170. Kaviany, M., *Laminar flow through a porous channel bounded by isothermal parallel plates*. International Journal of Heat and Mass transfer, 1985. **28**(4): p. 851-858.
171. Lekakou, C.a.B., M. G., *Mathematical modeling of macro- and micro-infiltration in resin transfer moulding (RTM)*. Composites Part A, 1998. **29**: p. 29-37.
172. Visconti, C., Langella, I. A., and Durante, M. *The influence of injection pressure on the permeability of unidirectional fiber preform in RTM*. in *Proceedings of the 8th European Conference on Composite Materials (ECCM 8)*. 1998. Napels, Italy.
173. Chan, A.W., Larive, D. E., and Morgan, R. J., *Anisotropic Permeability of Fiber Preforms: Constant Flow Rate Measurement*. Journal of Composite Materials, 1993. **27**(10): p. 996-1008.
174. Belov, E.B.e.a. *Modeling of permeability of textile reinforcements: Lattice Boltzman method*. in *Composites for the future - 10th European Conference on Composite Materials*. 2002. Brugge, Belgium.
175. Shih, C.H.a.L., L. J., *Effect of fiber architecture on permeability in liquid composite molding*. Polymer Composites, 1998. **19**(5): p. 626-639.
176. Kandhai, D., Vidal, D. J.-E., Hoekstra, A. G., Hoefsloot, H., Iedema, P. and Sloot, P. M. A., *A Comparison between Lattice-Boltzmann and Finite Element simulations of fluid flow in static mixer reactors*. International Journal of Modern Physics C, 1998. **9**(8): p. 1123-1128.
177. Martys, N.S.a.C., H., *Simulation of Multicomponent Fluids in Complex three-dimensional Geometries by the Lattice Boltzman Method*. Phys. Rev. E., 1996. **53**: p. 753.

178. Spaid, M.A.A.a.P., F. R., *Lattice Boltzmann method for modeling microscale flow in fibrous porous media*. *Physics of Fluids*, 1997. 9(9): p. 2468-2474.
179. Chen, S.a.D., G. D., *Lattice Boltzmann Method for Fluid Flows*. *Annu. Rev. Fluid. Mech.*, 1998. **30**: p. 329-364.
180. Inamuro, T., Yoshino, M., and Ogino, F., *Lattice Boltzmann simulation of flows in a Three-dimensional Porous Structure*. *International Journal for Numerical Methods in Fluids*, 1999. **29**: p. 737-748.
181. Han, K.e.a., *Flow modeling and simulation of SCRIMP for composites manufacturing*. *Composites Part A*, 2000. **31**: p. 79-86.
182. Trochu, F., Gauvin, R., and Gao, D.-M., *Numerical Analysis of the Resin Transfer Molding Process by the Finite Element Method*. *Advances in Polymer Technology*, 1993. **12**(4): p. 329-342.
183. Militky, J.K., Vladimir, *Ultimate Mechanical Properties of Basalt Filaments*. *Textile Research Journal*, 1996. **66**(4): p. 225-229.
184. Cater, S., *Editorial*. *International Composites News*, March 2002. **40**.
185. Haeberle, D.C., Senne, J. L., Lesko, J. J. & Cousins, T. E. *Performance and Interfacial Stresses In The Polymer Wear Surface/FRP Deck Bond Due to Thermal Loading*. in *Advanced Composite Materials In Bridges and Structures: 3rd International Conference*. 2000.
186. Imamutdinov, M.a.P., G. 2001: Russia. p. 64-67.
187. Sim, J., Park, Cheolwoo & Moon, Do Young, *Characteristics of basalt fiber as a strengthening material for concrete structures*. *Composites, Par B*, 2005. **36**(6-7): p. 504-512.
188. Van de Velde K., K.P., Van Langenhove L., '*Basalt Fibers As Reinforcement For Composites*', <http://www.basaltex.com/logos/basalt%20fibres.pdf>.
189. Chantladze, T., '*Industrial assimilation of the effective type of fiber with multicomponent charge*', <http://www.tctv.ne.jp>.
190. '*Basaltex, The thread of stone*', <http://www.basaltex.com>.
191. Figovsky, O., Beilin, D., Blank, N., Potapov, J., & Chernyshev, V., *Development of Polymer Concrete with Polybutadiene Matrix*. *Cement and Concrete Composites*, 1998. **18**: p. 437-444.
192. Sergeev, e.a., *Basalt Fibers - A Reinforcing Filler for Composites*. *Power Metallurgy and Metal Ceramics*, 1994. **33**(9-10): p. 555-557.
193. BGF Ltd. *Product literature*: <http://www.bgf.com>.
194. Albarrie Ltd. *Product literature*: <http://www.albarrie.com/Filtration/fil-basalt.html>.
195. '*Aketoma - Basalt fabrics, tubes, prepregs, rods, etc...*' <http://www.laseroptronix.com>.
196. *Fire Resistant Board Material*. 2001: European Patent.
197. Zihlif, A.M.R., G., *A study on the Physical Properties of Rock Wool Fiber - Polystyrene Composite*. *Journal of Thermoplastic Composite Materials*, 2003. **16**: p. 273-283.
198. www.laseroptronix.se/exoma/basalt.pdf.
199. <http://www.measurementcomputing.com/>.
200. <http://www.albarrie.com/>.
201. <http://www.syncoglas.com/>.
202. <http://www.carolinanarrowfabric.com/>.
203. Stephens, M.A., *EDF Statistics for Goodness of Fit and Some Comparisons*. *Journal of the American Statistical Association*, 1974. **69**: p. 730-737.
204. www.thermo.com.

205. <http://cchp.meca.polymtl.ca/pages/polyper.php?page=install>.
206. Mertz, D.R., Chajes, M. J. and Gillespie, J. W., *Application of Fiber Reinforced Polymer Composites to the Highway Infrastructure*. 2003, NCHRP Report 503: Washington, D. C.
207. FHWA web site. www.ibrc.fhwa.dot.gov.
208. McCrum, N.G., Buckley, C. P. and Bucknall, C. B., *Principles of Polymer Engineering*. 1989, New York: Oxford University Press.
209. Ramakrishnan, V.T., Neeraj S., *Performance Evaluation of 3-D Basalt Fiber Reinforced Concrete & Basalt Rod Reinforced Concrete*. November 1998, Transportation Research Board, National Research Council.
210. Lisakovski, A.N., Tsybulya, Y. L. and Medvedyev, A. A. *Yarns of Basalt Continuous Fibers*. in *The Fiber Society Spring 2001 Meeting*. May 23-25, 2001. Raleigh, NC.
211. Brik, V.B., *Basalt Fiber Composite Reinforcement For Concrete*. March 1997, Transportation Research Board, National Research Council.
212. *Epon Resin-Curing Agent Systems, Technical Literature*.
http://www.resins.com/resins/am/pdf/Tab12_Appendix%201_Resin_Curing%20Agent_Systems.pdf.
213. Czigan, T., *Basalt Fiber Reinforced Hybrid Polymer Composites*. *Materials Science Forum*, 2005. 4: p. 59-66.
214. Kadykova, Y.A., Artemenko, S. E., Vasil'eva, O. V. and Leont'ev, A. N., *Physicochemical Reaction In Polymer Composite Materials Made From Carbon, Glass, and Basalt Fibers*. *Fiber Chemistry*, 2003. 35(6): p. 455-457.
215. Piggott, M.R., *Load Bearing Fiber Composites*. 2nd ed. 2001, Ontario, Canada: MERP Enhanced Composites Inc.
216. Cameron, N.M., *The effect of environment and temperature on the strength of E-glass fibers. Part 2. Heating and Ageing*. *Glass Technology*, 1968. 9(5): p. 121-130.
217. Tsai, S.W.a.H., T. H., *Introduction to Composite Materials*. 1980, Pennsylvania: Technomic Publishing Company, Inc.
218. Liu, Q., Shaw, Montgomery, Parnas, Richard S. and McDonnell, Anne-Marie H., *Investigation of Basalt Fiber Composite Mechanical Properties for Applications in Transportation*. *Polymer Composites*, 2006. 27(1): p. 41-48.
219. Montgomery, D.C., *Design and Analysis of Experiments*. 5th ed. 2001, New York: John Wiley & Sons, Inc.
220. www.minitab.com/support.
221. Zweben, C., Smith, W. S. and Wardle, M. W. *Test Methods for Fiber Tensile Strength, Composite Flexural Modulus and Properties of Fabric-Reinforced Laminates*. in *Composite Materials: Testing and Design - Fifth Conference*. 1978.
222. Pipes, R.B., Blake, Robert A., Gillespie, John W. and Carlsson, Leif A., *Delaware Composites Design Encyclopedia*. Vol. 6. 1990: Technomic Publishing Company, Inc.
223. Bullock, R.E., *Journal of Composite Materials*, 1974. 1: p. 200.
224. Mittal, K.L., *Silanes & Other Coupling Agents*. 2001: Brill Academic Publishers.
225. Palmese, G.R.a.C., A. J. *Environmental Durability of Polymer Concrete*. in *International SAMPE Symposium*. 1996.
226. Liu, F.P.W., Michael P.; Gardner, Douglas J.; Rials, Timothy G., *Characterization of the interface between cellulosic fibers and a thermoplastic matrix*. *Composite Interfaces*, 1994. 2(6): p. 419-432.

227. Wu, G., *Effects of carbon fiber treatment on interfacial properties of advanced thermoplastic composites*. *Polymer Journal*, 1997. 29(9): p. 705-707.
228. Xiao, W.-z.Y., Wei-xia; Han, Ke-qing; Yu, Mu-huo, *Study on the interface of long glass fiber reinforced PET thermoplastic composite*. *Donghua Daxue Xuebao, Ziran Kexueban*, 2004. 30(4): p. 102-105.
229. Zhang, Y.C.W., X., *Thermal effects on interfacial stress transfer characteristics of carbon nanotubes/polymer composites*. *International Journal of Solids and Structures*, 2005. 42(20): p. 5399-5412.
230. Masud, A.K.M.I., Kiyoshi; Suzuki, Jippei., *Effect of fiber surface treatment on the interface and bending strength of aramid short fiber composite*. *Materials Science Research International*, 2000. 6(3): p. 186-192.